A Measurement of the Inclusive $Z/\gamma^* \to \mu^+\mu^-$ Cross Section and Study of W and Z Events in $p\bar{p}$ Collisions at DØ

Emily L. Nurse

2005

THE UNIVERSITY
of MANCHESTER

Particle Physics Group
Department of Physics and Astronomy

A thesis submitted to The University of Manchester for the degree of
Doctor of Philosophy in the Faculty of Science and Engineering

Contents

List of Figures

List of Tables

Abstract

A measurement of the inclusive $Z/\gamma^* \to \mu^+\mu^-$ cross section for $M_{\mu\mu} > 40$ GeV at $\sqrt{s} = 1.96$ TeV is presented. The measurement is performed using a data sample corresponding to an integrated luminosity of 147.7 pb^{-1}, collected with the DØ detector at the the Tevatron, Fermilab, between September 2002 and October 2003. A total of 14352 di-muon events are selected and a final result of

$$\sigma\,(Z/\gamma^*) = 327.8 \pm 3.4(\text{stat.}) \pm 8.4(\text{syst.}) \pm 21.3(\text{lumi.}) \;\; \text{pb}$$

is obtained. Correcting the number of di-muon events by a factor of 0.885 ± 0.015 for the contribution from pure γ^* exchange and Z/γ^* interference, the inclusive $Z \to \mu^+\mu^-$ cross section is found to be:

$$\sigma\,(Z) = 290.1 \pm 3.0(\text{stat.}) \pm 7.4(\text{syst.}) \pm 18.9(\text{lumi.}) \;\; \text{pb.}$$

Finally, comparisons of W and Z boson p_T distributions as measured with DØ during Run I of the Tevatron are compared to HERWIG and MC@NLO predictions. Relevant parameters in the simulations are tuned to obtain the best possible fit to the data. An excellent agreement is found for both HERWIG and MC@NLO.

Declaration

No portion of the work referred to in this thesis has been submitted in support of an application for another degree or qualification of this or any other university or other institute of learning.

The Author

The author was educated a [redacted] before gaining a first class MPhys degree from the Department of Physics and Astronomy at the University of Manchester in 2001. The work presented here was undertaken in Manchester and Fermilab, Illinois in 2001–2005.

Acknowledgements

First and foremost I owe a huge debt of gratitude to my supervisors, Mike Seymour and Terry Wyatt. I feel privileged to have worked closely with two excellent physicists from both the experimental and theoretical sides of the field. Both have taught me complementary skills and ways of thinking. Thank-you for all your encouragement. Thanks also to other members of the department who have given me help and advice along the way. Thanks to Fred Loebinger for making himself so approachable and for dragging me down to the coffee area for much needed breaks.

Working in a collaboration the size of DØ it is difficult to acknowledge everyone that contributed to the progress of my PhD. I will attempt to mention people that I feel made a direct impact during my time at Fermilab. Thanks to Gavin Hesketh for allowing me to step into his shoes and for the helpful comments he gave me after wading through this thesis. Thanks to Simon Dean for always being willing to help and always having time no matter how busy he was himself. Thanks to Michiel Sanders for helping me get to grips with the DØ software. Thanks to Paul Telford, my 'Monte Carlo monkey', for being a very capable colleague and making me laugh during the long pre-conference nights in deepest, darkest Fermilab. I would also like to thank members of the WZ and Muon ID groups for helpful hints and encouragement along the way, in particular Marco Verzocchi and Frédéric Déliot.

Thanks to the UK posse and other friends at Fermilab for making it so much fun. Thanks to Tamsin for sharing my life out there and for being such a good friend.

Thanks to all my friends in Manchester and the rest of the country for keeping life fun and helping me forget about my thesis. Thanks to my family for their unconditional support and love throughout my entire life. Thanks to Matt for being there for me through it all, and for making everything right.

Lastly, I would also like to thank PPARC, for making it all possible by funding my PhD and allowing me to have a fantastic year in Chicago.

Chapter 1

Introduction

Particle physics is the study of the fundamental building blocks of our Universe and the interactions between them. Historically, what is meant by a fundamental particle has changed as physicists' knowledge has improved and achievable energies have increased. Currently, the world's highest energy particle accelerator is the Tevatron, which collides protons with antiprotons at a centre of mass energy of 1.96 TeV. One of the many processes that occur when the protons and antiprotons collide is the production of the massive W and Z bosons. This thesis presents the measurement of the inclusive $Z/\gamma^* \rightarrow \mu^+\mu^-$ cross section as well as studies of W and Z boson properties using DØ, a general purpose detector at the Tevatron. The remainder of the thesis is set out as follows.

Chapter 2 introduces the Standard Model, the current theoretical description of the fundamental particles and their interactions. Chapter 3 serves as an introduction to the experimental apparatus used throughout the thesis: the Tevatron and the DØ detector that detects and measures the properties of many different particles. The production and properties of W and Z bosons at the Tevatron as well as motivation for the work described in the rest of the thesis are given in Chapter 4. The invaluable Monte Carlo programs that simulate the processes occurring at particle colliders, enabling sophisticated analysis of the data, are introduced in Chapter 5. The measurement of the inclusive $Z/\gamma^* \rightarrow \mu^+\mu^-$ cross section as well as that of $Z \rightarrow \mu^+\mu^-$ is described in Chapter 6. Comparisons of the measured W and Z boson momentum distributions with Monte Carlo predictions are described in Chapter 7. Parameters in the Monte Carlo are tuned to obtain the best possible fit to the data. Finally, Chapter 8 summarises the work described and puts it in context with the bigger

picture of present day condel physics research.

Chapter 2

The Standard Model of Particle Physics

The Standard Model of particle physics is a mathematical description of the fundamental building blocks of matter and the interactions between them. These building blocks are portrayed as structureless, point-like particles that cannot be decomposed into anything else. This chapter will serve as a brief introduction to the Standard Model (SM) and the particles and forces that it describes.

The SM describes the Universe in terms of Quantum Field Theories, the mechanics of which are formulated from the theory's Lagrangian density. Matter particles are described as fermionic (spin-$\frac{1}{2}$) excitations of relativistic quantum fields. There are 12 fundamental fermions, grouped into two classes — leptons and quarks. There are three families in each class, containing particles of similar properties but differing mass. Each of the lepton families contains one particle with an electric charge[1] of -1 and one electrically neutral particle. Each of the quark families contains a quark with electric charge $+\frac{2}{3}$ and a quark with electric charge $-\frac{1}{3}$. For every existing particle there also exists an associated antiparticle, which is the same as its corresponding particle in properties such as mass and spin, and opposite in properties such as charge and magnetic moment. Table 2.1 summarises the fundamental fermions and the interactions in which they participate. Interactions between matter particles are introduced into the theory by imposing symmetry conditions on the quantum fields that represent them. The Lagrangian of the theory is required to be invariant under a group of *local* phase changes, where local means that the phase change depends on

[1] All charges are given in units of the absolute value of the electron charge, 1.602×10^{-19} Coulombs.

	I	II	III	charge	interactions
leptons	ν_e (electron-neutrino)	ν_μ (muon-neutrino)	ν_τ (tau-neutrino)	0	weak
	e (electron)	μ (muon)	τ (tau)	-1	EM/weak
quarks	u (up)	c (charm)	t (top)	$+\frac{2}{3}$	strong/EM/weak
	d (down)	s (strange)	b (bottom)	$-\frac{1}{3}$	strong/EM/weak

Table 2.1: *The fermions of the Standard Model. The mass of the particles increases with family I → II → III, apart from the neutrinos whose masses are negligible. The charges given are electric charges.*

the space-time coordinates. Such phase changes are known as gauge transformations. Since the equations of motion contain space-time derivatives, lagrangians will not trivially be invariant under such transformations. In order to restore invariance an additional gauge field is added to the theory which ensures that the equations of motion remain unchanged. Excitations of these gauge fields are interpreted as the force-carrying spin-1 bosons that mediate the interactions of nature; the theory now describes interactions between particles.

There are four known fundamental forces that act in nature: the strong force, the weak force, electromagnetism and gravity. All but the latter are described within the SM via the exchange of one of the force-carrying bosons, which are summarised in Table 2.2.

gauge boson	interaction
γ (photon)	EM
Z^0 boson	weak
$W^\pm$ bosons	weak
g (gluon)	strong

Table 2.2: *The force-carrying gauge bosons of the Standard Model.*

2.1 Electroweak Theory

The theory of electromagnetism, Quantum ElectroDynamics (QED), is a gauge theory invariant under the U(1) group of transformations. Here, U(1) means a group of unitary one-dimensional matrices: space-time dependent rotations in a complex plane. Forcing the theory to be invariant under U(1) transformations introduces the photon field. QED describes interactions between the photon and charged particle fields.

A standalone theory for weak interactions was harder to formulate. However, Glashow [1], Weinberg [2] and Salam [3] found that it was possible to have a unified theory for both electromagnetism and the weak force — the electroweak theory. It is formulated from a new U(1) group and an SU(2) group, such that the theory is invariant under SU(2)$\otimes$U(1) transformations. SU(n) designates the group of Special, Unitary $n \times n$ matrices. Here, special means that the determinant of the matrices must be 1, instead of $e^{i\phi}$, as is the case for U(n). Since an $n \times n$ unitary matrix with the condition that det U $= 1$ has $n^2 - 1$ free parameters, such a group will have $n^2 - 1$ matrices known as *generators*. Invariance of the theory under the SU(n) transformations introduces an interacting gauge boson field for each generator. For $n > 1$, matrices are in general non-commutative; theories with generators that do not commute are known as non-Abelian. This leads to the important result that the gauge bosons of the theory are self interacting. The generators of SU(2) correspond to the W^-, W^0 and W^+ bosons. When the U(1) group is added, interactions with the B^0 boson are introduced. The W^0 and B^0 mix quantum mechanically and orthogonal states form the Z^0 boson (associated with the weak interaction) and the photon (associated with the electromagnetic interaction). For the remainder of this thesis the Z^0 boson will be denoted the Z boson and the $W^\pm$ bosons will be generically denoted the W boson.

Physical quantities, such as the rate at which a particular process occurs, cannot be exactly calculated in Quantum Field Theories. In order to demonstrate this point, consider the simple process of electron-positron annihilation to form a photon that decays to a muon-antimuon pair, $e^+e^- \rightarrow \gamma^* \rightarrow \mu^+\mu^-$, which is represented graphically in a Feynman diagram in Figure 2.1(a). Such a process is indistinguishable from the process shown in Figure 2.1(b), which corresponds to the same final state, but has an additional photon loop connecting the final state fermion lines. It is also

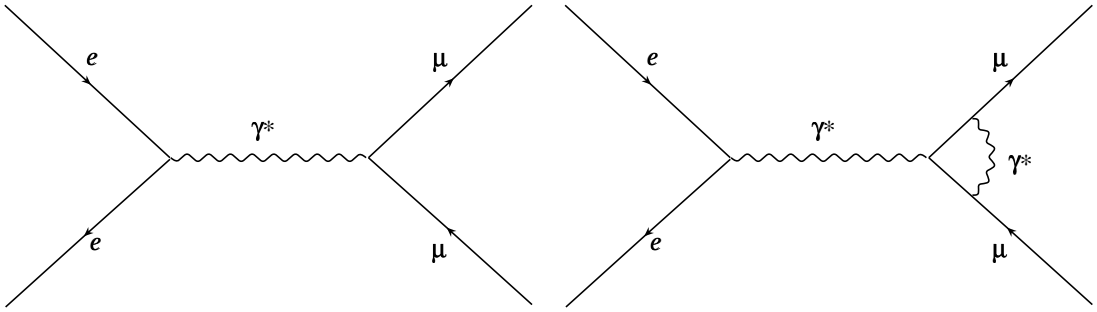

Figure 2.1: *Feynman diagram of the process* $e^+e^- \to \gamma^* \to \mu^+\mu^-$. *(a) First order process. (b) The same process with an additional photon loop.*

indistinguishable from infinitely many other diagrams with more loops. A full calculation would have to take into account all of these diagrams. Since each successive diagram contains more interaction vertices the rate will contain an additional factor of the coupling constant of the interaction, and the physical quantity forms a power series with successive terms containing higher powers of the coupling constant. If the coupling is small the perturbative series will converge and higher order terms will become negligible compared to the leading terms.

Loop diagrams, such as Figure 2.1(b), contain infinities. The momenta of the particles within the loop are not constrained and can therefore extend to infinity, causing calculations to diverge. This problem is solved via the principle of *renormalisation*. Let us consider for a moment what is meant by the electron charge and other parameters in the theory. The electron charge is measured by its electromagnetic interactions with other charged particles. These interactions will also suffer from the same problem of higher order loop corrections. What we call the electron charge is therefore not the *bare* electron charge, but a physical quantity that is affected by electromagnetic interactions. If this measured quantity is used in the calculation of the process, the divergences have, in effect, been absorbed into the physical electron charge. Different types of divergences are treated in the same way, by being absorbed into different physical parameters. A theory is only renormalisable if a finite set of such input parameters is required. The physical parameters are expressed

in terms of the bare parameters and the expression contains some arbitrary finite functions. Different choices made for these functions constitute different *renormalisation schemes*. One such scheme, known as the modified minimal subtraction ($\overline{\text{MS}}$) scheme [4], subtracts certain universal constants that appear in all cross sections, and sets the remainder of the arbitrary functions to zero. Most renormalisation schemes, including $\overline{\text{MS}}$, introduce an unphysical scale called the *renormalisation scale*, μ. The coupling constant of the theory becomes a function of μ, as do the coefficients of perturbative expansions, in such a way that if calculated to infinite orders, the result would be independent of μ. However, truncating the series at a finite order leaves some remaining μ dependence. The usual prescription is to set μ equal to the typical energy scale associated with the process of interest.

Accurate calculations can now be made by performing the calculation to a certain order in perturbation theory. By using such methods, predictions of the electroweak theory have been tested experimentally to an extremely high precision — the theory has proved incredibly successful.

There is, however, a remaining problem with the electroweak theory: that its particles are massless. This is in direct conflict with what is observed in nature. If mass terms for the particles were simply added to the Lagrangian, the gauge symmetry would be broken. This problem is solved through a process known as *spontaneous symmetry breaking* where a theory, symmetric with respect to some group, has degenerate ground state (vacuum) solutions. Choosing a solution spontaneously breaks the symmetry of the system. Within the framework of the SM this is achieved via the *Higgs mechanism* [5]. A scalar field, known as the Higgs field, with a potential function of a form allowing degenerate vacuum solutions with a non-zero vacuum expectation value, is introduced. Other particles acquire mass through interactions with this field, with the value of the mass dependent on the strength of the coupling.

2.2 The Strong Force

The theory of the strong force, Quantum ChromoDynamics (QCD), is an SU(3) gauge theory. Strongly interacting particles carry a type of charge known as *colour*. All (anti)quarks carry a colour charge that can be (anti)red, (anti)blue or (anti)green. The $3^2 - 1 = 8$ generators of QCD represent massless gluons that themselves carry

colour charge and differ by their colour quantum numbers.

In contrast to QED, the coupling strength of QCD decreases as the energy scale increases or the distance scale decreases. This property is known as asymptotic freedom, and it means that perturbative calculations are not possible at low energies and long distances; in this region it is necessary to describe nature using approximate, non-perturbative models. Asymptotic freedom is believed to lead to the confinement property of objects that carry colour charge. They are never found as free particles in nature, instead they are always confined into colour-neutral composite objects known as hadrons. Just as neutral electric charge can be achieved by the addition of two opposite charges, neutral colour charge can be achieved by the addition of all three colour charges, all three anticolour charges or a colour charge with its equivalent anticolour charge. Hadrons can therefore be one of two types: (anti)baryons consist of three (anti)quarks each with a different (anti)colour and mesons consist of a quark with a colour and an antiquark with the equivalent anticolour. The proton is an example of a baryon and consists of two u quarks and one d quark. These *valence* quarks within hadrons will interact with each other via the exchange of gluons; the gluons can themselves emit more gluons or split into quark-antiquark pairs, forming a *sea* of quarks and gluons. Quarks and gluons are collectively known as partons. The description of hadrons, in terms of these constituent point-like particles, is known as the parton model. Since the strong force decreases in strength as the scale of the interaction increases, a hadron probed at a high energy will approximately consist of non-interacting partons.

When the calculation of a hadronic cross section is performed it is split into two parts in accordance with the *factorisation theorem*. The two parts are separated in energy by the *factorisation scale*, μ_F. The first part is low energy, partly non-perturbative, QCD that goes on within the hadron. This is described by Parton Distribution Functions (PDFs), which give the momentum distributions of constituent partons. The PDFs are universal and process independent; they are determined from fits to data using many different processes at different experiments. The probability of finding a parton of type i with a fraction of the hadron momentum between x and $x + dx$, is given by $f_i\left(x, \mu_F^2\right)dx$, where $f_i\left(x, \mu_F^2\right)$ is the PDF. Although it is not possible to derive PDFs from first principles, their evolution as a function of μ_F is predictable in perturbation theory. The second part is the perturbative, hard

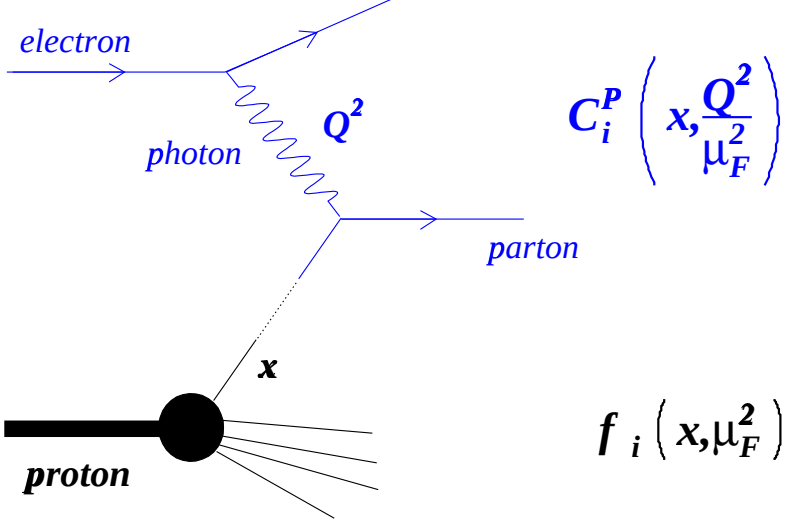

Figure 2.2: *Schematic view of Deep Inelastic Scattering. An electron exchanges a virtual photon with a proton. The cross section for the process can be factorised into the two parts separated in colour.*

partonic interaction, which can be calculated from first principles.

Factorisation can be illustrated with the example of Deep Inelastic Scattering (DIS) where an electron exchanges a virtual photon with a proton, as is illustrated in Figure 2.2. The cross section can be expressed as:

$$\sigma = \sum_i f_i\left(x,\mu_F^2\right) \otimes C_i^P\left(x,\frac{Q^2}{\mu_F^2}\right), \tag{2.1}$$

where $C_i^P\left(x,\frac{Q^2}{\mu_F^2}\right)$ are the partonic cross sections for parton i, $f_i\left(x,\mu_F^2\right)$ are the PDFs, $Q^2 = -q^2$ (minus the four-momentum squared of the virtual photon) and the $\otimes$ symbol denotes convolution over x values.

When cross sections are calculated to greater than leading order in perturbation theory, it is necessary to include both virtual corrections (those including additional loops) and real corrections (those including additional external lines). Higher order corrections result in divergences in the soft and collinear limits of parton emission. For fully inclusive quantities the virtual and real divergences exactly cancel giving a finite result. For more exclusive quantities the divergences do not completely cancel and logarithmic terms that become large in the soft and collinear limits appear. This complication can be overcome via a technique known as *resummation*. Leading Logarithmic (LL) terms have a form similar to $\alpha_S^n L^n$, where α_S is the strong coupling

constant and L represents the logarithmic term. The Next to Leading Logarithmic (NLL) terms have the form $\alpha_S^n L^{n-1}$, the Next to Next to Leading Logarithmic (NNLL) terms have the form $\alpha_S^n L^{n-2}$, and so on. The LL terms can be summed to all orders in perturbation theory to a closed form that gives a finite result, this is the Leading Log Approximation (LLA). Similarly the NLL terms can be summed to a more complicated closed form, which together with LL terms gives the NLLA. These approximations take into account the enhanced regions of phase space to all orders in perturbation theory.

If a parton is a final state particle of an interaction it will emit more partons that will in turn emit more. Since isolated partons cannot propagate over macroscopic distances, they will combine into *jets* of hadrons through a process known as hadronisation. The observed final state will be a jet rather than a quark.

2.3 Unanswered Questions in Particle Physics

The SM combines the electroweak and QCD theories to form an SU(3)⊗SU(2)⊗U(1) description of the Universe which has proved to be extremely successful. It has predicted new particles that have later been discovered and predicted relationships between parameters that have been verified to a high precision.

Despite such success there are still some problems with the SM as it stands today. One major outstanding issue is direct evidence for the predicted Higgs field, responsible for the generation of mass terms for SM particles. Excitations of this field lead to a particle known as the Higgs boson. The Higgs boson has never been observed in experiments and if it does not exist then the SM is evidently incomplete.

Even if the Higgs is found, we know that the SM cannot be the whole story. The mass of the Higgs, m_{H}, is constrained by other SM parameters to be of the same order as the electroweak scale[2] $\sim$ 100 GeV. Loops of virtual SM particles lead to quantum corrections to m_{H} of the order of the highest energy scale at which the SM is valid; this could be as large as the Planck scale, $m_{\mathrm{P}} \sim 10^{19}$ GeV, which represents the energy at which quantum gravity effects become important. The cancellation of such corrections to get m_{H} down to the electroweak scale is extremely unnatural.

[2]Here, and throughout the rest of the thesis, natural units will be used, with $\hbar = c = 1$. Energies, momenta and masses can therefore all be expressed in terms of electron volts, eV, where $1\ \mathrm{eV} = 1.6 \times 10^{-19}$ Joules.

This issue is known as the *hierarchy problem*. There are a number of theories that address the hierarchy problem, the most popular being the theory of supersymmetry, which predicts a host of as yet undetected massive particles whose quantum loop corrections cancel those of the SM particles.

There are many other unsatisfactory features of the SM. It does not include gravity, the weakest of the fundamental forces. A theory excluding gravity is clearly an incomplete theory of the entire Universe. A lot of the parameters, such as the particle masses and field coupling strengths, are free parameters that have to be measured in experiments and cannot be predicted. It is not known why there are 12 fermions or why the different generations have such hugely differing masses.

There is also some experimental evidence for Beyond the Standard Model (BSM) physics. It has recently been discovered that neutrinos have a small but non zero mass whereas the SM describes them as massless, a clear discrepancy. The fact that the majority of matter in our Universe is invisible to us, which cannot be explained within the SM, suggests that there is some BSM massive particle out there making up the dark matter that we cannot see. Low mass neutrinos have been considered as a *hot* dark matter candidate, here hot means that the particles are moving at close to the speed of light. However, the matter distribution in the Universe can only be explained by *cold* dark matter and the likely candidate is an as yet undiscovered BSM particle.

One of the main aims of particle physics experiments is to try and find new massive particles from BSM theories as well as the Higgs boson. Another of the main approaches employed by particle physics experiments in an attempt to try and further test the SM and search for physics beyond it, is the measurement of SM parameters to higher and higher precision. Although the SM does not predict the exact values of parameters, it does predict relationships between them. The parameters that can be most accurately measured in experiments are put back into the theory in order to predict the values of remaining parameters. In order to really test the theory it is necessary to make more measurements than there are free parameters. If this is not done then it is always possible to adjust the parameters to fit the data. Measurements made to over constrain the theory in this way are known as precision measurements, any deviation from the measured and predicted values of such parameters suggests BSM physics. One important example is the relationship between the mass of the

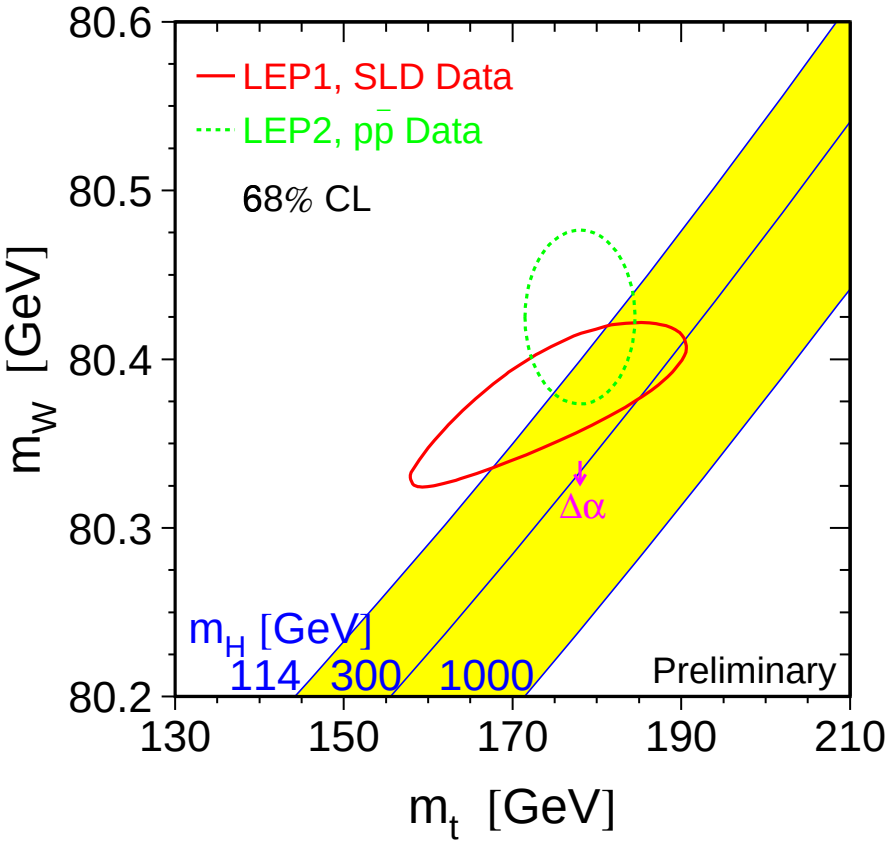

Figure 2.3: *m_{W} as a function of m_{t}. The green ellipse shows the direct measurements. The red ellipse shows the indirect measurements. The yellow bands show the expected mass of the SM Higgs in the $m_{\mathrm{W}} - m_{\mathrm{t}}$ plane.*

W boson, m_{W} and that of the top quark, m_{t}. Figure 2.3 shows a plot taken from [6] of m_{W} versus m_{t}, measured both directly and indirectly. The direct measurements come from the experiments at the Tevatron and the Large Electron Positron collider (LEP) at CERN, Geneva. The indirect measurements come from LEP and the SLAC Large Detector (SLD). SLAC is the Stanford Linear Accelerator Centre in California. The measurements agree within their current uncertainties. A decrease in the uncertainties of the direct measurements will further constrain the SM as well as the mass of the elusive Higgs boson, m_{H}. This link between theoretical predictions and models and experimental measurements is known as *phenomenology*. The following chapter serves as an introduction to the experimental apparatus required to make such measurements.

Chapter 3

Experimental Apparatus

3.1 Particle Accelerators

In order to probe tiny distance scales and to create massive particles, it is necessary to create a huge amount of energy. This can be achieved by accelerating charged particles, using oscillating electromagnetic fields, to high energies before colliding them together or into a fixed target. There are two types of accelerator, linear and circular. The former collide particles that are travelling in a straight line and the latter collide particles that are travelling in opposite directions around a ring. In circular accelerators the moving particles are kept in a circular orbit using magnets. One type of particle is travelling in a beam in one direction and another (or the same) type is travelling in a beam in the other direction. At certain points around the ring the two beams are focused onto each other and the particles collide. High centre of mass energies are achievable through repetitive acceleration as the particles circulate many times around the ring. This enables the creation of many different types of particle; the collision point is surrounded by a large detector which has the job of identifying these particles and measuring their properties.

3.2 The Tevatron

The Tevatron is a circular accelerator, situated at the Fermi National Accelerator Laboratory (Fermilab) near Chicago in the USA. It is 6.3 km in circumference and collides protons and antiprotons travelling at close to the speed of light. During Run I of the Tevatron (1992–1996) it ran with a centre of mass energy of 1.8 TeV. Run II

began in 2001 and will continue until about 2009. It currently runs at a centre of mass energy of 1.96 TeV, making it the highest energy accelerator in the world.

The Fermilab Tevatron complex consists of a number of accelerators and storage rings. Figure 3.1 shows a schematic view of the accelerator chain. The process

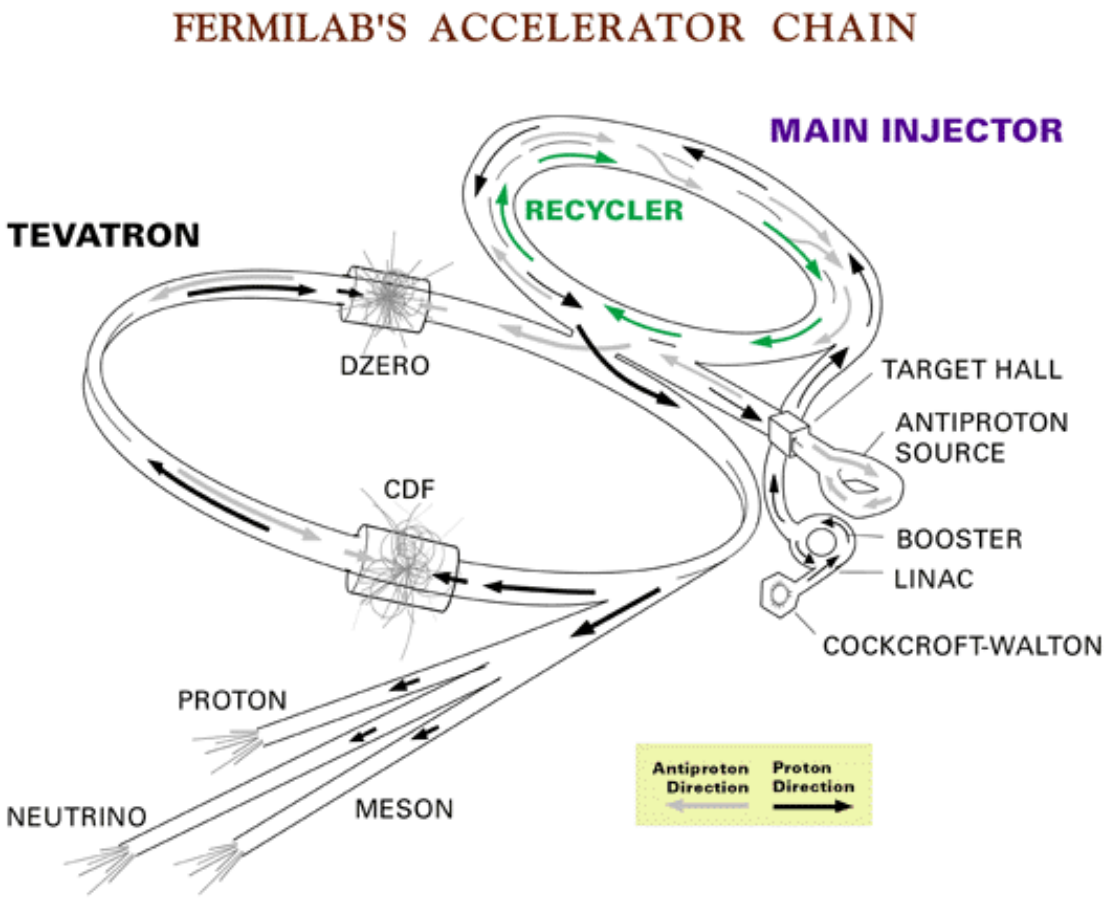

Figure 3.1: *The accelerator chain at Fermilab.*

begins inside the Cockcroft-Walton pre-accelerator, where H^- ions are formed by ionising Hydrogen gas and accelerated by a positive voltage to 750 keV. The H^- ions subsequently enter a 150 m linear accelerator (the Linac) where oscillating electric fields accelerate them to 400 MeV. Once at this energy they are passed through a Carbon foil which strips off the electrons leaving behind a beam of protons. The protons enter the circular Booster where they are accelerated to an energy of 8 GeV. The next stage in the journey is the Main Injector which has two important jobs:

1. Accelerate the protons to 120 GeV (to be used as an antiproton source).

2. Accelerate the protons and antiprotons to 150 GeV (to be injected into the Tevatron).

The antiprotons are formed in the Antiproton Source where the 120 GeV protons from the Main Injector collide with a stationary Nickel target. Many particles are formed after the protons interact with the nuclei in the target; antiprotons are separated out and introduced into the Debuncher where they are formed into a coherent beam. The antiproton beam is then stored in the Accumulator ring until there is a sufficient number to introduce into the Main Injector. The Main Injector forms the 150 GeV protons and antiprotons into a bunch structure before injecting them in opposite directions into the Tevatron, where their energy is increased until it reaches 0.98 TeV, giving a centre of mass energy of 1.96 TeV.

The Tevatron beam consists of 36 proton and 36 antiproton bunches arranged into three groups of 12, named super-bunches. There is 2 μs between each super-bunch and 396 ns between each bunch inside a super-bunch. The are $\sim 10^{11}$ protons and $\sim 10^{10}$ antiprotons per bunch, resulting in an average of 2 proton-antiproton ($p\bar{p}$) interactions per bunch crossing at an instantaneous luminosity[1] of $5 \times 10^{31} cm^{-2} s^{-1}$.

The beams are kept apart for most of their journey around the Tevatron and are only focused onto each other at two points. These points are surrounded by huge multipurpose detectors, CDF and DØ. Before describing the detector used in this thesis (DØ), it is worthwhile to say a few words about the particle interactions with matter that enable their detection.

3.3 The Detection of Particles

When a particle passes through matter the following types of interaction can take place:

1. Excitation and ionisation of atoms.

2. Photon radiation (bremsstrahlung) and electron-positron pair production.

3. Short range interactions with nuclei.

[1]Luminosity is a measure of the beam intensities, determined by the density of particles in the beams. The instantaneous luminosity gives a measure of the rate of collisions at any given time and the integrated luminosity gives a measure of the total number of collisions over a given time period. An integrated luminosity is usually given in terms of pico- (pb) or femto-barns (fb), where 1 barn = 10^{-24} cm^2.

The first two are due to electromagnetic interactions and the last is due to the weak or the strong force. The following sections describe each of these interactions in turn.

3.3.1 Excitation and Ionisation of Atoms

When a charged particle passes by an atom it can exchange a photon with an atomic electron, exciting it to a higher energy level, or completely stripping it from the atom: ionisation. High energy charged particles can produce electrons with a considerable amount of kinetic energy, known as *knock-on* electrons, which are able to free more electrons from atoms which go on to free more. When a photon passes through matter it can also interact with the atomic electrons.

3.3.2 Photon Radiation and Pair Production

A charged particle passing by an atom can interact electromagnetically with the atomic nucleus, leading to the emission of a photon. This photon radiation is known as bremsstrahlung. In a similar way, a photon passing by an atom can interact with the nucleus to form an electron-positron pair, this is known as pair production.

3.3.3 Short Range Interactions With Nuclei

Any strongly interacting particle passing through a medium can interact with atomic nuclei via the exchange of a gluon. In the case of neutrinos that do not interact via the strong or the electromagnetic forces, a weak interaction can take place. This interaction is, however, *so* weak that neutrinos are not directly detectable in general purpose detectors.

3.4 The DØ Detector

This section will serve as an introduction to DØ and the way in which it identifies and measures the properties of different particles. For a more detailed description of the DØ detector the reader is referred to [7].

Most collider detectors are composed of different sub-systems that surround each other like onion skin layers. Figure 3.2 shows a schematic view of the DØ detector. The DØ sub-systems, which are described in the following sections, include:

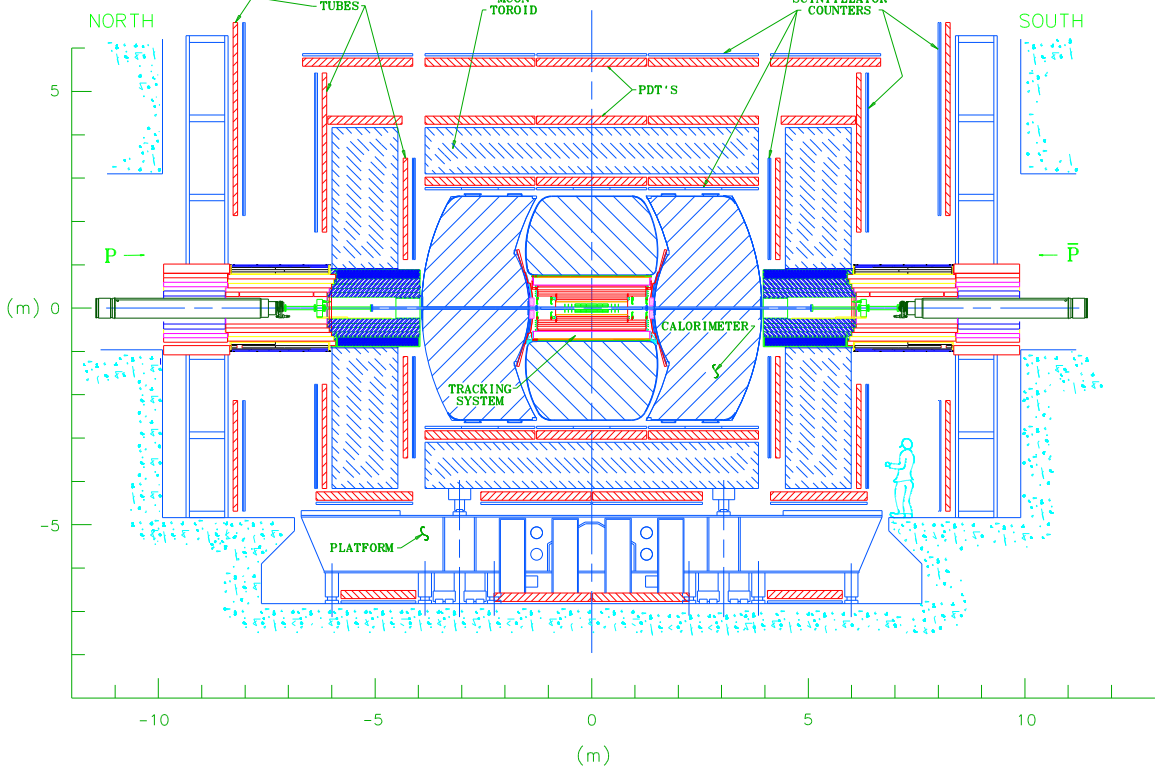

Figure 3.2: *A cross section view of the DØ detector.*

1. Central Tracking System [section 3.4.2]:
   - Silicon Microstrip Tracker (SMT).
   - Central Fibre Tracker (CFT).
   - Solenoid magnet.
2. Calorimetry [section 3.4.3]:
   - Preshower detectors.
   - Calorimeter.
3. Muon System [section 3.4.4].
4. Luminosity Monitor [section 3.4.5].

3.4.1 Coordinate System

DØ uses a right handed coordinate system. The proton beam defines the positive z axis, the y axis points vertically upward and the x axis points towards the centre of

the Tevatron ring, with the DØ detector centered at (0,0,0).

The azimuthal angle, $\phi = \tan^{-1}\left(\frac{y}{x}\right)$, and the polar angle, $\theta = \tan^{-1}\left(\frac{r}{z}\right)$, where r denotes the perpendicular distance from the beam axis, are also used. Unless otherwise indicated, all measurements in ϕ and θ will be given in radians. Since constituent partons carry a varying amount of their parent hadron's momentum, DØ is generally not in the centre of mass frame of each collision. The polar angle is therefore often replaced by *pseudo-rapidity*, $\eta = -\ln\left(\tan\left(\frac{\theta}{2}\right)\right)$, which approximates to the true rapidity, $y = \frac{1}{2}\ln\left(\frac{E+p_z}{E-p_z}\right)$, for relativistic particles. Differences in rapidity are invariant under a Lorentz boost in the z direction, making it a more convenient coordinate.

The direction of the track can be used to define η, this is known as 'physics-η' or η_{phys} and is independent of the z-position of the track. Alternatively, η can be calculated using the origin (0,0,0) and the z-position at a particular detector. For example, η_{CFT} denotes η at the point where the particle exits the CFT detector. Since the luminous region of collisions at DØ has a large spread in z, this can differ significantly from η_{phys}. The bending of particle tracks in the magnetic fields causes ϕ to vary slightly at different point in the detector.

3.4.2 Central Tracking System

The central tracking system consists of two tracking detectors, the SMT and the CFT, that record the passage of charged particles. Both detectors are immersed in a 2 Tesla, superconducting, solenoid magnet. The magnet will cause charged particles to bend in the $r - \phi$ plane. A measurement of the extent of curvature enables a measurement of the particles' momenta in the direction perpendicular to the beam, known as transverse momentum, p_T.

Silicon Microstrip Tracker

Silicon detectors are semi-conductor tracking devices used for high precision position measurements. They provide good momentum resolution and measurements of a particle track's *dca*. The magnitude of the *dca* is the *distance of closest approach* of the muon track to the beam spot position in the $x - y$ plane and the sign depends on

which side the track passes the beamspot in the $x-y$ plane.[2] Silicon detectors consist of n-type silicon wafers with strips of p^+-type silicon implanted on one surface for single-sided detectors and additional n^+-type silicon strips on the opposite surface for double-sided detectors.[3] The passage of a charged particle through the wafers results in excitation of electrons from an energy level in the valence band to one in the conduction band, creating a free electron-hole pair. The ionised charge collects on the nearest surface strip and is used to measure the position of the particle. The double-sided detectors have the n^+- and p^+-type strips offset at a stereo angle to each other allowing the reconstruction of the tracks in three dimensions.

The DØ SMT, shown in Figure 3.3, directly surrounds the beam pipe. The SMT

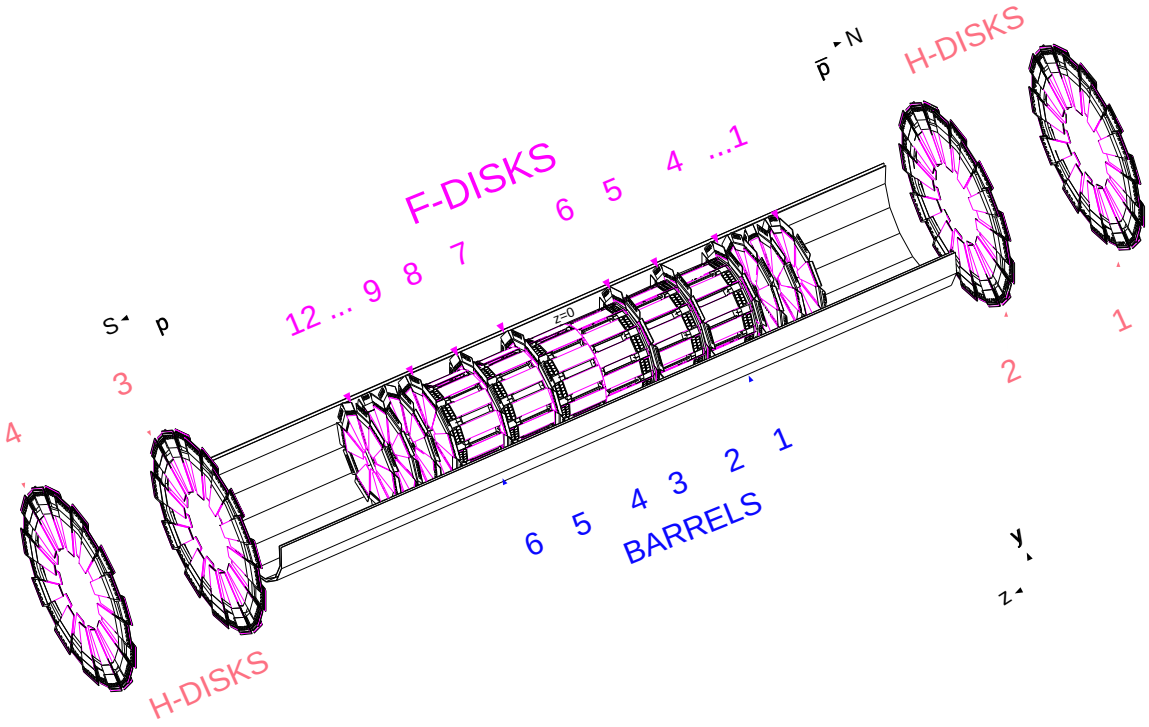

Figure 3.3: *The Silicon Microstrip Tracker at DØ.*

was designed to maximise tracking for the full η acceptance of DØ. The task was complicated by the fact that the luminous region of collisions has a large spread in z. The resulting design consists of both barrel and disk components. The barrels contain four co-axial layers of wafers, equally spaced in the region $2.5 < r < 10$ cm. All four layers have *axial* strips running parallel to the beam, allowing the measurement of

[2] If the track is drawn pointing directly upwards in the $x-y$ plane and it passes to the left of the beamspot the *dca* is positive; if it passes to the right of the beamspot the *dca* is negative.

[3] The + in n^+ and p^+ denotes a higher than usual concentration of charge carriers.

the $r-\phi$ coordinate of tracks. Layers one and three are double-sided detectors with a stereo angle of 90° (apart from those in the outermost barrels which are single-sided). Layers two and four are also double-sided with a stereo angle of 2°. The stereo angles allow an $r-z$ measurement. There are two types of disk, the F-disks and the larger H-disks, both with wafers perpendicular to the beam. The F-disks consist of double-sided wafers with a stereo angle of ±15°. They have an inner radius of 2.6 cm and an outer radius of 10 cm. The H-disks are made of single-sided wafers with an inner radius of 9.5 cm and an outer radius of 26 cm.

There are six barrels covering the region $|z| < 39$ cm. There is an F-disk positioned at the end of each barrel and an additional three are positioned at either end of the barrel region. Situated at $z = \pm 110$ cm and $z = \pm 120$ cm are four H-disks, which help to extend the SMT coverage to $|\eta| \sim 3$.

Central Fibre Tracker

Fibre trackers work on the principle that certain materials produce scintillation light, which is in or near the visible spectrum, when atomic electrons are excited by the knock-on electrons produced by passing charged particles. In this case scintillating fibres produce light in the yellow-green part of the visible spectrum. Doublet layers of fibres are mounted on eight concentric cylinders in the axial direction providing an $r-\phi$ measurement. Each cylinder supports an additional doublet layer of fibres at alternating stereo angles of ±3°, allowing three-dimensional reconstruction of tracks. The dimensions of the eight cylinders are shown in Table 3.1.

Cylinder	Radius (cm)	Extension in z (cm)
1	19.5	± 83
2	23.4	± 83
3	28.1	± 128.5
4	32.8	± 128.5
5	37.5	± 128.5
6	42.1	± 128.5
7	48.8	± 128.5
8	51.5	± 128.5

Table 3.1: *The dimensions of the cylinders in the Central Fibre Tracker.*

Scintillation light collected in the fibres, which are double clad to improve the light yield, is transmitted via internal reflection in both directions. At one end an aluminium mirror reflects the light back in the opposite direction. The other end is connected to fibre waveguides that conduct the light to Visible Light Photon Counters (VLPCs). The VLPCs are solid state devices that convert the collected photons to an electronic signal via electron-hole pair creation. They have a high gain of up to 50,000 electrons per incoming photon. The CFT provides optimal tracking up to $|\eta_{CFT}| \sim 1.6$.

Momentum Resolution

The momentum resolution of the DØ central tracking system can be parameterised [8] as:

$$\frac{\sigma_{1/p_T}}{1/p_T} = \sqrt{\frac{(0.0028 \times p_T)^2}{L^4} + \frac{0.0258^2}{L \sin(\theta)}}. \tag{3.1}$$

Here, L is the tracking bending lever arm, defined as follows:

$$L = \begin{cases} 1, & \text{if } |\eta_{phys}| < 1.62; \\ \frac{\tan(\theta)}{\tan(\theta_{CFT})}, & \text{otherwise,} \end{cases} \tag{3.2}$$

where θ_{CFT} denotes the value of θ where $|\eta_{phys}| \equiv 1.62$. The purpose of L is to model the degradation of the resolution with the fall off of the CFT.

3.4.3 Calorimetry

In particle physics experiments calorimetry has the role of measuring the energy and position of particles by their total absorption. The basic principle is that passing particles interact with a medium and consequently lose their energy to it; the energy loss is then measured.

When a high energy ($\gg$ 10 MeV) electron passes through a material with a high atomic number, the primary mechanism of energy loss is bremsstrahlung. Similarly, the dominant interaction for high energy photons is pair production. The secondary particles produced in these processes will themselves undergo bremsstrahlung and pair production and so on, forming what is known as an electromagnetic shower. The particles at the end of the shower will share the energy of the original electromagnetic particle. When the shower particles have a low enough energy, ionisation becomes the dominant form of energy loss, thus these end particles are detected via the ionisation of atoms.

Hadronic particles passing through a material interact with the atomic nuclei via the strong force. Secondary particles are produced that go on to produce more particles with decreasing energy in what is known as a hadronic shower. The average distance travelled by particles in a hadronic shower before an interaction is typically longer than that in an electromagnetic shower meaning that they will penetrate further. The low energy charged particles at the end of the shower will be detected by ionisation. Neutral hadrons can be detected by the production of secondary charged particles.

Preshower detectors

The preshower detectors combine both tracking and calorimetry to improve position and energy measurement as well as particle identification. In the central region ($|\eta| < 1.2$) the dense material of the solenoid magnet acts as an absorber, causing some showering. Here, an additional layer of lead is added to the edge of the solenoid to increase the amount of absorbing material. Three layers of scintillating material lie outside the lead to detect charged particles. In the forward region ($1.4 < |\eta| < 2.5$) there is no solenoid coverage. There are three layers of scintillators with a layer of lead between the first and second layers.

Calorimeter

The DØ calorimeter is segmented into cells. Each cell consists of layers of absorbing material, to induce shower formation, and active layers of liquid argon, where atoms are ionised by the passage of charged particles. Calorimeters that have alternating absorption and active layers are known as sampling calorimeters. The ionised charge is collected on a copper plate located in each cell. The energy of a traversing particle or jet is found by adding up the charge collected from all of the cells that it passes through. The calorimeter must be calibrated so that the observed charge can be converted into an energy measurement.

In most calorimeters the fraction of energy deposited by a hadron is less than that deposited by an electron or a photon, since more of it is released in an undetectable form. DØ has a compensating calorimeter where the fraction of energy is the same. This is achieved by using uranium as the absorber layers. Low energy neutrons, from the nuclear breakup in hadronic showers, cause fission in the uranium and energy is

converted into charged particles by the β decay of the fission products.

There are three modules that make up the calorimeter: the Central Calorimeter (CC) and a pair of End Calorimeters (ECs). The CC has a cylindrical shape covering the inner detectors and the ECs are situated at either end of them. Both the CC and the ECs consist of tiers of cells. The first four tiers make up the ElectroMagnetic (EM) calorimeter, the absorption layers in these cells are plates of uranium 3-4 mm thick. Typically electromagnetic showers will terminate within these tiers with hadronic showers penetrating through. The next three tiers form the Fine Hadronic (FH) calorimeter, which also has uranium plates as absorption layers, but they are 6 mm thick. Hadronic showers will deposit most of their energy in the FH calorimeter although some particles will penetrate further into the final tiers, known as the Coarse Hadronic (CH) calorimeter. There is only one such tier in the CC but there are up to three in the ECs. The absorption layers here are copper or stainless steel 46.5 mm plates.

Most of the cells have a segmentation of 0.1×0.1 in $\eta \times \phi$. The position resolution of a traversing particle is determined by the size of the cells, so the third row in the EM calorimeter, situated at the expected shower maximum for electrons and photons, has a segmentation four times as fine (0.05×0.05). For all layers at $|\eta| > 3.2$ the cell size increases to 0.2×0.2. Figure 3.4 shows a cross section of one quarter of the calorimeter, where the cell segmentation can be seen.

Electrons, photons and jets are all detected and identified by the shape and size of the shower in the calorimeter. Neutrinos do not interact in the calorimeter and are not directly detected. Their presence can be inferred by a measurement of missing transverse energy in an event, E_T^{miss}. The transverse energy, E_T, of a calorimeter object or cell with energy E is defined as

$$E_T = E \sin(\theta). \tag{3.3}$$

Summing E_T for all the cells in the calorimeter provides a measure of E_T^{miss} in an event.

The dominant form of energy loss for muons is through ionisation. Typically a high momentum muon will only lose ~ 2.5 GeV of energy when passing through the calorimeter, since they do not lose much energy to bremsstrahlung radiation. They can be detected in the calorimeter by ionisation of the liquid argon layer but they will not form an electromagnetic shower and so their total energy cannot be measured.

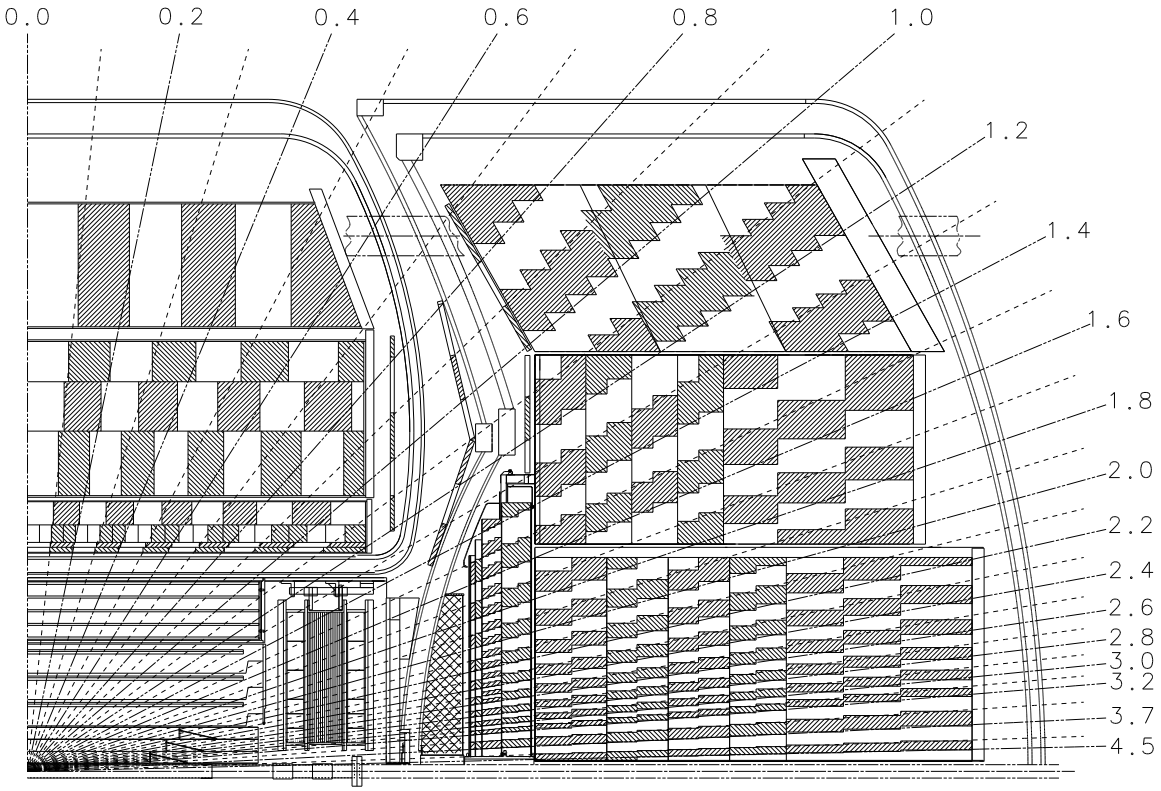

Figure 3.4: *Cross section quarter view of the DØ calorimeter.*

3.4.4 Muon System

Generally, the only detectable particles that will make it all the way through the DØ calorimeter are muons. The muon system surrounds the calorimeter, as can be seen in Figure 3.2. It consists of three sub-systems: Proportional Drift Tubes (PDTs), Mini Drift Tubes (MDTs) and scintillation counters. The PDTs and MDTs are shown schematically in Figure 3.5 and the scintillation counters in Figure 3.6. Drift tube detectors are containers filled with a gas that is ionised by a traversing charged particle. An anode wire runs through the centre of the container and cathode pads lie at its top and bottom. The scintillation counters collect scintillation light when a charged particle passes through them. They are embedded with Wavelength Shifting Fibres which are connected to photomultiplier tubes which convert the light to an electronic signal. The muon system is comprised of three layers, one (the A-layer) inside and two (the B- and C-layers) outside a 1.8 Tesla, solid iron toroid magnet. The bend of particle tracks due to the magnetic field allows a momentum measurement.

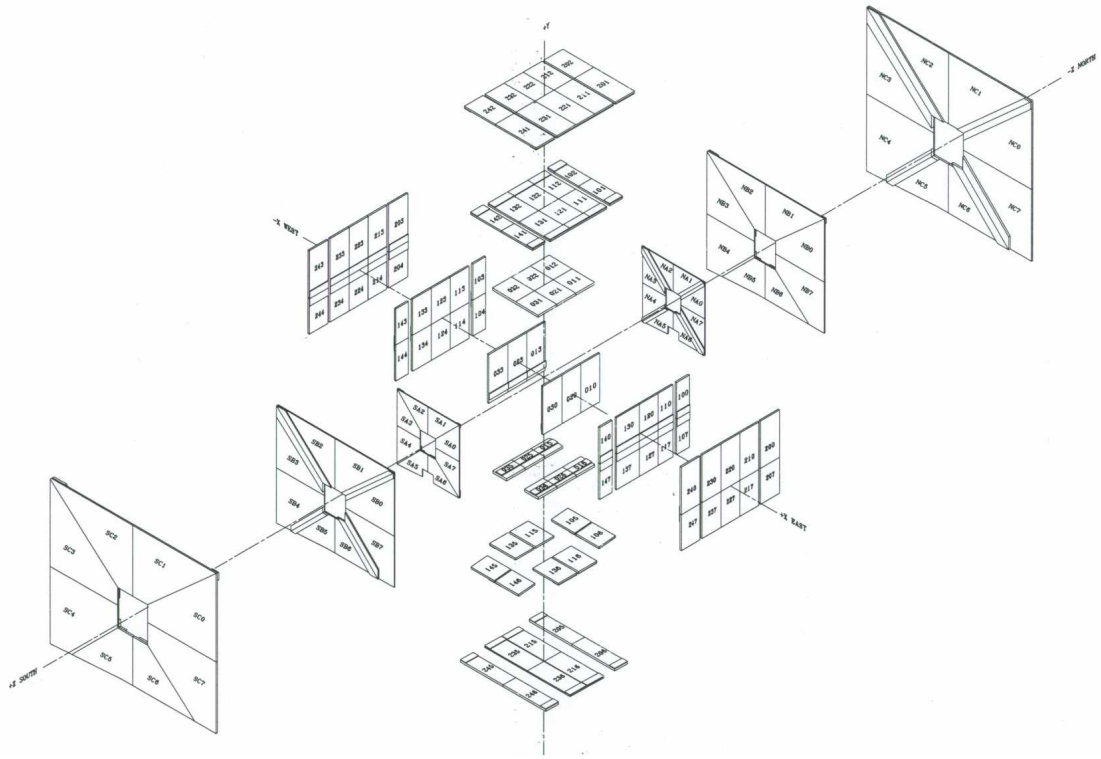

Figure 3.5: *A schematic view of the DØ muon PDT chambers and MDT sections.*

There are two sections to the muon detectors: the central system and the forward system. The value of η measured at the A-layer is denoted η_A. The central system, covering the region $|\eta_A| < 1$, consists of PDT chambers and scintillators in each of the three layers. The PDT chambers are formed from aluminium rectangular extrusion *cells*. There are 94 chambers in total, lying horizontally and vertically around the calorimeter, giving the muon system a cuboid geometry. Each cell is 10.1 cm across and 5.5 cm high and is filled with a gas mixture of 84% argon, 8% CH_4 and 8% CF_4. There are three decks containing typically 24 columns of cells in each B- and C-layer chamber and four decks in each A-layer chamber, except in the bottom region where there are three. Their lengths vary, with a maximum of ~ 6 m. The anode wires lie in the centre of each cell in the direction of the magnetic field lines; the drift time of the ionised gas to the wire gives a position measurement of the distance to the anode in the z direction with a resolution of 0.5 mm. The anodes of neighbouring cells are connected at one end with the readout of both at the other end. The difference in the time of hits in these cells gives a position measurement in the x or y direction with a resolution between 10 and 50 cm, depending on the distance along the wire.

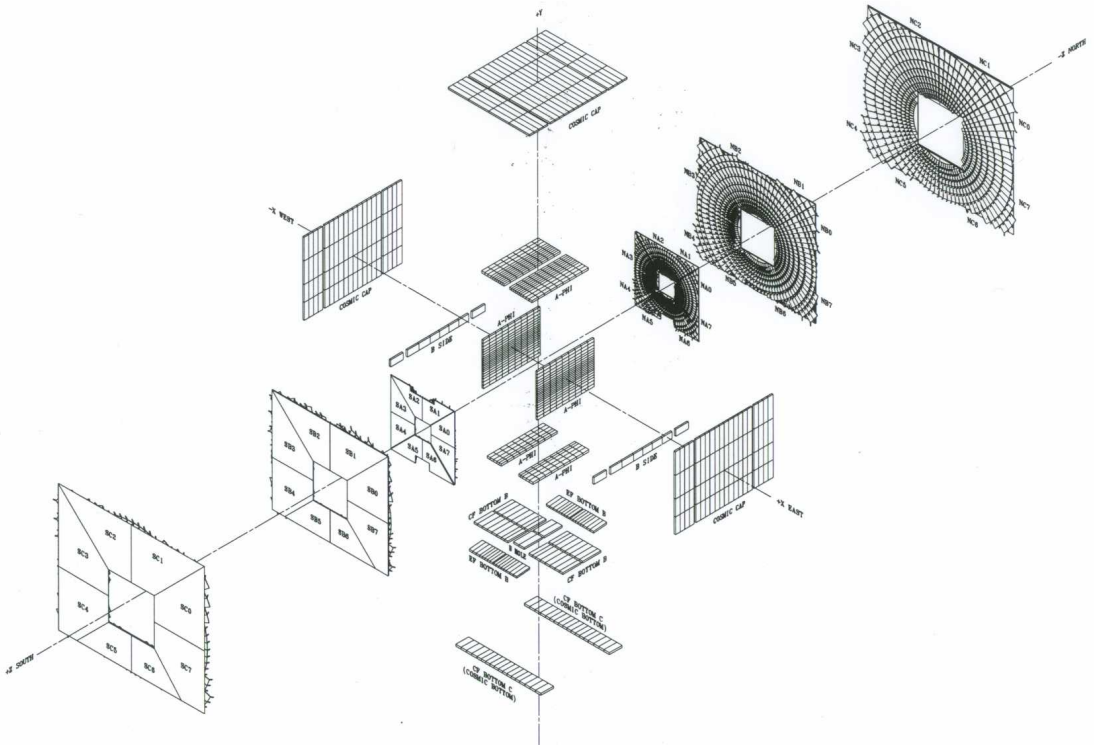

Figure 3.6: *A schematic view of the DØ muon scintillator planes.*

Scintillator counters cover the PDT chambers in the A-layer, the C-layer and the bottom region of the B-layer. The counters in the A-layer, B-layer and the bottom region of the C-layer are segmented in ϕ slices of 4.5° and are 25–56 cm wide (in the z direction). The rest of the C-layer counters are 64 cm wide (in the z direction) and between 207 and 287 cm long (in the x or y direction). The time resolution of the scintillator counters is ~ 2 ns.

The forward system covers the region $1 < |\eta_A| < 2$ and consists of MDT sections and scintillation pixel counters. There are three rectangular layers of MDTs divided into octants. Each cell, containing a gas mixture of 90% CF_4 and 10% CH_4 is 1 cm by 1 cm, with a length in the range 1–6 m, depending on the position within an octant. The length of the cell, and hence the anode wire, runs in the direction of the magnetic field which can either be in the x or y direction depending on which octant it is in. The resolution of the distance from the anode is 0.7 mm, with no measurement made in the direction of the wire. There are four decks of cells in the A-layer and three in the B- and C-layers.

Scintillator counters cover all three layers in the forward region and are segmented

in slices of 0.1×4.5 in $\eta \times \phi$. The timing resolution is ~ 1 ns.

Due to mechanical supports required for the rest of the DØ detector, the region directly below the calorimeter in the muon system is compromised, with only partial coverage achievable, as can be seen in Figures 3.5 and 3.6. This region is $4.25 < \phi < 5.15$ for $|\eta_A| < 1.25$. There are boundaries between the octants in the forward muon system. There are also boundaries in the four corners of the cuboid detector in the central region with some compromised coverage due to gaps midway between each corner. This gives an octant structure similar to that seen in the forward system.

3.4.5 Luminosity Monitor

The purpose of the Luminosity Monitor is to measure the rate of inelastic $p\bar{p}$ interactions. This is achieved by detecting the charged remnants of the proton and the antiproton after the collision. The two detectors are situated between the forward preshower detectors and the beampipe at $z \sim \pm 140$ cm. They each consist of 24 wedges of scintillating material read out by photomultipliers. The Luminosity Monitor covers the range $2.7 < |\eta| < 4.4$.

3.5 The DØ Trigger System

It is important to keep the rate of $p\bar{p}$ collisions at the Tevatron high so that as much integrated luminosity as possible can be collected. The rate of events is therefore too high to be able to write all of them to storage tapes, where they can be analysed offline. It is therefore necessary to decide in real time which events are interesting enough to store. Information from the detector sub-systems is used in a three level trigger system that decreases the rate from 1.8 MHz to 30–60 Hz.

3.5.1 Level 1 Trigger

The Level 1 trigger makes fast decisions on each bunch crossing. At this stage the rate is reduced from 1.8 MHz to 300–1600 Hz. All detector sub-systems, except the SMT, can be used in Level 1 trigger decisions. The decision can be based on standalone trigger objects or combinations between the different sub-detectors.

The Level 1 track trigger has inputs from the CFT and preshower detectors. The scintillating fibres are grouped into 4.5° sections in ϕ. Hits in each section are matched to a group of pre-defined hit maps which represent different curvature paths in the magnetic field corresponding to the following four p_T bins: 1.5–3 GeV, 3–5 GeV, 5–10 GeV and $>$ 10 GeV.

The Level 1 calorimeter trigger adds up the energy in a *tower* of cells in η and ϕ. The transverse energy in each tower can be determined to within four ranges: 3–5 GeV, 5–7 GeV, 7–10 GeV and $>$ 10 GeV.

The Level 1 muon trigger combines wire and scintillator hits to build muon objects. For the data used in this thesis a muon object can be based on a coincidence of scintillator hits in two layers of the muon system (tight scintillator condition) or a coincidence of wire hits with scintillator hits (loose wire and tight scintillator condition).

The *fast-z* inelastic collision trigger is based on a coincidence of hits in the two luminosity detectors, implying an inelastic $p\bar{p}$ collision.

3.5.2 Level 2 Trigger

The Level 2 trigger combines information from all the sub-detectors and provides additional information so as to reduce the rate from 300–1600 Hz to 200–1000 Hz. Information from the SMT is added to Level 1 tracks enabling a better resolution on the p_T measurement as well as a measurement of the track *dca*. The calorimeter trigger consists of three processors designated for finding jets, EM objects and E_T^{miss}. The Level 2 muon trigger combines wire and scintillator hits to form muon objects with track quality and p_T information. *Loose* muon objects require hits inside or outside the toroid; *medium* muon objects require hits inside and outside the toroid.

3.5.3 Level 3 Trigger

The third and final stage of the trigger system further reduces the rate to be written to storage tapes to 30–60 Hz. The Level 3 trigger uses the full precision readout of the detector. It is a computer farm that partially reconstructs events using faster and simpler versions of the offline reconstruction code, described in section 3.6.

3.5.4 Prescales

A series of triggers, containing components from all or some of the three levels, make decisions whenever there is beam in the Tevatron. Due to the high rate of collisions, it is not always possible to write all events that pass these trigger conditions to tape. Certain triggers will run with a *prescale* on their Level 1 condition. When a trigger is running with a prescale the Level 1 trigger only passes the event a certain fraction of the time that the condition is satisfied. For example, if a trigger has a prescale of 10, it will only pass Level 1 in $\frac{1}{10}$th of the events that satisfy the Level 1 condition. The extent to which triggers are prescaled depends on the instantaneous luminosity of the Tevatron.

3.6 DØ Offline Event Reconstruction

The events that are written to storage tapes are later processed by a computer farm which outputs the raw data in a physics oriented format. This event reconstruction takes place in three steps:

1. Hit finding, where the digitised information is converted into hits in certain sub-detectors at definite locations and energies.

2. Track and cluster forming, where hits are combined to form a track in one of the tracking detectors or a cluster of cells in the calorimeter.

3. Formation of physics objects, where tracks and clusters are matched to form jets and particles.

Loose requirements are made on the physics objects to achieve a high efficiency. Tighter selection requirements are made later in offline analyses.

3.6.1 Central Track Reconstruction

Central track objects are formed from hits in the SMT and CFT detectors. A *hypothesis* for a track is initially formed from three SMT hits or three CFT hits. Each hypothesis is extrapolated into the other layers of the SMT and CFT and an expected crossing region is computed. If a hit is found in this region it is added to the hypothesis, otherwise a *miss* is attributed to it. A hypothesis is saved if it passes set criteria

on the number of hits and misses. The saved hypotheses are ordered by an algorithm taking into account the number of hits and misses and the χ^2. A hypothesis is saved as a track if the ratio of the number of hits shared with other tracks to the total number of hits is below a given value.

3.6.2 Vertex and Beamspot Reconstruction

Reconstructed tracks in an event are used to find the positions of the primary vertices: points where the $p\bar{p}$ inelastic collisions occurred. Firstly, all tracks in the event are fit to a common vertex. If the $\frac{\chi^2}{dof}$ of the fit is > 10 the track contributing the most is removed. This process is repeated until the $\frac{\chi^2}{dof} < 10$ or there are less than two tracks used in the fit. The process is repeated from the beginning using all tracks that have not already been associated with a vertex.

The position of the beamspot in each run[4] is found by performing a linear fit to the three-dimensional coordinates for all primary vertices.

3.6.3 Calorimeter Object Reconstruction

Calorimeter objects are reconstructed by forming clusters of neighbouring cells containing energy deposits. The total energy within a cone in $\eta - \phi$ surrounding the cluster is defined and the fraction of cells from EM and hadronic layers is used to identify it as an EM object or a hadronic jet. An EM object is then identified as an electron if it is matched to a central track and a photon if it is not.

The calorimeter is also used to measure the E_T^{miss} in an event. Since muons only lose a small fraction of their energy in the calorimeter, the missing energy must be corrected for any muons identified in the event.

3.6.4 Muon Particle Reconstruction

Muon objects are reconstructed from hits in the muon detectors. For this purpose the muon detectors are divided into two regions: the A-layer and the B- and C-layers combined. Initially hits in these two regions are grouped into *segments*. A segment is formed from a straight line fit to two or more nearby wire hits from the PDTs or MDTs. Any nearby scintillator hits can then be added to the segment. Tracks are

[4]Recorded data is split into *runs* of approximately four hours of data taking.

formed by combining segments in the two regions, allowing a measurement of the muon momentum due to the bend in the magnetic field. These muon chamber tracks and segments are known as *local* muon objects. The quality of a muon object depends on the number of hits in the track or segment. See Appendix A for the definition of *loose* and *medium* muons. The local muon is extrapolated back through the rest of the sub-detectors in an attempt to match it to a reconstructed central track. If this matching is successful then the central and local tracks are combined to form a *global* muon.

It is also possible to reconstruct a muon in the calorimeter by looking for a signal for a charged particle that did not induce showering. If this calorimeter muon fails to match a local muon but is matched to a central track, it is known as a 'calorimeter-only' muon.

Chapter 4

W and Z Physics at the Tevatron

At the Tevatron, W and Z bosons, known collectively as vector bosons, are predominantly produced via the leading order annihilation of a quark antiquark pair: $q\bar{q} \to Z$ and $q\bar{q}' \to W$. Figure 4.1 shows this process for a Z, which will decay to a pair of fermions as discussed below.

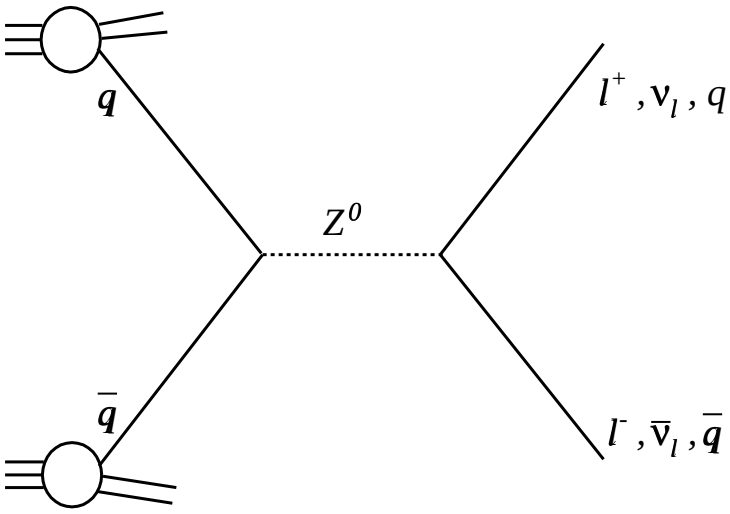

Figure 4.1: Z *production and decay at the Tevatron.*

The cross section for such processes, $p\bar{p} \to V$, where V generically denotes a W or a Z, can be written in the factorised form:

$$\sigma = \sum_{i,j} f_i\left(x_1, \mu_F^2\right) \otimes C_{i,j}^P\left(x_1 x_2 s, \frac{Q^2}{\mu_F^2}\right) \otimes \bar{f}_j\left(x_2, \mu_F^2\right), \tag{4.1}$$

where Q^2 is the scale of the hard process, s is the square of the centre of mass energy of the $p\bar{p}$ system, $C_{i,j}^P\left(x_1 x_2 s, \frac{Q^2}{\mu_F^2}\right)$ are the coefficient functions describing the hard processes, $q_i\bar{q}_j \to V$, and $f_i\left(x_1, \mu_F^2\right)$ and $\bar{f}_j\left(x_2, \mu_F^2\right)$ are the PDFs of the

first principles whereas the PDFs must be taken from fits to experimental data. The partons inside the hadrons that do not participate in the hard interaction will generally interact softly. This part of the process is known as the *underlying event*.

The bosons are unstable and will decay to a pair of fermions; the branching fractions for the decays (taken from [9]) are given in Tables 4.1 and 4.2 for the Z and W respectively. Leptonic decays of the bosons have the cleanest experimental signature

decay channel	branching fraction (%)
e^+e^-	3.363 ± 0.004
$\mu^+\mu^-$	3.366 ± 0.007
$\tau^+\tau^-$	3.370 ± 0.008
invisible	20.00 ± 0.06
hadrons	69.91 ± 0.06

Table 4.1: *Branching fractions for* Z *boson decays. The invisible decays are presumed to be to neutrinos.*

decay channel	branching fraction (%)
$e\nu_e$	10.72 ± 0.16
$\mu\nu_\mu$	10.57 ± 0.22
$\tau\nu_\tau$	10.74 ± 0.27
hadrons	67.96 ± 0.35

Table 4.2: *Branching fractions for* W *boson decays.*

since the huge background from other multijet events at the Tevatron swamps the signal from bosons decaying to quarks. The large V masses, $m_{\rm Z} = 91.1876 \pm 0.0021$ GeV and $m_{\rm W} = 80.425 \pm 0.038$ GeV [9], result in their decay products having high energy. The signature of a $\mathrm{Z} \to \ell^+\ell^-$ event[1] will therefore be two high momentum charged leptons and that of a $\mathrm{W} \to \ell\nu_l$ event will be a high momentum charged lepton as well

[1]In principle, a $\mathrm{Z} \to \ell^+\ell^-$ event is indistinguishable from a $\gamma^* \to \ell^+\ell^-$ event. This means that there also exists quantum mechanical interference terms in the cross section. $\mathrm{Z}/\gamma^* \to \ell^+\ell^-$ denotes the cross section including pure Z and γ^* exchange as well as all Z/γ^* interference terms. Here the $*$ is used to denote that the photon *must* be off mass-shell in order to decay. Although the Z is strictly speaking off mass-shell the distinction is less relevant.

as large $\not\!\!E_T$, due to the presence of the undetected neutrino. Taus will decay before they are detected, making the electron and muon channels the easiest to study.

The invariant mass distribution for a Z or W has a line-shape which is quantified by the *width* of the vector boson. The width is inversely proportional to lifetime, meaning that a short-lived particle has large fluctuations in mass. The Z and W widths are measured as $\Gamma_{\mathrm{Z}} = 2.4952 \pm 0.0023$ GeV and $\Gamma_{\mathrm{W}} = 2.124 \pm 0.041$ GeV respectively [9].

4.1 Electroweak Precision Measurements

W and Z events at the Tevatron can be used to make electroweak precision measurements. One important example, as described in section 2.3, is m_{W}.

Since a leptonically decaying W has an invisible decay product, a neutrino, its kinematic properties cannot be fully reconstructed from those of its decay products. The mass is therefore deduced from the distribution of the charged lepton p_T or the W transverse mass, $m_{\mathrm{W}}^{\mathrm{T}}$. Assuming massless decay products, the transverse mass is defined as:

$$m_{\mathrm{T}}^2 = 2|{p_T}^i||{p_T}^j|(1 - \cos\Delta\phi_{ij}), \tag{4.2}$$

where ${p_T}^i$ and ${p_T}^j$ are the p_T of the two decay products and $\Delta\phi_{ij}$ is the angle between them.

Another important precision measurement is Γ_{W}, which places constraints on exotic W decays. Γ_{W} can be indirectly measured from R_ℓ, the ratio of the cross section for $\mathrm{p\bar{p}} \to \mathrm{W} + \mathrm{X} \to \ell\nu + \mathrm{X}$ to that for $\mathrm{p\bar{p}} \to \mathrm{Z} + \mathrm{X} \to \ell^+\ell^- + \mathrm{X}$. R_ℓ can be expressed as:

$$R_\ell = R\frac{Br(\mathrm{W} \to \ell\nu)}{Br(\mathrm{Z} \to \ell^+\ell^-)}, \tag{4.3}$$

where R is the ratio between the W and Z production cross sections and $Br(\mathrm{W} \to \ell\nu)$ and $Br(\mathrm{Z} \to \ell^+\ell^-)$ are the leptonic branching fractions of the W and Z respectively. $Br(\mathrm{W} \to \ell\nu)$ can be extracted from the above expression since R is accurately predicted by a SM calculation [10] that used a Next-to-Next-to Leading Order (NNLO) QCD expression [11, 12] and $Br(\mathrm{Z} \to \ell^+\ell^-)$ has been accurately measured at LEP [9]. The W leptonic branching ratio can be expressed as:

$$Br(\mathrm{W} \to \ell\nu) = \frac{\Gamma(\mathrm{W} \to \ell\nu)}{\Gamma_{\mathrm{W}}}, \tag{4.4}$$

within the SM [9]. Thus Γ_{W} can be extracted. It is also possible to make a direct measurement of Γ_{W} from the shape of the distribution of $m_{\mathrm{W}}^{\mathrm{T}}$.

Although similar precision measurements of the Z are also interesting, they have already been measured at LEP to a much higher precision than could be expected from hadron colliders. There is one exception to this rule, the forward-backward asymmetry, A_{FB}, of the lepton pairs in the process $\mathrm{q\bar{q}} \to \mathrm{Z}/\gamma^* \to \ell^+\ell^-$. A non-zero A_{FB} arises from the presence of both vector and axial vector couplings of electroweak bosons to fermions. The Z-quark couplings can be extracted from the distribution of A_{FB} as a function of the invariant mass of the lepton pair, $M_{\ell^+\ell^-}$. The high mass range attainable at the Tevatron allows a constraint of non SM processes contributing to $\mathrm{q\bar{q}} \to \ell^+\ell^-$ that is complementary to direct searches using the total cross section as a function of $M_{\ell^+\ell^-}$.

4.2 W and Z Events as Probes of QCD

Properties of the vector bosons can be determined by measuring the kinematic variables of their decay products. The clean experimental signature and well understood electroweak nature of W and Z events makes them ideal probes of the QCD aspects of their production. Measurements of the Z rapidity distribution and the W charge asymmetry, arising in part from the difference between the u and d quark PDFs, provide a strong constraint on the (anti)proton PDFs.

In a naive model it may be expected that the vector boson is produced with zero p_T since the (anti)proton's momentum is directed down the beam pipe. In reality, however, the (anti)quark may emit gluons before the collision, resulting in a non-zero p_T. Measurements of the vector boson p_T distributions provide a good test of QCD phenomenology. If a hard enough parton is emitted the event will contain a well distinguished jet in addition to the final state leptons.

As well as being interesting in their own right, constraints of both the PDFs and the p_T distributions are important in reducing the systematic uncertainty on electroweak precision measurements such as m_{W}.

4.5 W and Z Events as 'Standard Candles'

W and Z events serve as 'standard candles' for other high p_T leptonic events. They can be used to calibrate the detectors and to understand lepton reconstruction and trigger efficiencies, as is described for $Z/\gamma^* \to \mu^+\mu^-$ events in sections 6.3–6.5. $Z \to \ell^+\ell^-$ events are used to calibrate momentum scales and understand the alignment of the detectors, since the Z line shape is well known from LEP. Many searches for BSM scenarios involve the decay of massive particles to leptons which will have signatures similar to those of W and Z events.

The luminosity uncertainty on normalised measurements at the Tevatron currently stands at $\sim 6\%$ (see section 6.1 for a description of the method used). Both experimental and theoretical uncertainties on the W and Z cross sections are predicted to be at the 1–2% level, meaning that ultimately a smaller uncertainty on the overall luminosity may well be achievable using W and Z cross sections.

Chapter 5

Event Simulation Using Monte Carlo Event Generators

Monte Carlo methods are used for solving problems by utilising sequences of random numbers. The aim of a Monte Carlo simulator is to reproduce the behaviour of a system described by probability distribution functions.

In particle physics Monte Carlo programs are used as event generators that simulate interactions, such as those occurring in particle accelerators. They output a set of initial, intermediate and final state particles and their associated 4-momenta. The generated events can be passed through simulations of detector responses to the produced particles so that the output can be compared to data. Resolution and detector acceptance effects are taken into consideration in the simulation. Alternatively data can be corrected for detector effects so that a direct comparison to generator level Monte Carlo simulations can be made.

Event generators are invaluable for analysing experimental data. They give physicists an idea of the rate that certain processes are predicted to occur to. They are used to give detector acceptances, necessary to extract the true physics signal from that seen in detectors. Selection criteria can be optimised by studying the signal to background ratio for certain processes.

5.1 HERWIG and PYTHIA

HERWIG (Hadron Emission Reactions With Interfering Gluons) [13] and PYTHIA [14] are both general purpose Monte Carlo programs that simulate all hard lepton-lepton,

lepton-hadron and hadron-hadron processes as well as soft hadron-hadron processes, with particular emphasis on QCD aspects.

The simulation of an event is factorised into three regions separated by the energy scale at which they occur:

1. the *elementary hard subprocess*,

2. *initial- and final-state parton showers* and

3. *hadronisation* of final state partons or incoming PDFs and underlying event.

The elementary hard subprocess is calculated exactly to Leading Order (LO) in perturbation theory. A pair of incoming particles interact to produce fundamental outgoing particles. In collisions involving hadrons the incoming particles will be the constituent partons. For Z production at the Tevatron decaying to an electron and a positron the hard subprocess will be $q\bar{q} \rightarrow Z \rightarrow e^+e^-$. The hard energy scale, Q, is set by the mass of the Z. In this example, the LO cross section is purely an electroweak process, so the normalisation will not depend on α_S.

The parton showers provide QCD corrections to the LO calculation. Initial- and final-state showers represent parton emission from any incoming and outgoing partons respectively. Figure 5.1 shows a schematic view of a parton shower, which describes the radiation of partons from partons which in turn radiate more partons and so on. The parton showers essentially resum the calculation to the LLA which takes into account logarithmic enhancements in the cross section in both the collinear and soft limits of QCD radiation.

Parton showers utilise the fact that in the collinear limit the matrix element for a process containing $n+1$ partons factorises into the product of the matrix element for n partons and the lowest order Altarelli-Parisi splitting function, $P_{ab}(z)$, which represents the probability for a parton of type a to emit a parton of type b with a fraction z of its longitudinal momentum [15]. If a shower is evolved using this prescription, with an evolution variable proportional to the angle of emissions in the small angle limit decreasing as the shower progresses, large logarithmic terms in the collinear limit will be accounted for.

Logarithmic enhancements also occur in the limit of soft gluon emission. The cross section in this region is dominated by interference between Feynman diagrams,

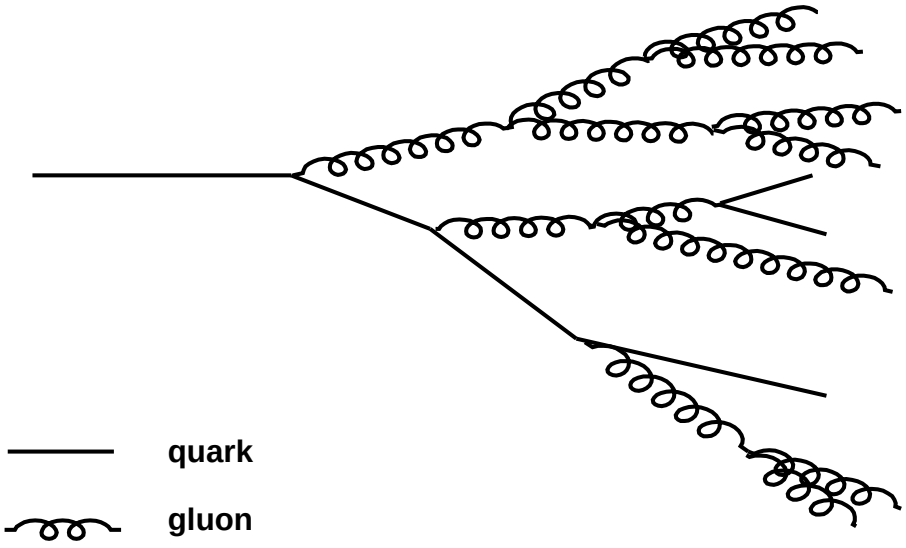

Figure 5.1: *A schematic diagram of a parton shower.*

which is destructive in large angle regions. Soft gluon enhancements are taken into account by restricting the available phase space to an angular ordered region.

For final-state showers the evolution variable decreases from the hard scattering down to the hadronisation scale. Initial-state showers are evolved backwards so that the variable decreases from the hard scattering to the incoming hadrons.

For branching $a \to bc$, PYTHIA uses the virtuality of the branching parton, m_a^2, for the evolution variable. An additional veto on opening angles to ensure angular ordering is applied.

For final-state showers HERWIG uses an angular evolution variable, $\zeta_{bc} = \frac{p_b.p_c}{E_b E_c}$, where p_i and E_i are the 4-momenta and energy of parton i respectively. To evolve initial-state showers it uses $E_a^2 \zeta_{bH}$, where p_H and E_H are the 4-momenta and energy of the incoming *hadron*. The HERWIG evolution variables ensure that angular ordering, and hence soft gluon enhancements are properly treated.

The parton shower continues from the scale Q down to a cut off scale, Q_0, where it terminates. In this region the perturbative physics of the parton shower is no longer applicable since the strong coupling constant is too large. Colour confinement requires that the partons at the end of the shower must be combined into hadrons. This is achieved via a non-perturbative process known as hadronisation.

PYTHIA uses the *string* model to describe this process. When a colour connected quark antiquark pair move apart from each other, the colour field between them collapses onto a string-like configuration. The energy density per unit length is constant so that as they move further apart the potential energy stored in the string increases until it becomes energetically favourable to pull another quark antiquark pair out of the vacuum, splitting the string in two. This break-up process continues until only on mass-shell hadrons remain.

HERWIG uses the *cluster* model to describe hadronisation. All remaining gluons at the end of the parton shower are forcibly split into quark-antiquark pairs which are grouped into colour-neutral clusters. The clusters decay into hadrons.

The parton showers are only reliable approximations in the soft and collinear limits. Emission is completely suppressed in the *dead zones* corresponding to hard and large angle parton radiation. The matrix element of the hard subprocess is therefore corrected to include the emission of one hard parton, and a matching between the parton showers and the matrix element corrections is required.

In addition to the QCD parton showers, PYTHIA also includes QED showers, where photons are emitted from charged particles. HERWIG only contains such a model for final state quarks and not for initial state quarks or any leptons.

Both PYTHIA and HERWIG have variable parameters that can be determined by tuning distributions to fit as closely as possible to experimental data. They can be split into three categories:

1. perturbative parameters,

2. interface (between perturbative and non-perturbative) parameters,

3. non-perturbative parameters.

The perturbative parameters control aspects of the hard subprocess and the parton showers. An example is Λ_{QCD}, the scale at which α_S becomes large and non-perturbative QCD becomes important. The interface parameters control the emission cut offs in the parton showers that set the scale below which perturbative QCD is unreliable. Non-perturbative parameters are used in the models that describe hadronisation and the non-perturbative p_T of incoming hadrons.

5.2 MC@NLO

MC@NLO [16] is a Monte Carlo event generator that calculates the hard sub-process to an additional order in α_S with respect to standard Monte Carlo generators. The events generated by MC@NLO are then showered and hadronised by one of the standard Monte Carlo programs. There is no need to make matrix element corrections since the emission of an extra gluon is already taken into account. Presently MC@NLO has only been interfaced with HERWIG.

5.3 Event Simulation at DØ

PYTHIA is used for the simulation of DØ events in this thesis. After particles have been generated, it is necessary to model the effects of the magnetic fields and material of the detector. At DØ this is done in two ways:

(a) D0gstar simulation

A simulation package called D0gstar [17] utilises the CERN package GEANT [18]. Features of GEANT are used to simulate the behaviour of the detector. Ionisation and showering are produced where appropriate. The expected response of DØ to particles is modelled, with the output being digitised data, as is produced by a real particle. The full event reconstruction used on the real data can then be used on the simulated data so that direct comparisons can be made. The D0gstar Monte Carlo Simulation will be referred to as DMCS in future chapters.

(b) Parameterised simulation

A fast, parameterised simulation is also available. Rather than simulating the exact detector response and fully reconstructing events, particles and physics objects (such as muons, jets and missing energy) are simply smeared to match the resolution seen in data. Reconstruction efficiencies are measured in data and introduced into the Monte Carlo simulation. The Parameterised Monte Carlo Simulation will be referred to as PMCS in future chapters.

Chapter 6

Measurement of the Inclusive $Z/\gamma^* \to \mu^+\mu^-$ Cross Section

This chapter describes a measurement of $\sigma\,(Z/\gamma^*)$, the cross section for $p\bar{p} \to Z/\gamma^* + X \to \mu^+\mu^- + X$ with the di-muon invariant mass, $M_{\mu\mu} > 40$ GeV. In addition, a measurement of $\sigma\,(Z)$, the cross section for $p\bar{p} \to Z + X \to \mu^+\mu^- + X$, is obtained by correcting the cross section for pure γ^* and Z/γ^* interference terms so that only the pure Z propagator is considered.

$\sigma\,(Z/\gamma^*)$ is evaluated according to the following formula:

$$\sigma\,(Z/\gamma^*) = \frac{N_{\rm cand}(1 - f_{\rm bckgrd})}{\varepsilon_{Z\gamma*} \int \mathcal{L}dt}, \tag{6.1}$$

where $N_{\rm cand}$ is the number of candidate $Z/\gamma^* \to \mu^+\mu^-$ events, $f_{\rm bckgrd}$ is the fraction of background events, $\varepsilon_{Z\gamma*}$ is the efficiency to select candidate events and $\int \mathcal{L}dt$ is the integrated luminosity for the sample. The detector acceptance, muon reconstruction, trigger and selection cut efficiencies are all included in $\varepsilon_{Z\gamma*}$, which is evaluated using $Z/\gamma^* \to \mu^+\mu^-$ PMCS. The efficiencies are measured using data and since they are in general not constant throughout the detector, they are input into PMCS as a function of relevant detector coordinates. It is important to chose the correct coordinates so as to avoid any biases in the efficiencies due to the geometrical distributions of the samples used to measure the efficiencies. Section 6.6.2 summaries the coordinates chosen for the different efficiencies. Section 6.8 addresses the possible biases and justifies the chosen coordinates for the tracking and loose muon reconstruction efficiencies.

Section 6.1 describes the measurement of $\int \mathcal{L}dt$, section 6.2 describes the measurement of $N_{\rm cand}$, $f_{\rm bckgrd}$ and parts of $\varepsilon_{Z\gamma*}$ and sections 6.3–6.6 describe the rest of

the measurement of $\varepsilon_{Z\gamma*}$.

6.1 Measurement of Integrated Luminosity

This section gives a very brief description of the method used to measure luminosity at DØ, for details see [19]. The integrated luminosity for a data sample is given by the following formula:

$$\int \mathcal{L}dt = \frac{N_{\mathrm{p\bar{p}}}}{\varepsilon_{\mathrm{LM}}\,\sigma_{\mathrm{p\bar{p}}}}, \tag{6.2}$$

where $N_{\mathrm{p\bar{p}}}$ is the number of inelastic $\mathrm{p\bar{p}}$ interactions, $\sigma_{\mathrm{p\bar{p}}}$ is the total inelastic $\mathrm{p\bar{p}}$ cross section and $\varepsilon_{\mathrm{LM}}$ is the efficiency of the Luminosity Monitor, which includes the geometric acceptance as well as the efficiency to detect charged particles within the acceptance. The Luminosity Monitor, as described in section 3.4.5, measures $N_{\mathrm{p\bar{p}}}$. $\varepsilon_{\mathrm{LM}}$ is measured using a combination of Monte Carlo simulations and DØ data (see [19] for details). The value of $\sigma_{\mathrm{p\bar{p}}}$ is measured at the CDF [20] and E811 [21] experiments at $\sqrt{s} = 1.8$ TeV. The two results are combined to give a value which is extrapolated to $\sqrt{s} = 1.96$ TeV to a value of 60.7 ± 2.4 mb [22]. The uncertainty on the luminosity is 6.5%.

A total integrated luminosity of 147.7 ± 9.6 pb^{-1} is used in this analysis [23].

6.2 $Z/\gamma^* \rightarrow \mu^+\mu^-$ Selection Criteria and Backgrounds

6.2.1 Event Selection Cuts

The event selection requires evidence that a pair of oppositely charged, high p_T, muons is produced. The muons are identified by requiring a track in the central detectors that is matched to a track of at least *loose* quality in the muon detectors (see Appendix A for the definition of loose muons). In order to ensure reasonable trigger and reconstruction efficiencies, the muons are required to lie within a nominal geometrical acceptance of the muon detectors. This excludes the region where $|x_A| < 110$ cm and $|y_A| < 110$ cm as well as the compromised region at the bottom of the detectors, $4.25 < \phi_A < 5.15$ for $|\eta_A| < 1.25$, where x_A, y_A, η_A and ϕ_A are the x, y, η and ϕ coordinates of a track at the muon A-layer, found by extrapolating the

central track out to the A-layer. Figure 6.1 shows a two-dimensional scatter plot of ϕ_A versus η_A for candidate muons after all but the geometric acceptance selection criteria (see below) have been applied.

Any event containing a pair of high p_T muons is a potential background to the $Z/\gamma^* \rightarrow \mu^+\mu^-$ events. One possible source is $b\bar{b}$ events in which muons are produced in the b decays. In order to reduce this background, requirements are made on the isolation of the muons from other particles, since the muons from $b\bar{b}$ events will be buried inside jets.

Another source of background is from cosmic ray muons. If a cosmic ray muon traverses the detector it can produce two muon tracks, one from travelling towards and one from travelling away from the centre of the detector. Since the incoming track is travelling in the opposite direction to a track from a collision event, the two muon tracks will usually be assigned opposite charges. In order to reduce this background, cuts are made on the angle between the two muon tracks, which for a cosmic ray muon will be exactly back-to-back, and on the *dca* of the tracks.

Additional sources of background come from $Z/\gamma^* \rightarrow \tau^+\tau^-$ events, $W \rightarrow \mu\nu$ events containing an additional muon inside a jet and di-boson (WW, WZ and ZZ) events.

The p_T of candidate muons is measured from the track in the central detectors. For tracks that only have hits in the CFT and not the SMT the following correction is made to $\frac{q}{p_T}$, where q is the track charge:

$$\left(\frac{q}{p_T}\right)' = \frac{q}{p_T} - \left(\frac{\sigma_{dca,\frac{q}{p_T}}}{\sigma_{dca,dca}}\, dca\right), \tag{6.3}$$

where $\sigma_{dca,\frac{q}{p_T}}$ and $\sigma_{dca,dca}$ are elements of the track fit error matrix. A derivation of equation 6.3 is given in Appendix B. Having required two central detector tracks matched to at least loose quality muons within the geometrical acceptance of the muon system, additional cuts are applied. Figures 6.2–6.9 show the following histograms, where appropriate, for each cut:

- Distribution of the cut variable after all other cuts have been applied.
- Distribution of $M_{\mu\mu}$ for the events that fail only that cut.

The idea behind these plots is to allow the reader to assess:

- The degree to which each cut quantity discriminates signal from background.

- The amounts of signal and background exclusively rejected by each cut.
- The level of background remaining in the selected event sample.

The additional selection criteria are:

1. $p_T > 15$ GeV for both muons [Figure 6.2].

2. $M_{\mu\mu} > 40$ GeV [Figure 6.3].

3. At least two out of the following four isolation cuts are required to pass:

   (a) $\sum_{R=0}^{0.5} p_T^{\text{tracks}} < 3.5$ GeV, where $\sum_{R=0}^{0.5} p_T^{\text{tracks}}$ is the sum of the p_T of tracks contained within a cone around the first muon track direction with opening angle $R < 0.5$, where $R^2 = (\Delta\eta)^2 + (\Delta\phi)^2$. The tracks are also required to be < 2 cm in z from the muon track.

   (b) Same as (a) but for the second muon.

   (c) $\sum_{R=0.1}^{0.4} E_T^{\text{cells}} < 2.5$ GeV, where $\sum_{R=0.1}^{0.4} E_T^{\text{cells}}$ is the sum of the transverse energies of calorimeter cells for $0.1 < R < 0.4$ around the direction of the first muon. Cells in the electromagnetic and fine hadronic calorimeters are used, but not those in the coarse hadronic calorimeter.

   (d) Same as (c) but for the second muon.

   [Figure 6.4].

4. The muons are required to be oppositely charged [Figure 6.5].

5. For muon tracks containing SMT hits $dca < 0.02$ cm and for muon tracks with no SMT hits $dca < 0.2$ cm [Figure 6.6].

6. The pseudo-acolinearity, $\Delta\alpha_{\mu\mu}$, between the two muons is required to be > 0.05, where $\Delta\alpha_{\mu\mu} = |\Delta\phi_{\mu\mu} + \Delta\theta_{\mu\mu} - 2\pi|$ and $\Delta\phi_{\mu\mu}$ and $\Delta\theta_{\mu\mu}$ are the differences in the muon ϕ and θ measurements. [Figure 6.7].

   Figure 6.8 shows $M_{\mu\mu}$ for events rejected by the dca and $\Delta\alpha_{\mu\mu}$ cuts.

7. Before March 2003 the single muon trigger, MUW_W_L2M3_TRK10, was heavily prescaled at high luminosities. In this period candidate events are required to have been accepted by one of the di-muon triggers 2MU_A_L2M0, 2MU_A_L2M0_TRK(5,10), 2MU_A_L2M0_L3L(6,15) or 2MU_A_L2ETAPHI.

For the rest of the dataset candidate events are required to have been accepted by one of the above di-muon triggers or MUW_W_L2M3_TRK10. The dataset is therefore split into two periods. Period 1 is before March 2003 and corresponds to $\int \mathcal{L}dt = 36.8$ pb^{-1}. Period 2 is from March 2003 and corresponds to $\int \mathcal{L}dt = 110.9$ pb^{-1} [Figure 6.9]. More information about these triggers is given in Appendix C.

The number of candidate events after these selection criteria is 14352.

6.2.2 $M_{\mu\mu}$ Resolution

Figure 6.3 shows a large continuum at low $M_{\mu\mu}$. In order to investigate the extent to which this region is populated with $Z/\gamma^* \rightarrow \mu^+\mu^-$ events with mis-measured muon p_T, Figure 6.10(a) shows the $M_{\mu\mu}$ distribution for the selected candidate events in which:

- both of the central muon tracks have at least four SMT hits and at least 14 CFT hits and
- one of the central muon tracks has less than four SMT hits or less than 14 CFT hits .

The two plots are normalised to the same number of events. In the events with two high quality tracks the peak region becomes narrower. However, the approximately flat distribution at low masses is similar in the two plots, thus demonstrating that these events arise primarily from continuum Drell-Yan production rather than tracks with mis-measured momentum. This plot helps to demonstrate that the efficiency of the $M_{\mu\mu} > 40$ GeV requirement in the event selection cuts is insensitive to the details of track quality requirements and momentum resolution.

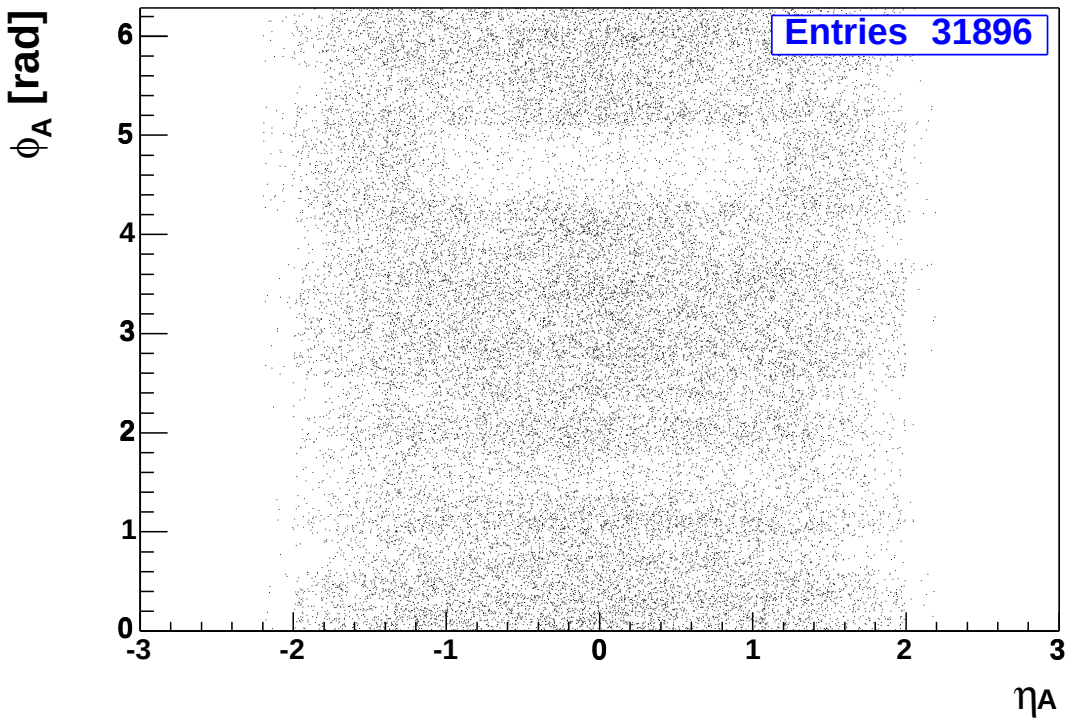

Figure 6.1: *ϕ_A versus η_A of muons in candidate events before cuts on geometrical acceptance are applied.*

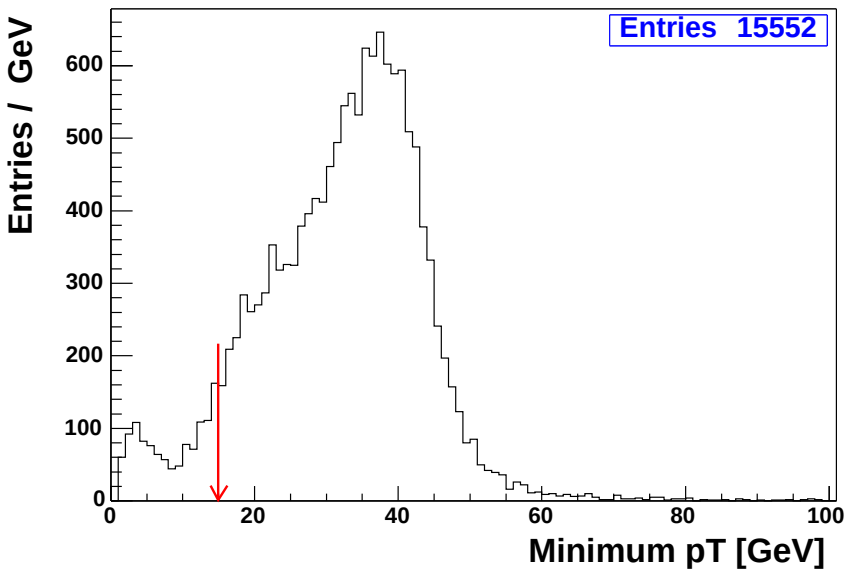

(a)

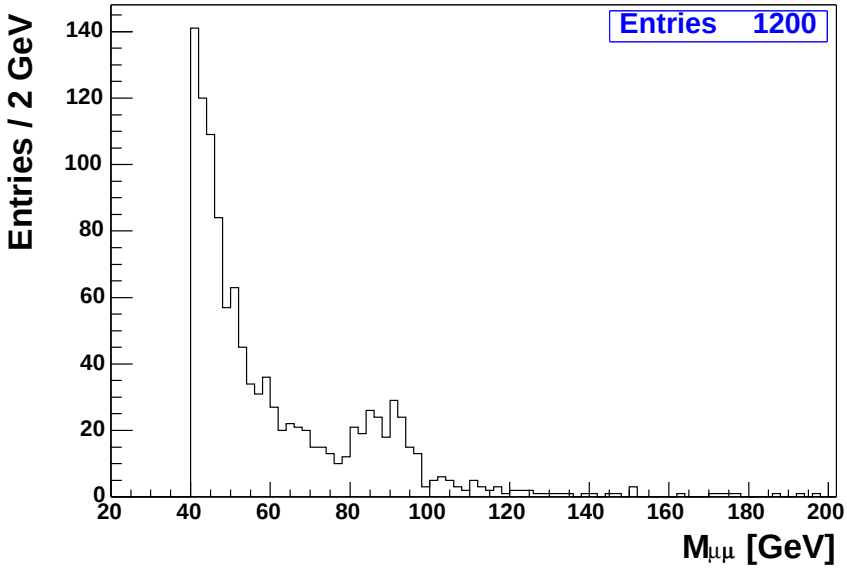

(b)

Figure 6.2: *(a) p_T distribution for the lowest p_T muon in the event after all other cuts have been applied. The red arrow indicates the position of the cut. (b) Distribution of $M_{\mu\mu}$ for the events exclusively rejected by this cut.*

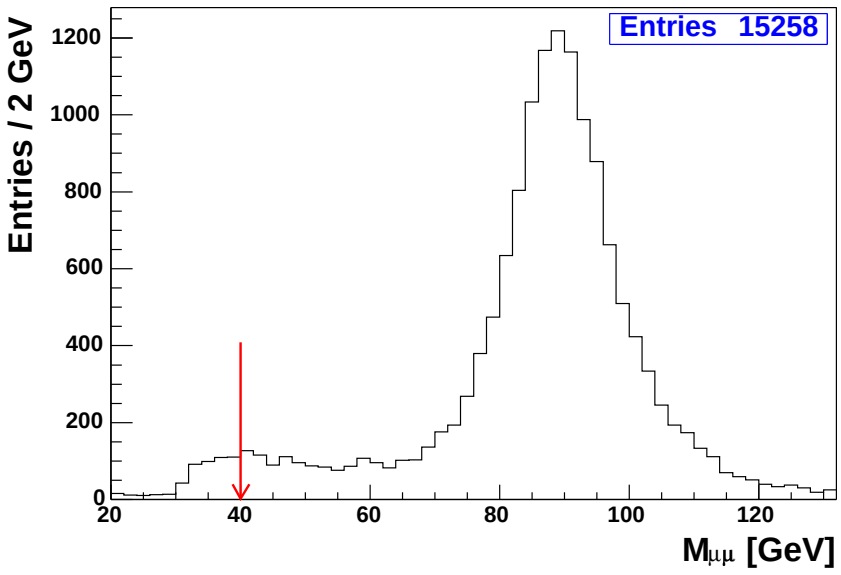

Figure 6.3: *Distribution of $M_{\mu\mu}$ before the cut on $M_{\mu\mu}$ is applied. The red arrow indicates the position of the cut.*

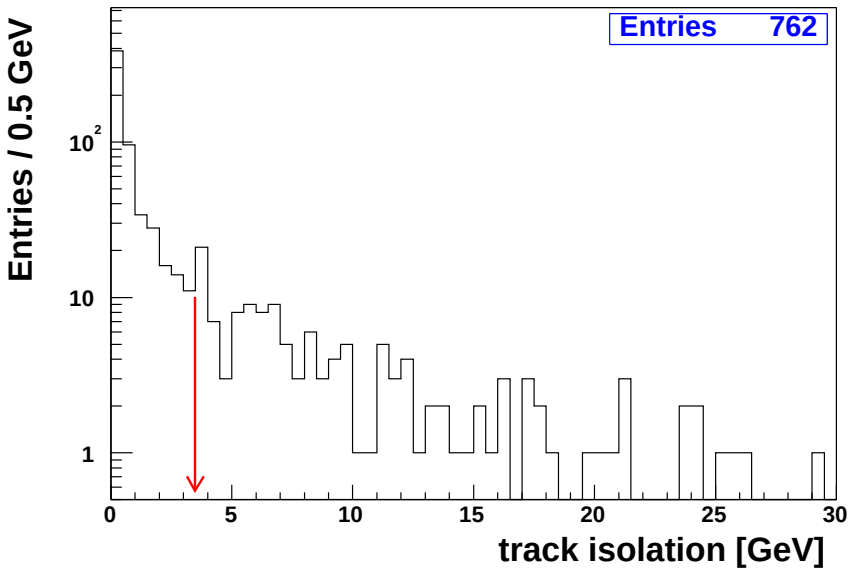

(a)

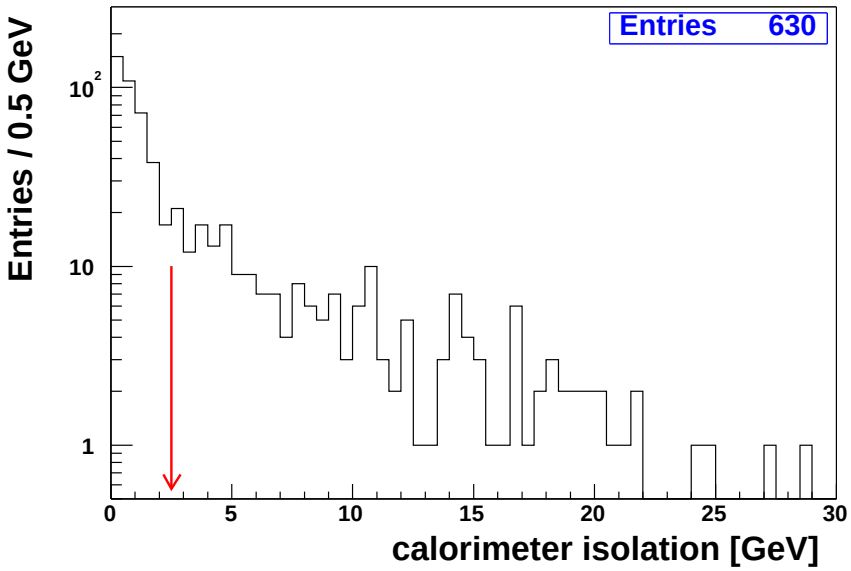

(b)

Figure 6.4: *Distribution of (a)* $\sum_{R=0}^{0.5} p_T^{\text{tracks}}$ *and (b)* $\sum_{R=0.1}^{0.4} E_T^{\text{cells}}$ *for each muon if one and only one of the other three isolation cuts pass. The red arrows indicate the positions of the cuts.*

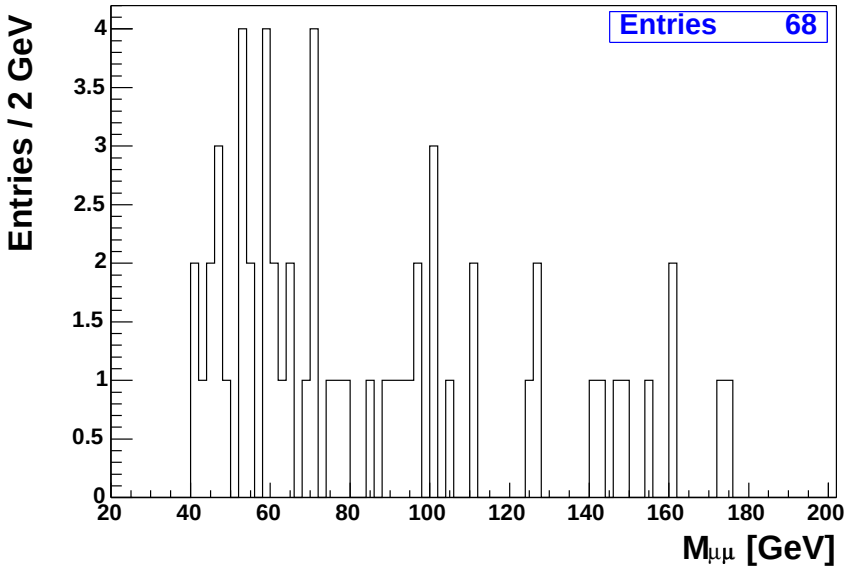

Figure 6.5: *Distribution of $M_{\mu\mu}$ for the events exclusively rejected by the requirement that the two muons be oppositely charged.*

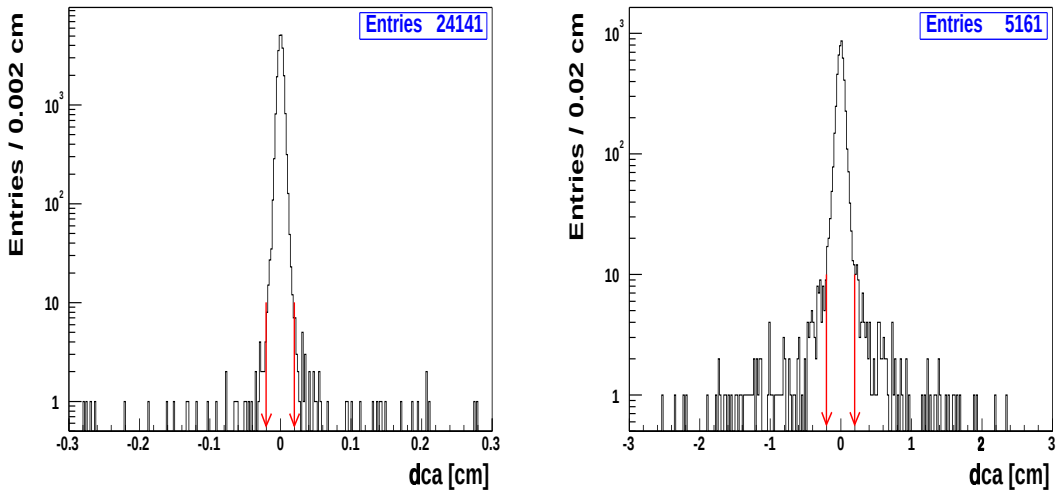

(a) (b)

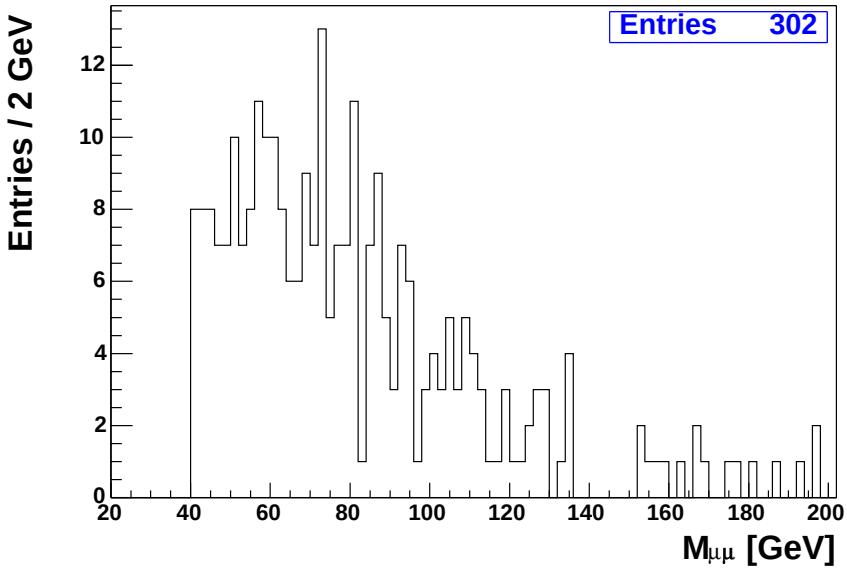

(c)

Figure 6.6: *(a) Distribution of dca after all other cuts have been applied for (a) tracks with SMT hits and (b) tracks without SMT hits. The red arrows indicate the positions of the cuts. (c) Distribution of $M_{\mu\mu}$ for the events exclusively rejected by this cut.*

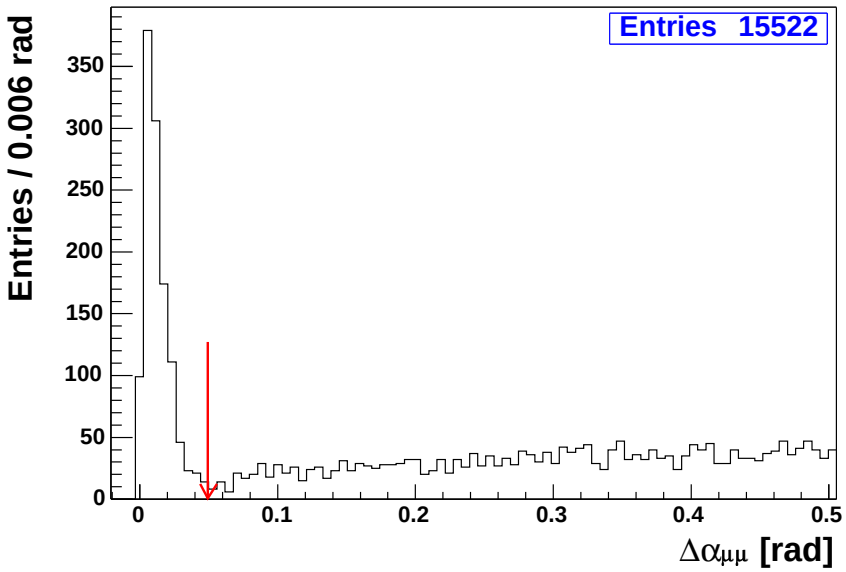

(a)

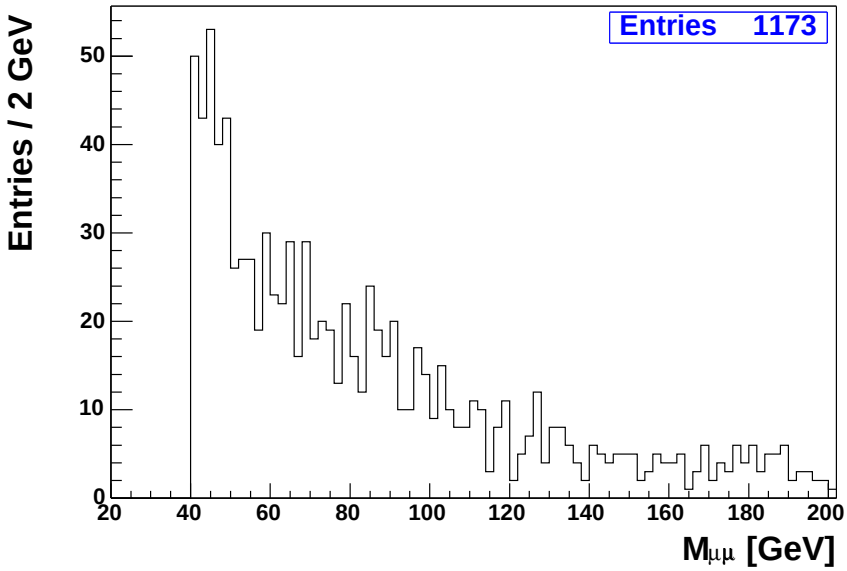

(b)

Figure 6.7: *(a) Distribution of $\Delta\alpha_{\mu\mu}$ after all other cuts have been applied. The red arrow indicates the position of the cut. (b) Distribution of $M_{\mu\mu}$ for the events exclusively rejected by this cut.*

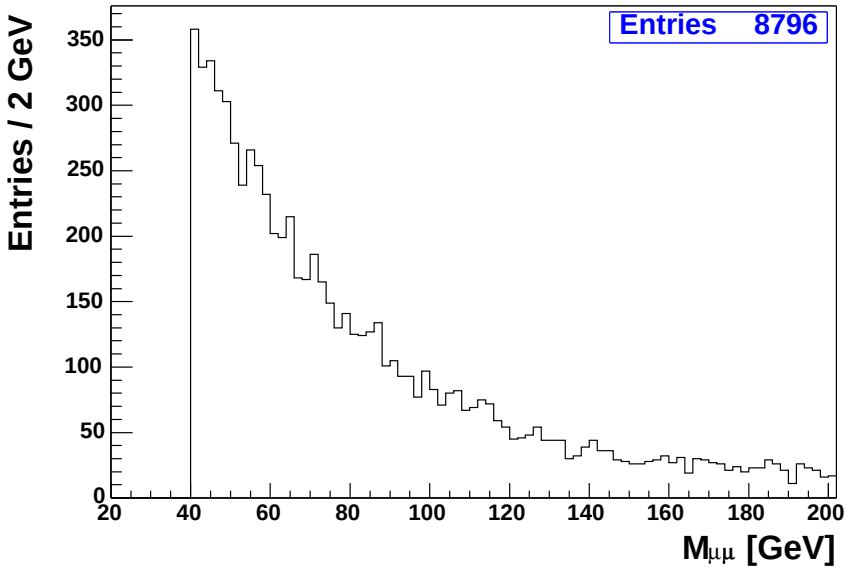

Figure 6.8: *Distribution of $M_{\mu\mu}$ for the events rejected by the cosmic cuts (dca or $\Delta\alpha_{\mu\mu}$).*

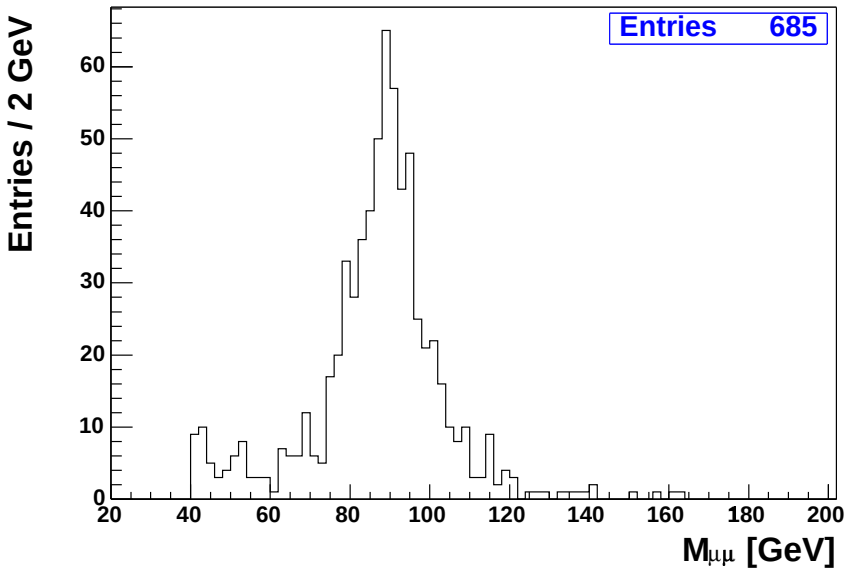

(a)

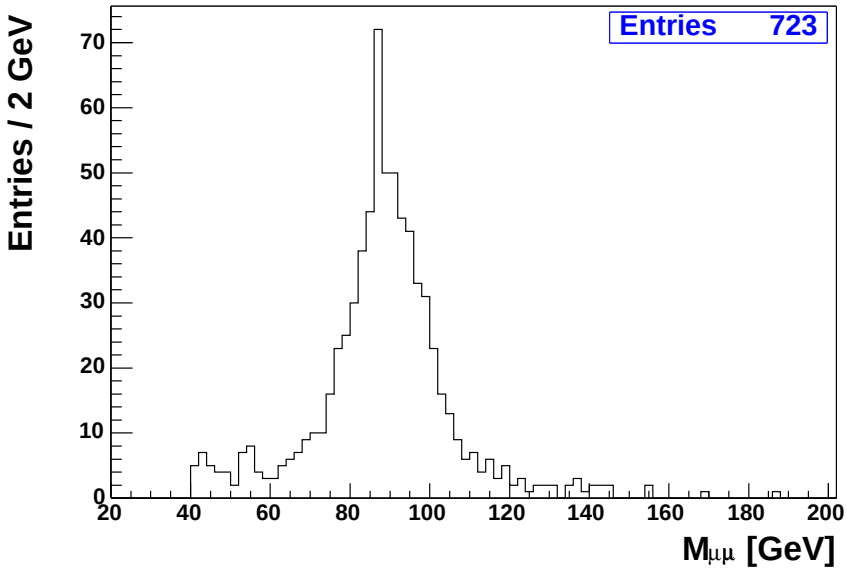

(b)

Figure 6.9: *Distribution of $M_{\mu\mu}$ for the events exclusively rejected by the requirement that candidate events were selected by one of the triggers given in the text for (a) period 1 and (b) period 2.*

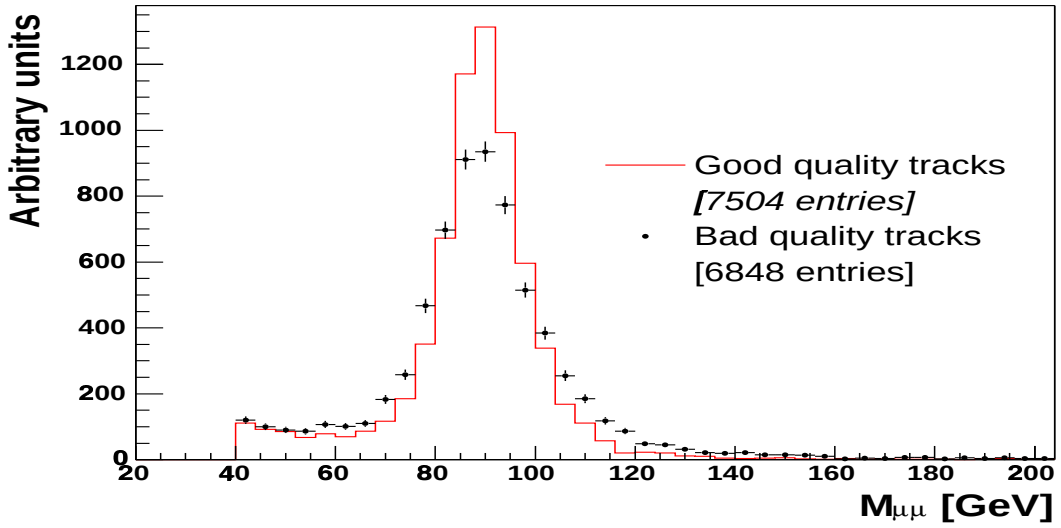

(a)

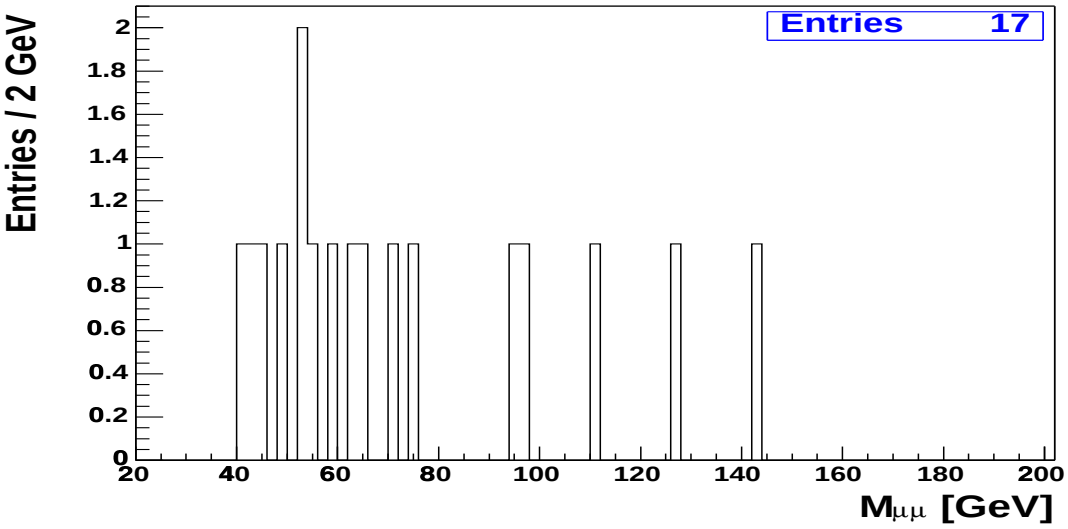

(b)

Figure 6.10: *Distribution of $M_{\mu\mu}$ for: (a) Candidate events in which both of the muon tracks have at least four SMT hits and 14 CFT hits (red histogram) and in which at least one of the muon tracks has fewer than four SMT hits or 14 CFT hits (points with error bars). The two histograms are normalised to the same number of events. (b) Like sign di-muon events passing all other cuts in which both of the muon tracks in the central detector have at least four SMT hits and 14 CFT hits.*

6.2.3 $b\bar{b}$ Background

The muons from $b\bar{b}$ events are buried inside jets and so should appear non-isolated from other particles. Although most of the muons from candidate $Z/\gamma^* \rightarrow \mu^+\mu^-$ events will be isolated from other particles, the presence of jets may cause one or both of the muons to be non-isolated. In addition, muon final state bremsstrahlung may cause muons to appear isolated in the central trackers but not the calorimeter. In order to check the purity of the candidate sample, the distributions of $M_{\mu\mu}$ for events falling into the following three categories are compared:

(1) Both muons are isolated in both the central trackers and the calorimeter.

(2) At least one of the muons is isolated in the central tracker and non-isolated in the calorimeter (likely to contain candidate events with final state bremsstrahlung).

(3) Any events not in categories (1) and (2) (likely to contain candidate events with jets as well as any residual $b\bar{b}$ background).

Figure 6.11(a) shows the distribution of $M_{\mu\mu}$ for candidate events in category (1) on top of that for events in category (2). The two distributions are normalised to the same number of events in the region $M_{\mu\mu} > 50$ GeV. The peak appears to be more smeared and shifted to a lower value in the distribution where at least one of the muons is non-isolated as would be expected in events with final state bremsstrahlung.

Figure 6.11(b) shows the distribution of $M_{\mu\mu}$ for events in category (1) on top of that for events in category (3). The two distributions are normalised to the same number of events in the region $M_{\mu\mu} > 50$ GeV. The two distributions have similar shapes which would suggest that the level of background is low. A value for the fractional background of $b\bar{b}$ events will be given in section 6.2.5.

Figure 6.12 shows the same plots as Figure 6.11 using $Z \rightarrow \mu^+\mu^-$ DMCS. The same effects are observed here, which indicates that the level of background is low. Since the Z/γ^* interference terms are not included there are less events in the low $M_{\mu\mu}$ region for the DMCS plots.

6.2.4 Efficiency of Isolation Cuts

Figure 6.13(a) shows $M_{\mu\mu}$ for the events that are rejected exclusively by the isolation cuts (plain histogram) and the expected shape and size of $M_{\mu\mu}$ for $Z/\gamma^* \rightarrow \mu^+\mu^-$

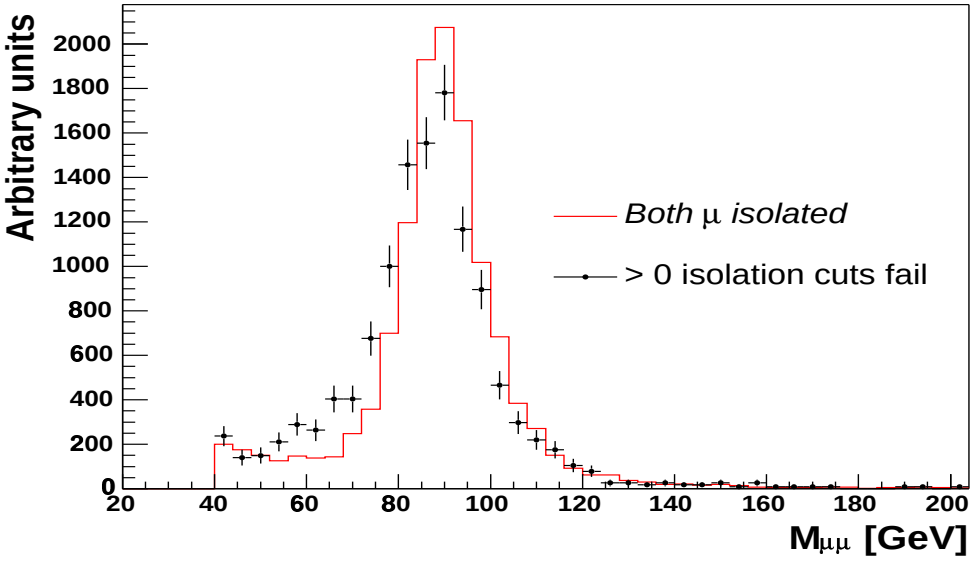

(a)

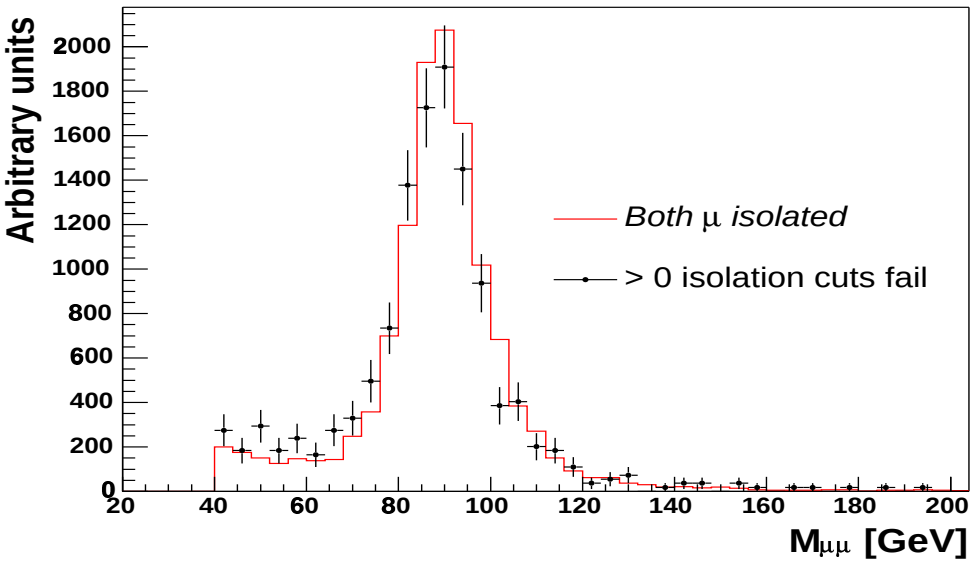

(b)

Figure 6.11: *Red histogram: Distribution of $M_{\mu\mu}$ for events with two isolated muons. Points with error bars: (a) Distribution of $M_{\mu\mu}$ for events where at least one of the muons is isolated in the central tracker and non-isolated in the calorimeter. (b) Distribution of $M_{\mu\mu}$ for events where at least one of the isolation cuts fails but that do not fall into category (a). The two distributions are normalised to the same number of events in the region $M_{\mu\mu} > 50$ GeV.*

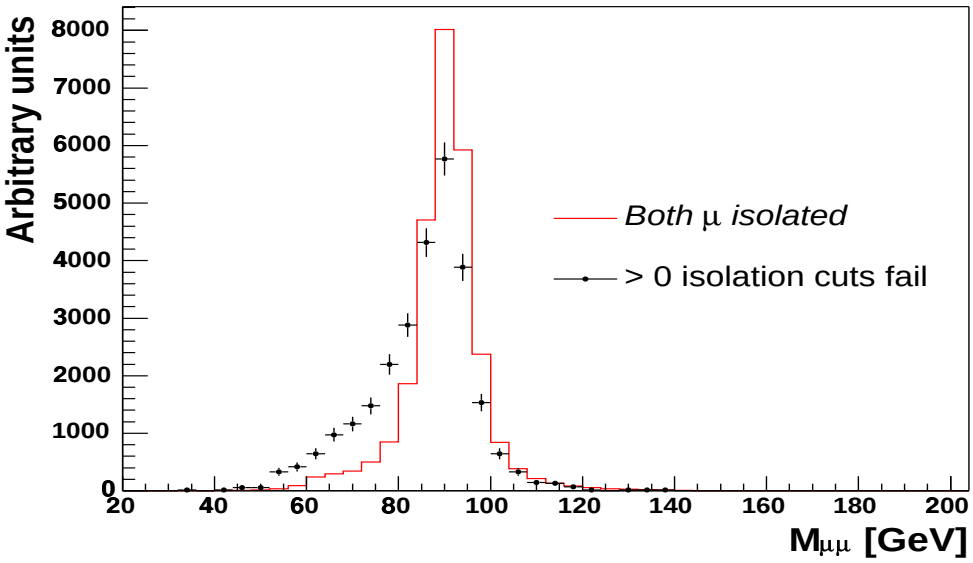

(a)

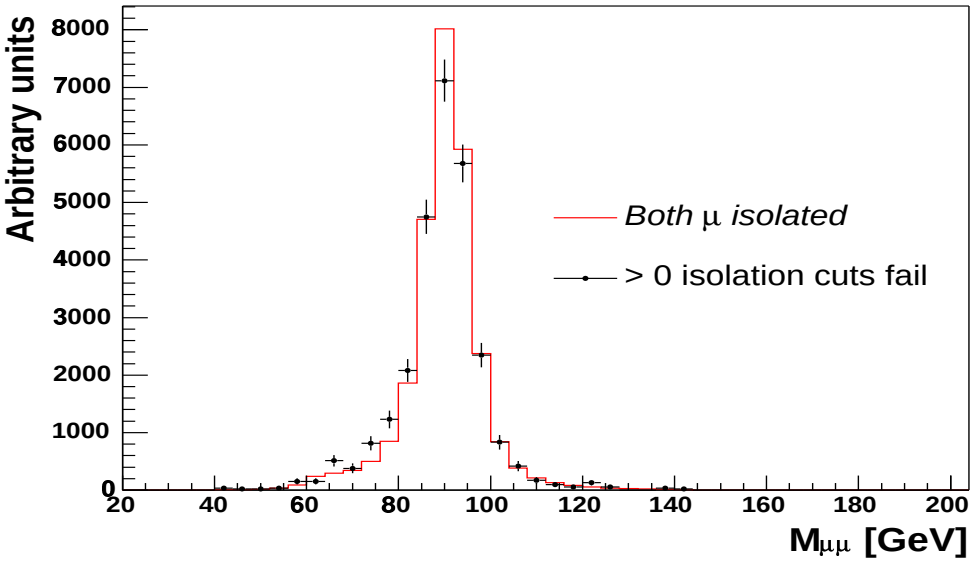

(b)

Figure 6.12: *Plots made using* $Z \to \mu^+\mu^-$ *DMCS. Red histogram: Distribution of* $M_{\mu\mu}$ *for events with two isolated muons. Points with error bars: (a) Distribution of* $M_{\mu\mu}$ *for events where at least one of the muons is isolated in the central tracker and non-isolated in the calorimeter. (b) Distribution of* $M_{\mu\mu}$ *for events where at least one of the isolation cuts fails but that do not fall into category (a). The two distributions are normalised to the same number of events in the region* $M_{\mu\mu} > 50$ *GeV.*

events rejected by the isolation cuts (blue solid histogram). The shape of the blue histogram is taken from that of signal events in the category where at least one of the isolation cuts fails. The size is found by fitting the histogram by eye to the region near m_Z in the plain histogram. By integrating over the blue shaded histogram, the number of signal events rejected by the isolation cuts is found to be 20.9, which corresponds to a fraction of 0.001 of the final sample. From these plots the efficiency for the isolation cuts is found to be

$$\varepsilon_{\text{isol}} = 0.999 \pm 0.001, \tag{6.4}$$

where a 100% uncertainty has been assigned to the number of signal events rejected by these cuts.

Figure 6.13(b) shows the plain histogram in Figure 6.13(a) minus the shaded histogram in order to demonstrate that the expected level of signal represented in the shaded histogram is sensible. The yellow shaded bands represent the 100% uncertainty on the efficiency.

6.2.5 Efficiency of Opposite Sign Requirement and $b\bar{b}$ Background Revisited

Figure 6.5 shows a flat distribution in $M_{\mu\mu}$ for the events exclusively rejected by the requirement that the two muons have opposite sign charge. This cut removes a fraction of 0.0047 of the potential candidate event sample. Some of these events are likely to originate from $b\bar{b}$ background where the muons have the same sign charge.[1] Some are likely to be $Z/\gamma^* \rightarrow \mu^+\mu^-$ events in which the sign of the curvature for one of the two muons has been mis-measured. Figure 6.10 shows that the relative fraction of events exclusively rejected by this cut is 0.0023 if both of the muon tracks in the central detector are required to have at least four SMT hits and at least 14 CFT hits. If it is assumed that no tracks with these quality requirements have a mis-measured sign, this suggests that a fraction of 0.0023 of the potential candidate event sample that are exclusively rejected by the opposite sign charge requirement are $b\bar{b}$ background and a fraction of 0.0024 are $Z/\gamma^* \rightarrow \mu^+\mu^-$ events with a muon with a mis-measured sign. The ratio of $b\bar{b}$ events containing a like sign high p_T di-muon

[1] $b\bar{b}$ events can have like sign muons if one of the muons comes from the c quark in the b decay or if one of the B mesons has undergone mixing.

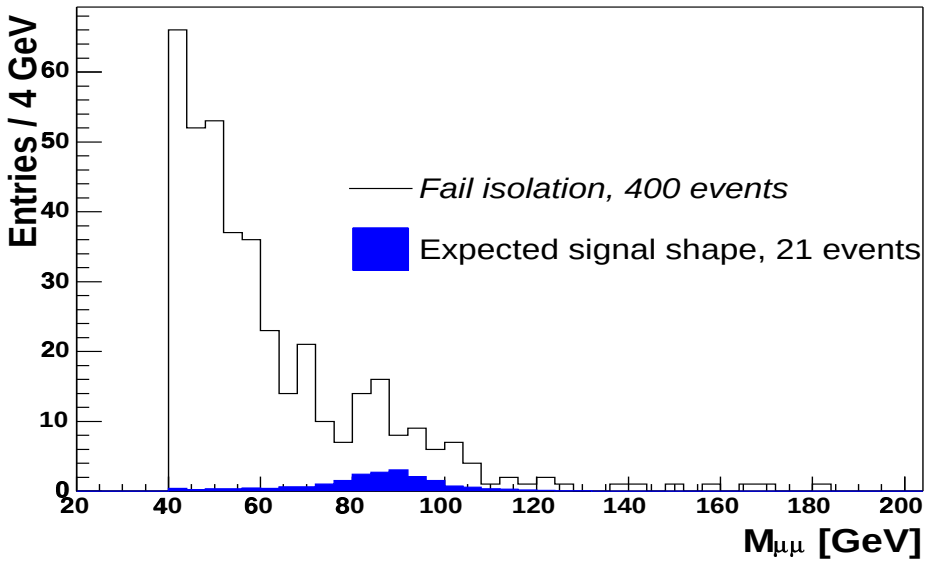

(a)

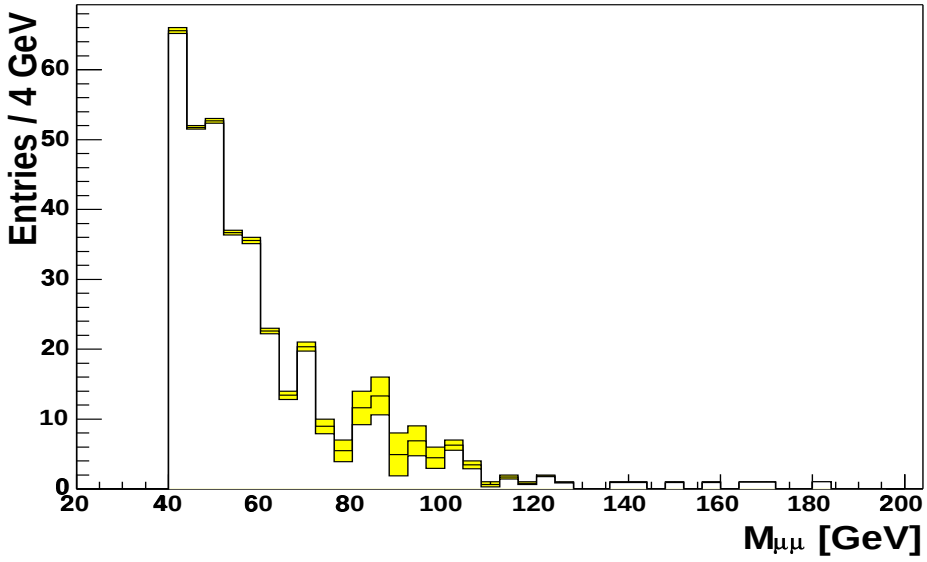

(b)

Figure 6.13: *(a) Plain histogram: $M_{\mu\mu}$ for events exclusively rejected by the isolation cuts. Blue shaded Histogram: Expected shape and size of $M_{\mu\mu}$ for signal events rejected by the isolation cuts. (b) $M_{\mu\mu}$ for events exclusively rejected by the isolation cuts with the expected shape of signal events subtracted. The shaded bands represent the 100% uncertainty assigned to the efficiency.*

pair to those containing an opposite sign high p_T di-muon pair is estimated in [24] using $b\bar{b}$ Monte Carlo to be 0.34. Therefore, for every $b\bar{b}$ event in Figure 6.5 there are two background $b\bar{b}$ events in the candidate sample. Using this and the fractions of events found above, the estimated efficiency for the opposite charge requirement is

$$\varepsilon_{\text{opposite\_q}} = 0.998 \pm 0.001 \tag{6.5}$$

and the estimated background fraction from $b\bar{b}$ events is

$$f_{\text{bb}} = 0.005 \pm 0.003. \tag{6.6}$$

The uncertainties in these assumptions are reflected in assigning a relative 50% uncertainty to the inefficiency of the like sign requirement and a 60% uncertainty to the level of $b\bar{b}$ background.

As a cross check of these measurements, Figure 6.14 shows the $M_{\mu\mu}$ distributions of like sign di-muon events falling into the following isolation categories:

(a) Both muons are isolated in both the central trackers and the calorimeter.

(b) One or two of the four isolation cuts fail.

(c) More than two of the four isolation cuts fail.

Presumably most of the like sign signal events will be in Figure 6.14(a), which contains 27 events. Once the efficiency for candidate events to have both muons isolated in both the central trackers and the calorimeter, $\varepsilon^{\text{all}}_{\text{isol}}$, is taken into account, $\varepsilon_{\text{opposite\_q}}$ can be deduced from this number. The ratio of the number of candidate events where both muons are isolated to the total number of candidate events gives

$$\varepsilon^{\text{all}}_{\text{isol}} = \frac{12273}{14352} = 0.86. \tag{6.7}$$

The number of candidate events rejected by the the opposite sign charge requirement is 31, which is obtained by dividing the number of events in Figure 6.14(a) by $\varepsilon^{\text{all}}_{\text{isol}}$. This corresponds to a fraction of 0.002 of the candidate event sample, which supports the value of $\varepsilon_{\text{opposite\_q}}$ obtained in equation 6.5.

Figure 6.14(b) (which contains 37 events) can be used to deduce the value of f_{bb}. If there are 31 candidate events rejected due to the opposite sign charge requirement then

$$31 \times (1 - \varepsilon^{\text{all}}_{\text{isol}}) = 4 \tag{6.8}$$

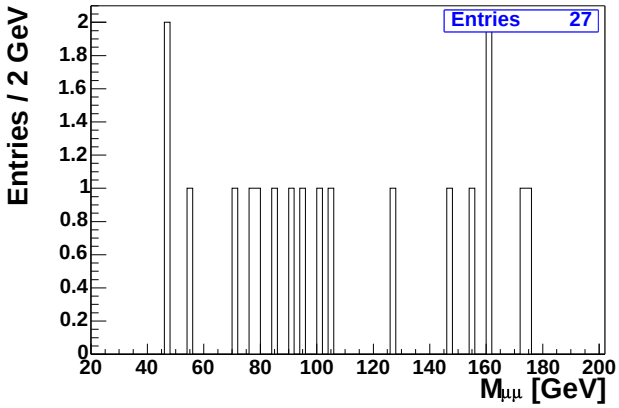

(a)

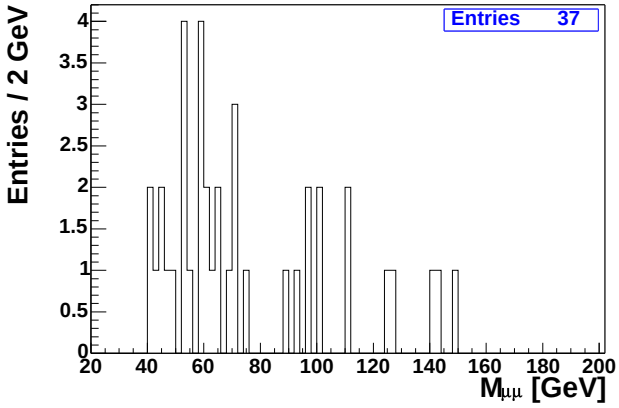

(b)

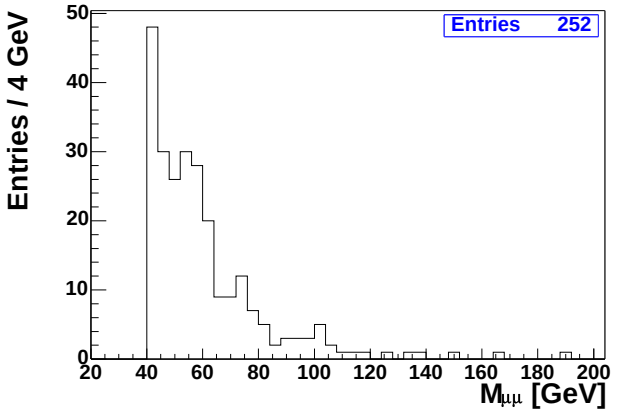

(c)

Figure 6.14: *Distribution of $M_{\mu\mu}$ for the like sign di-muon events in which (a) all isolation cuts pass, (b) one or two of the four isolation cuts fail and (c) more than two of the four isolation cuts fail.*

of them will have at least one isolation cut failing and so will be included in these 37 events. Assuming two opposite sign $b\bar{b}$ events for every like sign $b\bar{b}$ event, there should be

$$2 \times (37 - 4) = 66 \tag{6.9}$$

remaining $b\bar{b}$ events in the candidate sample, which supports the value of $f_{\rm bb}$ obtained in equation 6.6.

The shape of the distribution of $M_{\mu\mu}$ in the like sign non-isolated events in Figure 6.14(c) is similar to that in Figure 6.13(b) which supports the method used to subtract the signal from the background when calculating $\varepsilon_{\rm isol}$ in section 6.2.4.

6.2.6 Cosmic Rays

The difference in the times measured in the A-layer scintillators[2] by the two muons, Δt_A, should be small for $Z/\gamma^* \rightarrow \mu^+\mu^-$ events, since the muons should take approximately the same time to reach the A-layer. The time for a cosmic muon to traverse the detector will be ~ 20 ns. Figure 6.15 shows Δt_A as a function of $\Delta\alpha_{\mu\mu}$ of the muon pair before the cut on $\Delta\alpha_{\mu\mu}$ has been applied. Cosmic events would be expected to have a small $\Delta\alpha_{\mu\mu}$ and a high $|\Delta t_A|$. It is clear that the signal events are well separated from the cosmic events and that the choice of 0.05 for a cut on $\Delta\alpha_{\mu\mu}$ is a good one. The number of events with a high $|\Delta t_A|$ that appear to be in the tail of the cosmic $\Delta\alpha_{\mu\mu}$ distribution is small which suggests that the cosmic background is small. In order to cross check this, a plot of the speed of the muon is made as if it were a cosmic traversing the detector. The distance travelled is the distance between muon 1 and muon 2, measured in the muon detectors and the time is the difference between the scintillator times of muon 1 and muon 2. For a cosmic this would be expected to be near to the speed of light and for a $Z/\gamma^* \rightarrow \mu^+\mu^-$ event it would be infinitely large. Figure 6.16 shows the speed for candidate events. There are 68 events with a speed between 0 and 50 cm ns^{-1}. If half of these are assumed to be from cosmic events and half of them from $Z/\gamma^* \rightarrow \mu^+\mu^-$ events in the tail of the distribution, the fractional background from cosmic events is estimated to be

$$f_{cos} = 0.002 \pm 0.002, \tag{6.10}$$

[2]If either of the muons has no hits in the A-layer scintillators, then the time from the BC-layer scintillators is used. The time measured by the A- and BC-layer scintillators is corrected for the expected time of flight of the muons to the respective layers so that it should be close to zero.

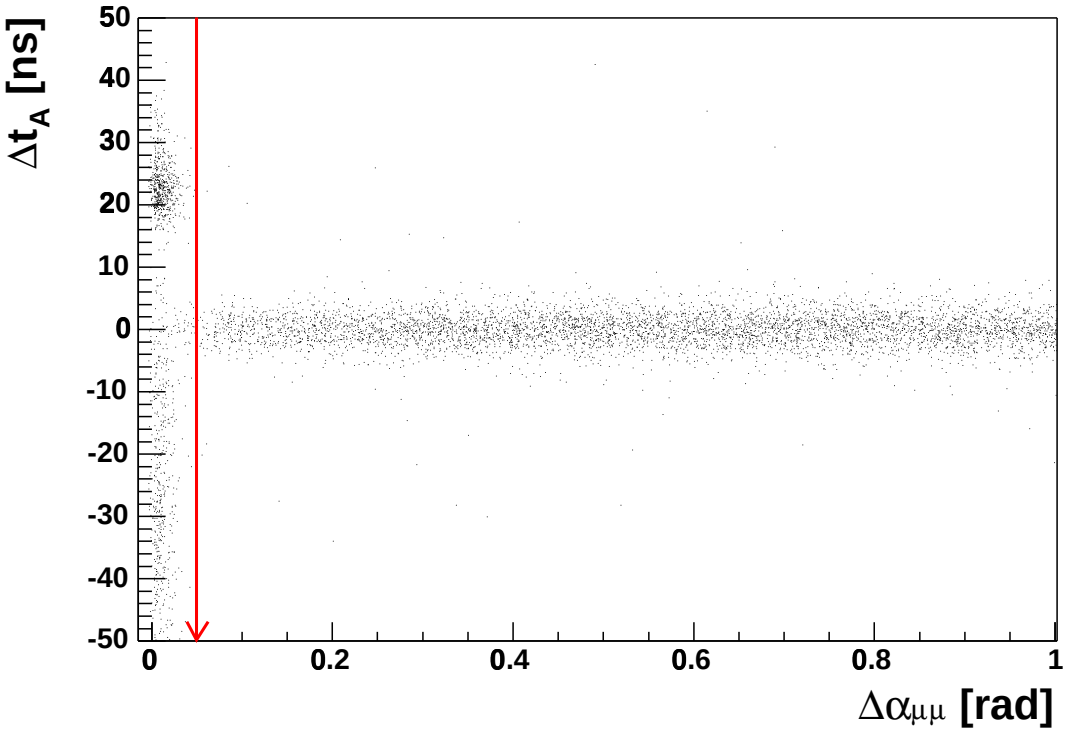

Figure 6.15: *Δt_A versus $\Delta\alpha_{\mu\mu}$ for events that have passed all cuts but that on $\Delta\alpha_{\mu\mu}$. The red arrow indicates the position of the cut.*

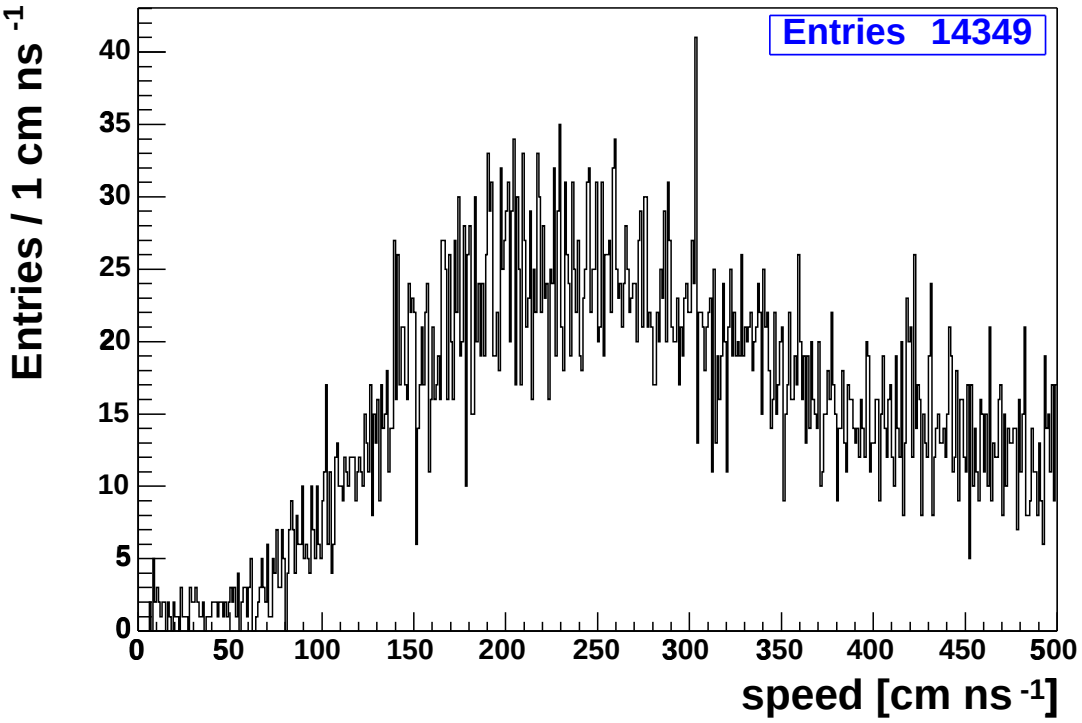

Figure 6.16: *Speed of muon pair in candidate events as if they were one muon traversing the detector.*

where a relative 100% uncertainty to the number of background events has been assigned.

Figure 6.8 shows the distribution of $M_{\mu\mu}$ for events rejected by the $\Delta\alpha_{\mu\mu}$ and *dca* cuts. Inspection of this plot shows that most of the rejected events are background. The efficiency of the $\Delta\alpha_{\mu\mu}$ cut is measured using PMCS to be 0.004.

The distribution of $M_{\mu\mu}$ for the 302 events that are exclusively rejected by the *dca* cut does not peak at the Z mass. However, we would expect signal events that fail this cut to have a mis-reconstructed mass as a poor resolution in p_T would be expected for tracks with a large *dca*. In order to estimate the amount of signal events rejected by this cut, a plot of the *dca* of one of the muon tracks is plotted against that of the other muon track before the *dca* cuts have been applied, as shown in Figure 6.17. Since the *dca* cut is also expected to suppress the $b\bar{b}$ background, this plot is only made for events in which both muons are isolated in both the central detectors and the calorimeter. In signal events that fail the *dca* cut, only one of the tracks would be expected to have a large *dca* since it is likely due to mis-reconstruction. In cosmic events the *dca* of both tracks would be expected to be of equal magnitude and opposite sign. Most of these events have a shape that is consistent with that expected from signal with only a few cosmic events. In order to check this, Figure 6.18 shows the speed of the muon pair for events that fail the *dca* cut exclusively. There are 32 events with a speed between 0 and 50 cm ns^{-1}, these are considered to be cosmics. There remains 135 out of the 167 isolated events that fail the *dca* cut. Correcting for the efficiency of requiring both muons to be isolated this becomes

$$\frac{135}{\varepsilon_{\rm isol}^{\rm all}} = 157 \tag{6.11}$$

events. DMCS samples for $Z/\gamma^* \to \mu^+\mu^-$ and $Z/\gamma^* \to \tau^+\tau^-$ are used to estimate the fraction of $Z/\gamma^* \to \tau^+\tau^-$ background in this sample which is found to be 23%. This leaves 121 events, or a fraction of 0.008 of the candidate sample, that may be considered as lost signal.

From these arguments the total fraction of events rejected by the cosmic cuts ($\Delta\alpha_{\mu\mu}$ and *dca*) is estimated to be 0.004 + 0.008 = 0.012. An efficiency for the cosmic cuts of

$$\varepsilon_{\rm cosmic} = 0.988 \pm 0.006 \tag{6.12}$$

is obtained. A relative 50% uncertainty has been assigned to the estimation of the number of events rejected by these cuts.

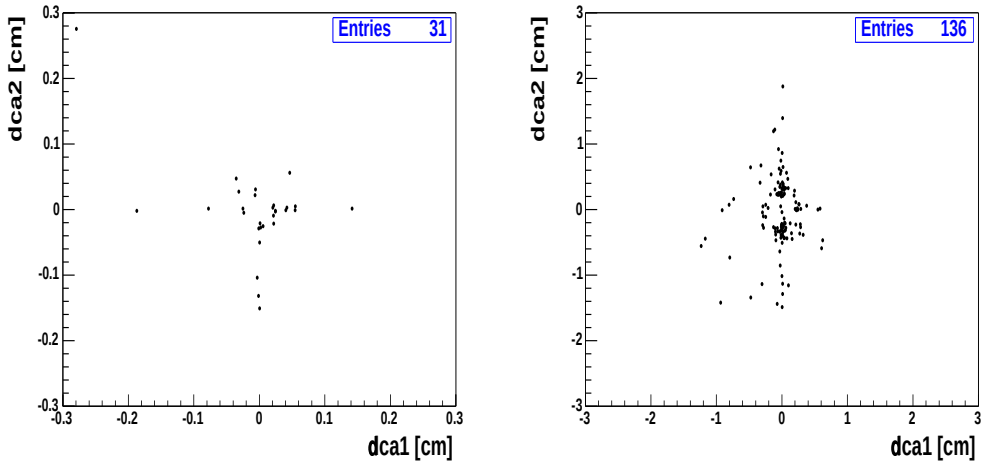

(a) (b)

Figure 6.17: *Distribution of dca for one muon track versus dca for the other muon track for events that fail the dca cut but have passed all other cuts, with the additional requirement that all four isolation cuts pass. (a) For events where both tracks have SMT hits. (b) For events where at least one track has no SMT hits.*

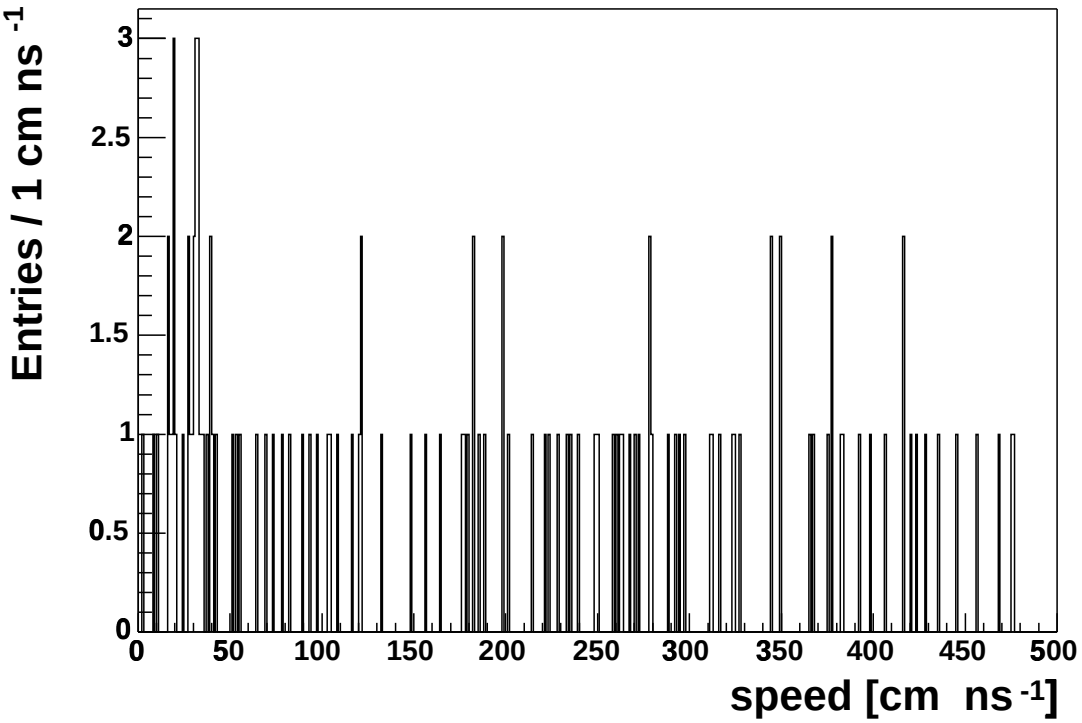

Figure 6.18: *Speed of muon pair in events rejected by the dca cut as if they were one muon traversing the detector.*

6.2.7 $Z/\gamma^* \to \tau^+\tau^-$ Background

$Z/\gamma^* \to \tau^+\tau^-$ events in which both taus decay to a muon could mimic a $Z/\gamma^* \to \mu^+\mu^-$ event. In addition, $Z/\gamma^* \to \tau^+\tau^-$ events in which one tau decays to a muon and the other decays hadronically, with a hadron *punching through* into the muon chambers and faking a muon, could mimic a $Z/\gamma^* \to \mu^+\mu^-$ event. The p_T spectrum of the muons will be softer than that in $Z/\gamma^* \to \mu^+\mu^-$ events but some events could pass the selection criteria. The number of $Z/\gamma^* \to \tau^+\tau^-$ events for every $Z/\gamma^* \to \mu^+\mu^-$ event is found to be 0.0051 ± 0.0003 by comparing the relative numbers of $Z/\gamma^* \to \mu^+\mu^-$ and $Z/\gamma^* \to \tau^+\tau^-$ DMCS events passing the selection criteria and 0.00408 ± 0.00008 by comparing the relative numbers of $Z/\gamma^* \to \mu^+\mu^-$ and $Z/\gamma^* \to \tau^+\tau^-$ PMCS events passing the selection criteria. The central value from DMCS is used as it is thought to be more realistic at modelling the possibility of hadronic *punch through*. The difference between the two values is taken to be a systematic uncertainty so that a value:

$$f_{\tau\tau} = 0.005 \pm 0.001 \tag{6.13}$$

is obtained.

6.2.8 Background From W + Jets and Di-boson Events

It is possible that a $W \to \mu\nu$ event with an additional high p_T muon from a jet could pass the event selection criteria. If the fraction of $W \to \mu\nu$ events with a high p_T muon from a jet is assumed to be roughly the same as the fraction of $Z/\gamma^* \to \mu^+\mu^-$ events with a high p_T muon from a jet, this background can be studied using candidate events. The total number of candidate events where more than one pair of muons passes all cuts is six. Two of these events have one of the three muons in the event non-isolated, the other four have three isolated high p_T muons. Those that fall into the former category may be considered to be $Z/\gamma^* \to \mu^+\mu^-$ events with a high p_T muon from a jet. Since the cross section for $W \to \mu\nu$ is a factor of ~ 10 larger than that for $Z/\gamma^* \to \mu^+\mu^-$, the background from W + jets events is found to be 20 ± 14 events. The 4 ± 2 events that contain three isolated high p_T muons are taken to be background from di-boson (WW, WZ, ZZ) events, where both bosons decay to muons. The total fractional background from W + jets and di-boson events is found

to be

$$f_{\mathrm{W}} = 0.002 \pm 0.001. \tag{6.14}$$

6.3 Measurement of Tracking Efficiency

It is possible to select a sample of clean $\mathrm{Z}/\gamma^* \to \mu^+\mu^-$ events, free from significant background, even if only one of the muon tracks produced in the central detectors is reconstructed. By these means the efficiency for central track reconstruction, $\varepsilon_{\mathrm{track}}$, may be evaluated using the data.

The event selection requires evidence that a pair of high p_T muons is produced. One muon, the *control muon*, is identified by requiring a track in the central detectors that is matched to a track of at least loose quality in the muon detectors. The second muon, the *test muon*, is required to be identified as a high p_T^{local} (p_T measured in the muon system) track of at least loose quality in the muon detector, but no requirement is made on the presence of a matched central detector track. Where possible, the selection criteria are tighter than those for candidate events so as to maintain a pure sample after the relaxation of the requirement of two central tracks. The event selection cuts, shown schematically in Figure 6.19, are as follows:

1. *Control muon:* $p_T > 30$ GeV.
2. *Control muon:* Required to be isolated[3] in both the calorimeter and central detectors, satisfying the same conditions as is described in section 6.2.
3. *Control muon:* $dca < 0.02$ cm.
4. *Test muon:* required to lie within the geometrical acceptance of the muon detector as defined in section 6.2.
5. *Test muon:* $p_T^{\mathrm{local}} > 15$ GeV. [4]
6. $\Delta R_{\mu\mu} > 2.0$, where $(\Delta R_{\mu\mu})^2 = (\Delta\phi_{\mu\mu})^2 + (\Delta\eta_{\mu\mu})^2$ and $\Delta\phi_{\mu\mu}$ and $\Delta\eta_{\mu\mu}$ are the differences in ϕ and η between the two muons.

[3] Since the tracking efficiency may be sensitive to the isolation of the muon, no isolation requirements are made for the test muon.

[4] Some loose muons do not have a valid p_T^{local} measurement. If this is the case the muon does not satisfy the test muon requirements.

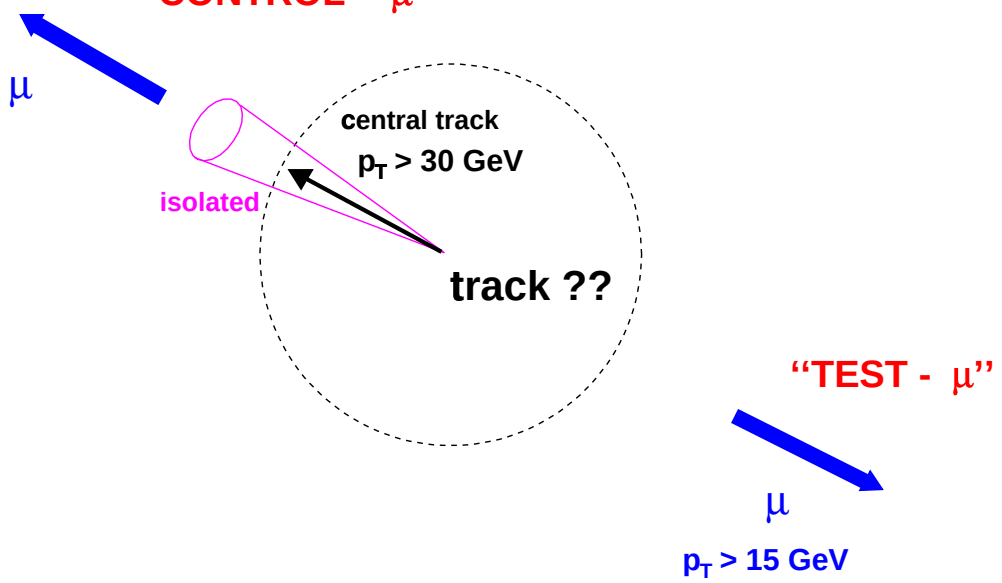

Figure 6.19: *Schematic view of the event selection for the tracking efficiency sample.*

7. $|\Delta t_A| < 6$ ns.

8. Events are required to have been selected by one of the di-muon triggers that does not have a Level 3 track requirement.

The meaning of the various symbols are as given in section 6.2. If both muons in the event satisfy the conditions for the control and test muons then the event is used twice in the efficiency measurement.

In order to have confidence that this analysis gives a reliable measure of the central tracking efficiency, it is important to demonstrate that the level of background is low, particularly in the inefficient subsample in which a track is not found for the test muon. Figure 6.20 shows the distribution of Δt_A after all other selection criteria have been applied. A plot is made for each of the following categories:

(a) the test muon is matched[5] to a central track with $p_T > 15$ GeV,

(b) the test muon is matched to a central track with $p_T < 15$ GeV,

(b) the test muon is not matched to a central track.

[5]If no track is matched to the muon but there is a $p_T > 15$ GeV track contained within a cone of width $\Delta R < 0.5$ around the test muon then this event is counted as efficient. The inefficiency of matching the central track to the muon track is accounted for in the measurement of the loose muon identification efficiency, as described in section 6.4.

Note that events falling into the first two categories are counted as efficient and those falling into the third category are counted as inefficient.

Figure 6.21(a) shows the p_T of the control muon for events where the test muon is found to have a central track associated with it on top of that for events where the test muon is found not to have a central track associated with it. The distributions are normalised to the same number of events. Although the distributions are similar, the one for inefficient events seems to peak at a slightly lower value. This is expected to be due to the η distribution of the tracking efficiency (as shown below). Inefficient test muons are more likely to be at larger values of $|\eta|$ since the tracking efficiency is worse there. The average p_T of muons will decrease at larger η values which will lead to the discrepancy in the p_T distributions shown. In order to check that this assumption is valid, the same distributions are shown for $Z \rightarrow \mu^+\mu^-$ DMCS in Figure 6.21(b). The same effect is observed here.

Figure 6.22(a) shows the distribution of $M_{\mu\mu}^{loc}$ for the selected events, where $M_{\mu\mu}^{loc}$ is $M_{\mu\mu}$ calculated using the kinematic information from the central track for the control muon and that from the local muon track for the test muon. This is done to enable a direct comparison between the events in which the central track is found and those in which it is not found. Inefficient events are plotted on top of efficient events, with the histograms normalised to the same number of events. The distribution of inefficient events is slightly broader than that for efficient events. In order to demonstrate that this is due to inefficient muons having larger $|\eta|$ values rather than more background in that sample, the same distributions are shown for $Z \rightarrow \mu^+\mu^-$ DMCS in Figure 6.22(b). The same effect is seen here.

The distributions for the efficient and inefficient cases in Figures 6.20–6.22 are very similar, showing that the composition of the two samples is similar.

From the number of events in the efficient and inefficient subsamples an average value of the tracking efficiency of

$$\varepsilon_{\text{track}} = 0.951 \pm 0.002 \tag{6.15}$$

is found. Note that this efficiency is an average over the available control sample and there is a bias due to the geometric distributions. The quantitative efficiency that is used in the evaluation of the total efficiency (as discussed in section 6.6.2) is therefore represented in Figure 6.23, which shows the tracking efficiency as a function of η_{CFT} in bins of z of the interaction point.

Candidate events are selected with certain isolation criteria, given in section 6.2. There are no isolation cuts made on the test muon in the tracking efficiency sample. Since the tracking efficiency may be sensitive to the isolation of the muon this is a potential source of systematic uncertainty. In order to investigate this potential bias the tracking efficiency is measured for the following categories of isolation for the test muon:

1. Isolated in the central trackers and the calorimeter ($\varepsilon = 0.951 \pm 0.002$).
2. Isolated in the central trackers but not the calorimeter ($\varepsilon = 0.94 \pm 0.01$).
3. Isolated in the calorimeter but not the central trackers ($\varepsilon = 0.96 \pm 0.01$).
4. Non-isolated in the central trackers and the calorimeter ($\varepsilon = 0.95 \pm 0.01$).

The tracking efficiency is then recalculated by weighting the separate efficiencies by the number of candidate muons that fall into the above four categories. The result obtained is 0.951 which is in complete agreement with the average efficiency found above.

In addition to tracking inefficiencies, an important potential source of systematic uncertainty in this analysis is the possibility that a central track is badly mis-measured and reconstructed with sufficiently low p_T that it fails the cut at 15 GeV. There are 92 events that have one (control) muon with $p_T > 30$ GeV and one (test) muon with $p_T < 15$ GeV which corresponds to a 0.8% inefficiency. It is assumed that this inefficiency is accounted for when the efficiency including kinematic cuts is calculated using PMCS as described in section 6.6.

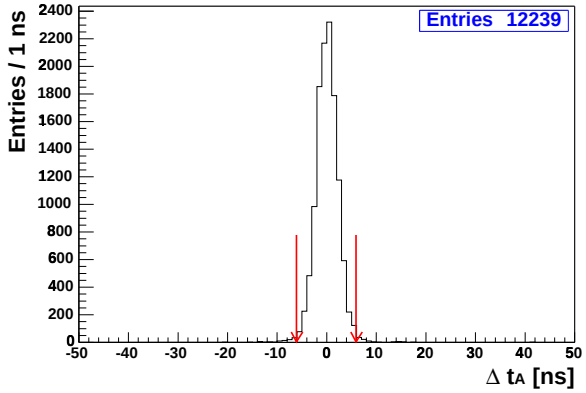

(a)

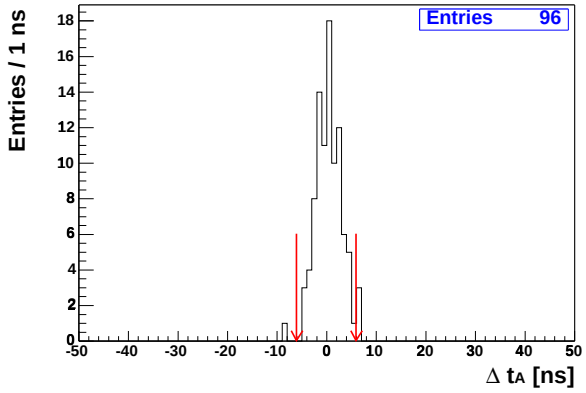

(b)

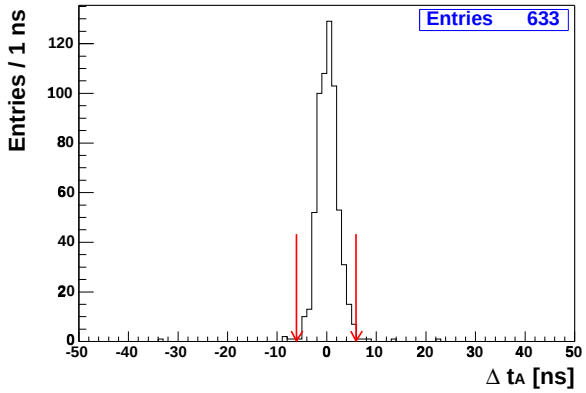

(c)

Figure 6.20: **Central track efficiency study:** *Distribution of Δt_A after all cuts have been applied for those cases in which the test muon is (a) matched to a central detector track with $p_T > 15$ GeV, (b) matched to a central detector track with $p_T < 15$ GeV and (c) not matched to a central detector track. The red arrows indicate the position of the cut.*

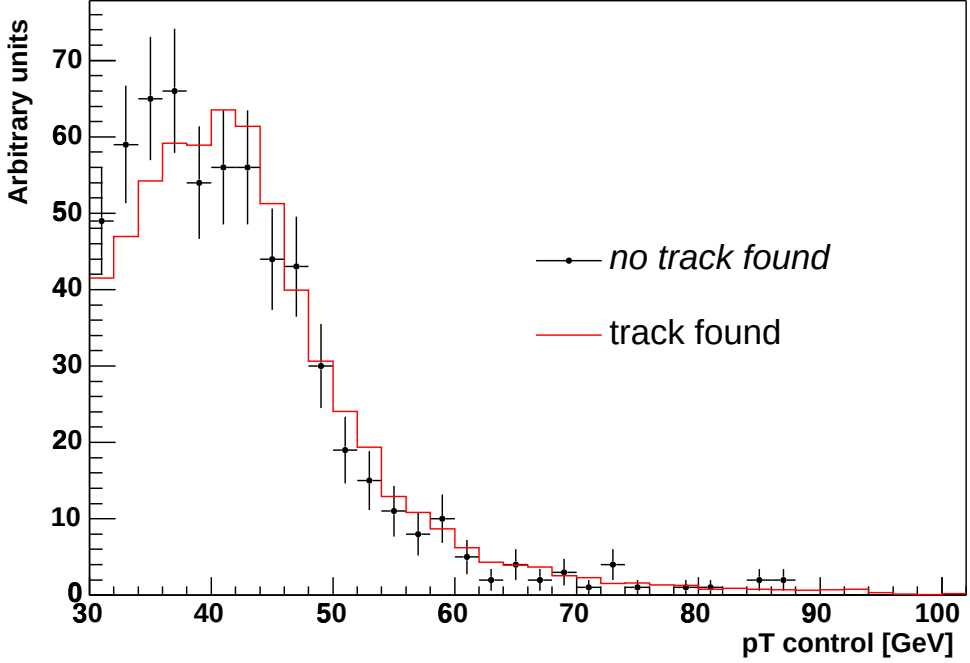

(a)

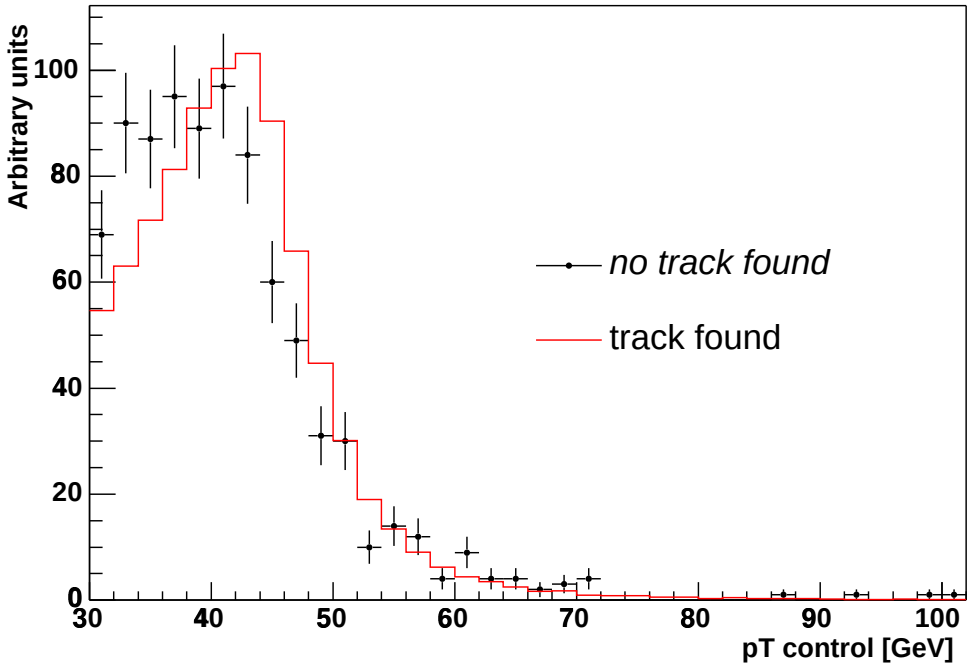

(b)

Figure 6.21: **Central track efficiency study:** *Distribution of p_T of the control muon. Events where the test muon is not matched to a central track (points with error bars) against events where it is matched to a central track (red histogram). Distributions are normalised to the same number of events. (a) Data. (b) DMCS.*

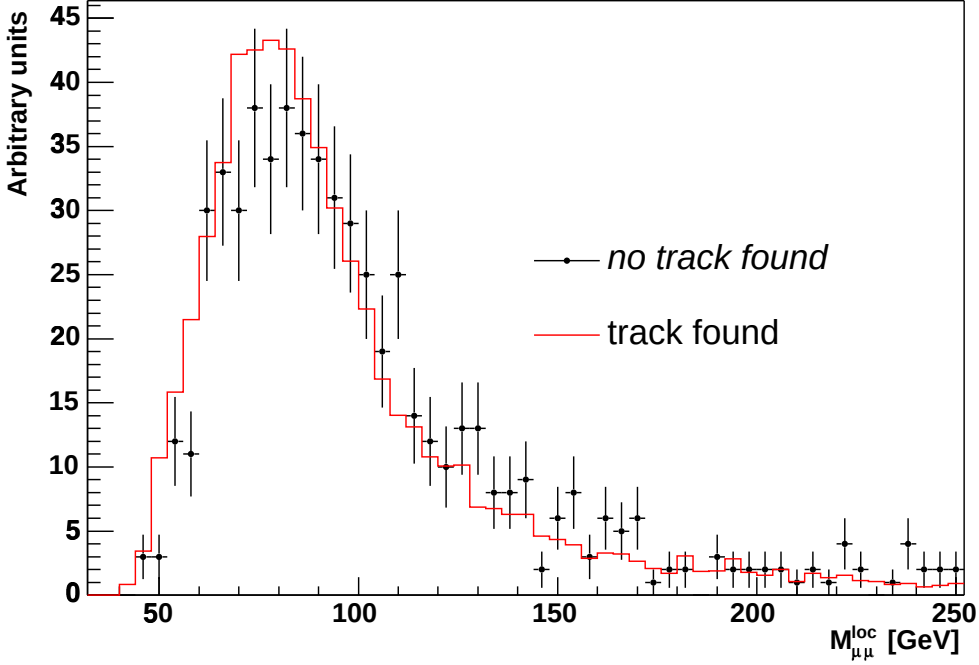

(a)

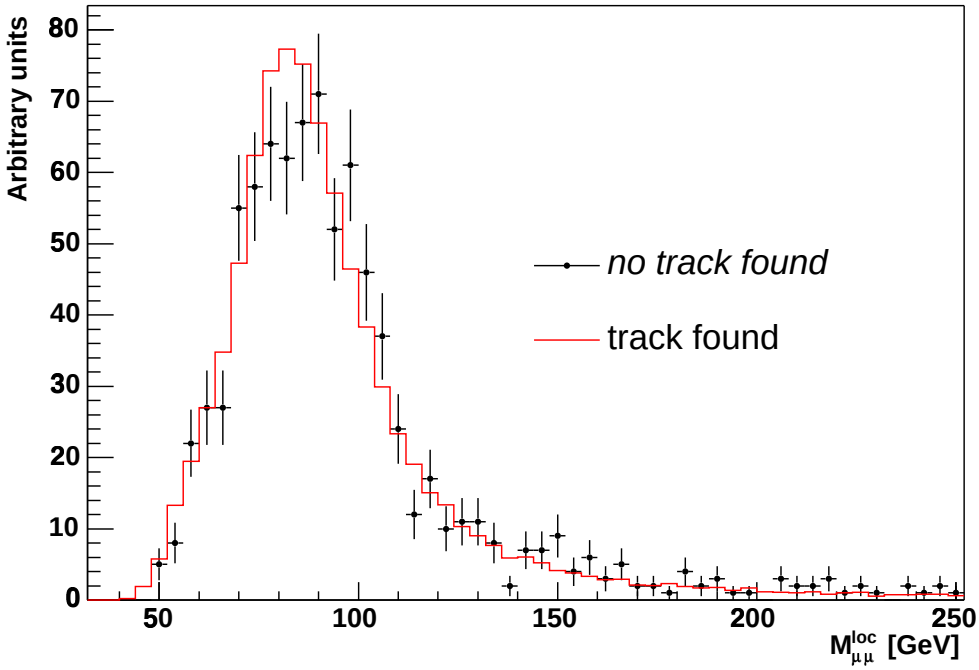

(b)

Figure 6.22: **Central track efficiency study:** *Distribution of $M^{loc}_{\mu\mu}$. Events where the test muon is not matched to a central track (points with error bars) against events where it is matched to a central track (red histogram). Distributions are normalised to the same number of events. (a) Data. (b) DMCS.*

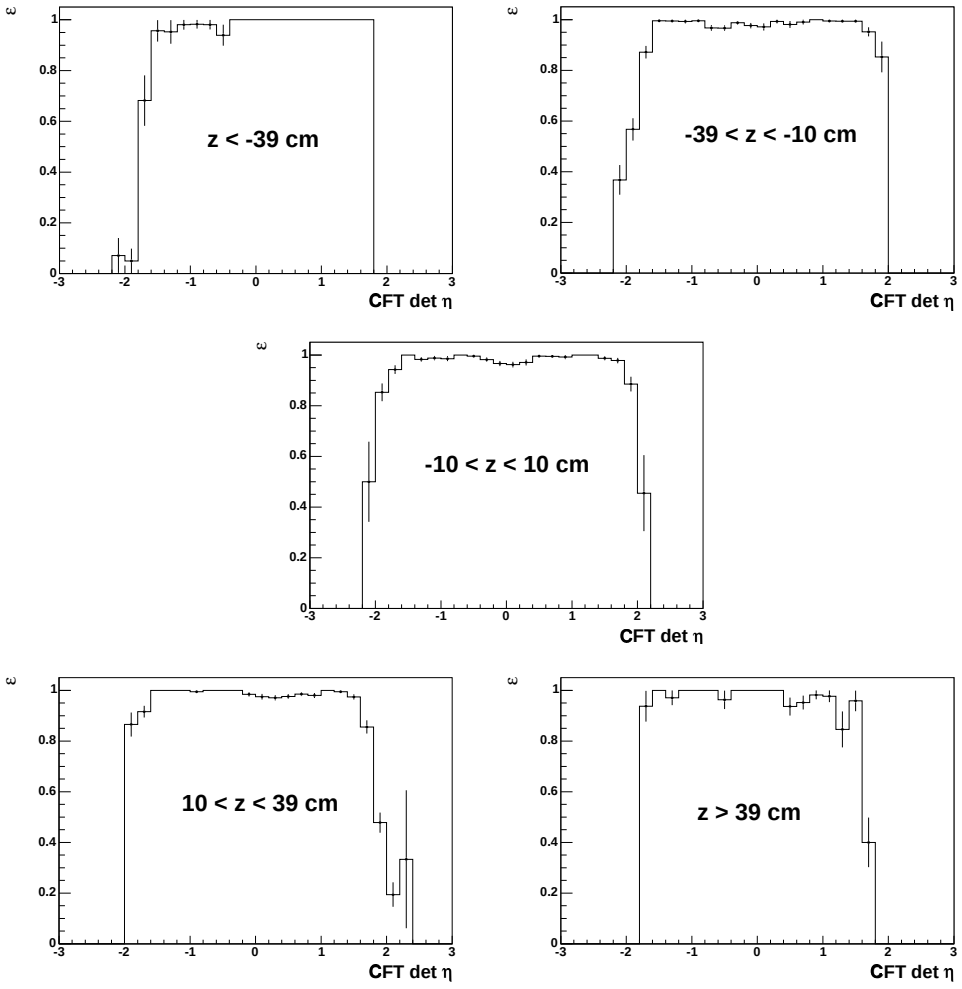

Figure 6.23: *The tracking efficiency as a function of η_{CFT} in bins of z of the interaction point.*

6.4 Measurement of Muon Identification Efficiency

It is possible to trigger on and select a sample of clean di-muon events, free from significant background, even if only one of the two muons is reconstructed as loose in the muon detector and matched to a track in the central detectors. By this means the loose quality muon reconstruction efficiency, $\varepsilon_{\text{loose}}$, may be evaluated using the di-muon data. The event selection requires evidence that a pair of high p_T muons is produced. One muon, the *control muon*, is identified by requiring a central track that is matched to a track of at least *medium* quality in the muon detector (see appendix A for a definition of medium muons). The control muon is required to have fired a single muon trigger. The second muon, the *test track*, is identified by requiring a track in the central detectors. Where possible, the selection criteria are tighter than those for candidate events so as to maintain a pure sample after the relaxation of the requirement of two muon objects.

In order to have confidence that this analysis gives a reliable measure of the muon reconstruction efficiency, it is important to demonstrate that the level of background is low, particularly in the inefficient subsample in which the test track is not matched to a loose muon. Figures 6.25–6.27 show, for selected cuts, distributions of the cut variable after all other cuts have been applied for (a) efficient events in which the test track is matched to a loose muon and (b) inefficient events in which the test track is not matched to a loose muon. The event selection cuts, shown schematically in Figure 6.24, are as follows:

1. *Control muon:* $p_T > 30$ GeV.

2. *Test track:* $p_T > 20$ GeV.

3. *Both muons:* Required to be isolated in both the calorimeter and central detectors, satisfying the same conditions as described in section 6.2.

4. *Test track:* Required to have $\sum_{R=0}^{0.1} E_T^{\text{cells}} < 8$ GeV, where $\sum_{R=0}^{0.1} E_T^{\text{cells}}$ is the sum of the transverse energies of calorimeter cells for $R < 0.1$ around the direction of the muon [Figure 6.25]. [6]

[6] The cut on $\sum_{R=0}^{0.1} E_T^{\text{cells}}$ is applied to reduce the background from $Z \to \tau^+\tau^-$ events where one of the taus decays to a muon and the other decays hadronically.

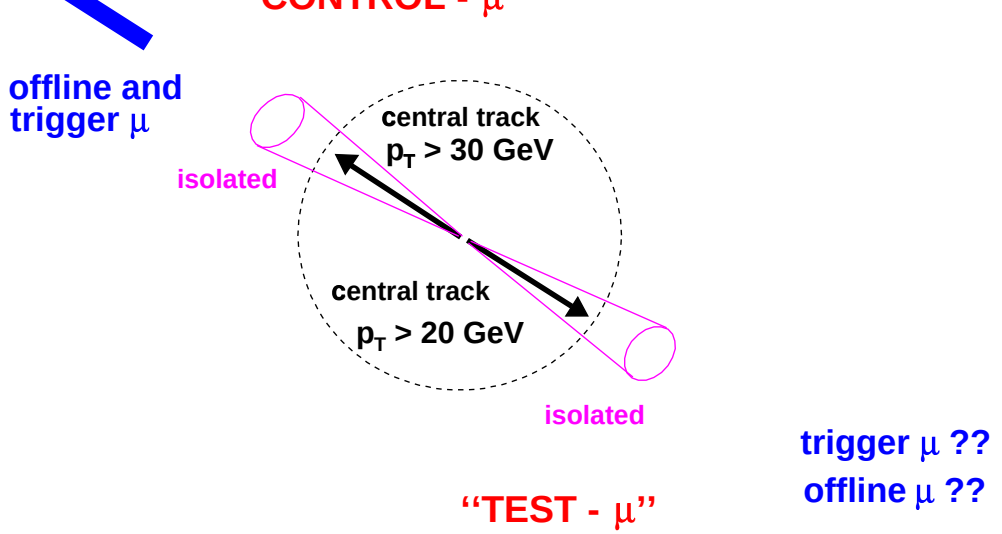

Figure 6.24: *Schematic view of the event selection for the muon identification efficiency sample.*

5. *Control muon:* $|t_A| < 7$ ns where t_A is the time measured in the A-layer scintillator counters.[7]

6. *Test track:* χ^2 per degree of freedom of track required to be < 3 [Figure 6.26].

7. *Test track:* Number of CFT hits required to be > 7.

8. *Test track:* Required to point to a region within the geometrical acceptance of the muon detector as defined in section 6.2.

9. *Test track:* $dca < 0.02$ cm for tracks containing SMT hits and $dca < 0.2$ cm for tracks with no SMT hits.

10. *Control Muon:* $dca < 0.02$ cm for all tracks.

11. $\Delta\alpha_{\mu\mu}$ is required to be > 0.05 [Figure 6.27].

12. $\Delta R_{\mu\mu} > 2.0$.

13. The muons are required to be oppositely charged.

14. (a) The event is required to be selected by a single muon trigger (MU_W_L2M(3,5)_TRK10, MUW_W_L2M(3,5)_TRK10,

[7] If the muon has no hits in the A-layer scintillators, then the time from the BC-layer scintillators is used.

MU_W_L2M0_(2)PtR5 or MU_W_A_L2M5_PtR10). The meaning of each component in these trigger names in given Appendix C.

(b) The control muon is required to be associated with all the muon objects required in the trigger that selects the event.

If both muons in the event satisfy the conditions for the control and test muons then the event is used twice in the efficiency measurement.

Figure 6.28 shows the distribution of p_T for the control muon for the inefficient subsample on top of the efficient subsample. The histograms are normalised to the same number of events. Figure 6.29 shows the $M_{\mu\mu}$ distribution. The two distributions in both figures are very similar, showing that the composition of the two samples is similar.

The loose muon efficiency is lower in the boundaries between the octants of the muon detectors. The loose muon efficiency is therefore plotted as a function of η_A for muons that are 'in the boundary' and 'out of the boundary'[8] as is shown in Figure 6.30. This is the quantitative efficiency used in the evaluation of the total efficiency as will be discussed in section 6.6.2.

The average value of the loose muon reconstruction efficiency is found by dividing the number of efficient events by the total number of events. A value of

$$\varepsilon_{\text{loose}} = 0.939 \pm 0.002 \tag{6.16}$$

is obtained. Note that this efficiency is an average over the available control sample and there is a bias due to the η_A / ϕ_A distributions.

Figure 6.26, which shows the χ^2 per degree of freedom of test tracks before this cut has been applied, shows a different distribution for efficient and inefficient events. This is a potential source of systematic uncertainty as the purity of the samples may be slightly different. In order to account for this effect the χ^2 cut is varied from 1.5 to 4.5. The change in the average efficiency after varying this cut is 0.18%. This leads to a change on the acceptance of 0.36% which is quoted as a systematic uncertainty.

[8] In the central region tracks are defined as 'in the boundary' if they are < 0.02 rad in ϕ_A away from the boundaries at x_A=0 and y_A=0 and if they are < 0.03 rad away from the boundaries at $|x_A|$=$|y_A|$. In the forward region tracks are defined as 'in the boundary' if they are < 5 cm in x_A or y_A away from the boundaries at x_A=0 and y_A=0 and if they are < 20 cm in $x_A - y_A$ away from the boundaries at $|x_A|$=$|y_A|$.

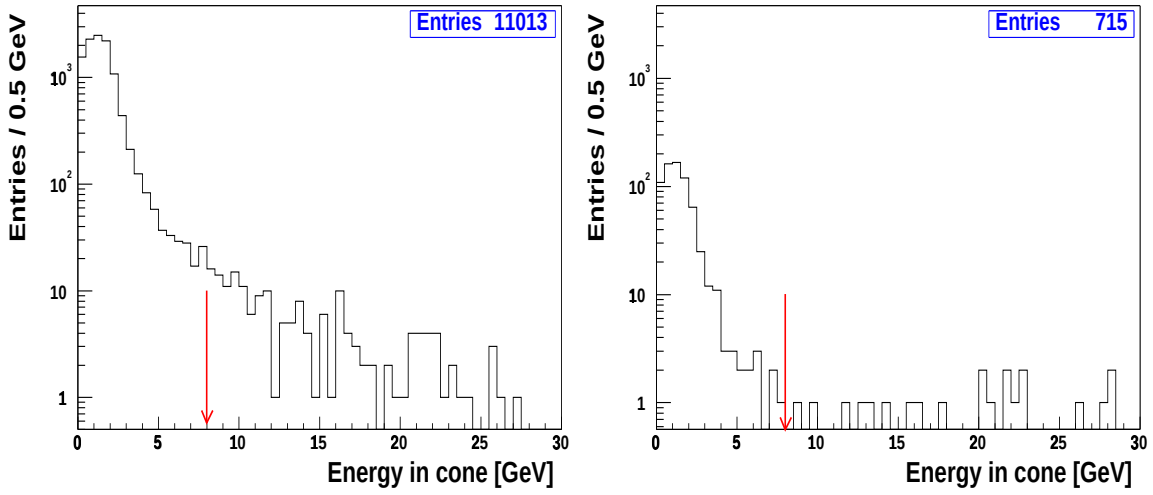

(a) (b)

Figure 6.25: **Loose muon efficiency study:** *Distribution of* $\sum_{R=0}^{0.1} E_T^{\text{cells}}$ *for the test muon after all other cuts have been applied. Those cases in which (a) the test track is matched to a loose muon and (b) the test track is not matched to a loose muon. The red arrows indicate the position of the cut.*

One potential source of background in this study is from $Z/\gamma^* \to \tau^+\tau^-$ events. If one of the taus decays to a muon and the other decays hadronically the event would appear as inefficient. In order to check for $Z/\gamma^* \to \tau^+\tau^-$ background the efficiency study is performed using $Z/\gamma^* \to \mu^+\mu^-$ and $Z/\gamma^* \to \tau^+\tau^-$ DMCS samples. The change in the efficiency when the fraction of $Z/\gamma^* \to \tau^+\tau^-$ events in the samples are included is 0.01% and is taken to be negligible.

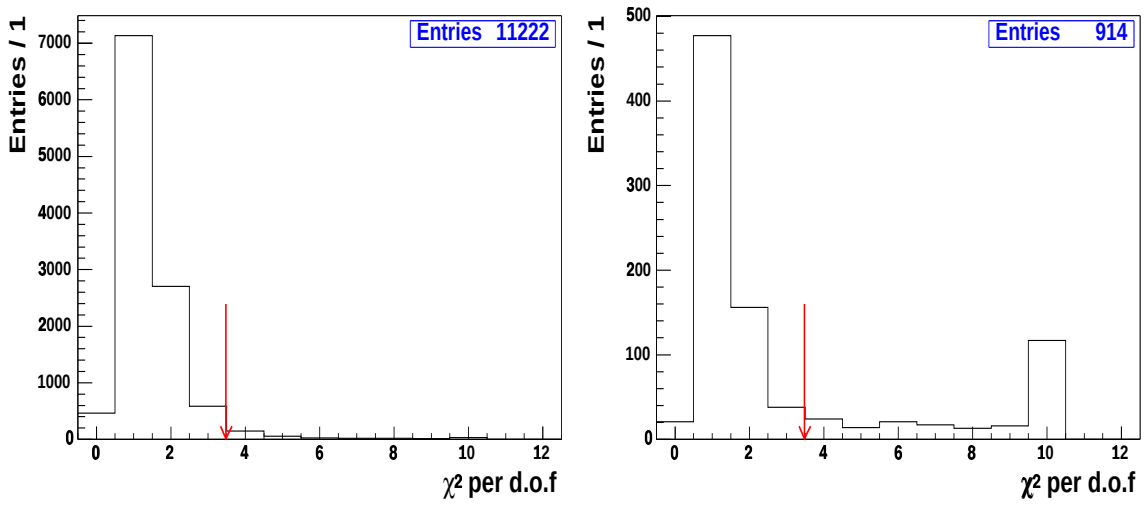

(a) (b)

Figure 6.26: **Loose muon efficiency study:** *Distribution of test muon track χ^2 per degree of freedom after all other cuts have been applied. Those cases in which (a) the test track is matched to a loose muon and (b) the test track is not matched to a loose muon. The red arrows indicate the position of the cut.*

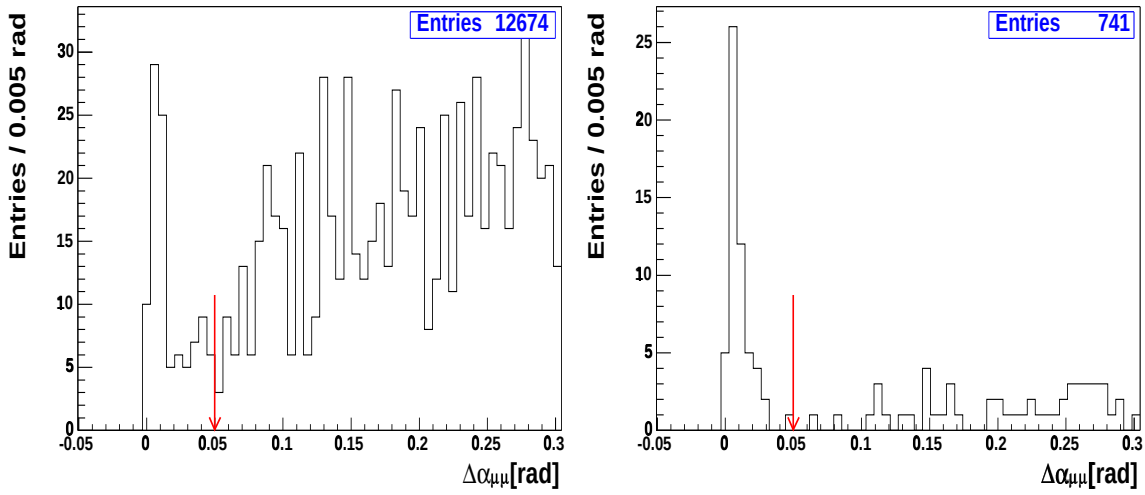

(a) (b)

Figure 6.27: **Loose muon efficiency study:** *Distribution of $\Delta\alpha_{\mu\mu}$ after all other cuts have been applied. Those cases in which (a) the test track is matched to a loose muon and (b) the test track is not matched to a loose muon. The red arrows indicate the position of the cut.*

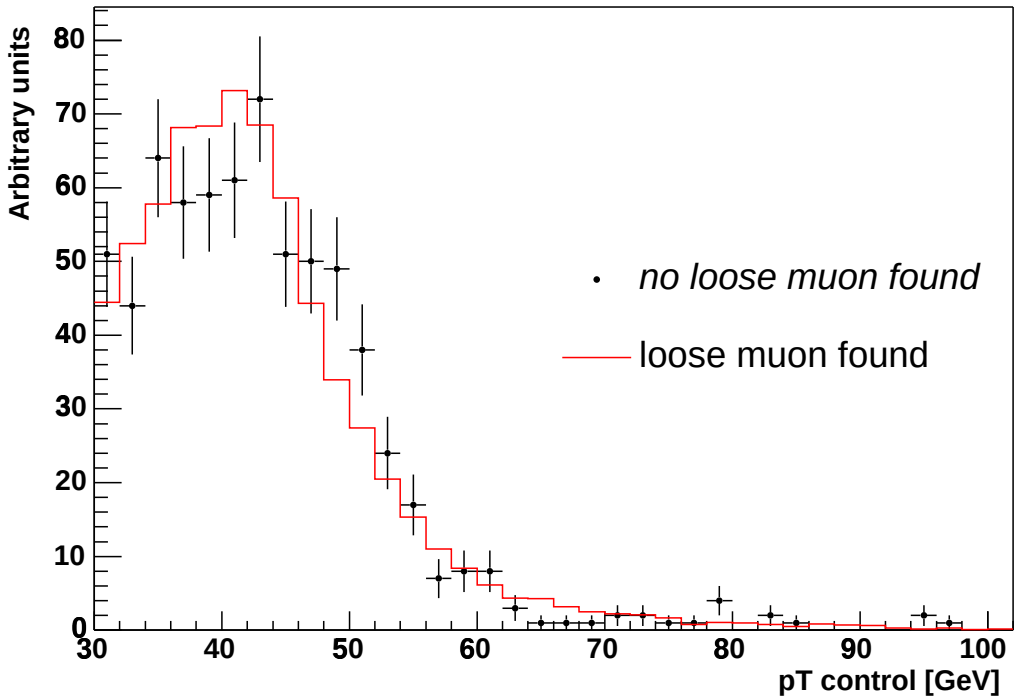

Figure 6.28: **Loose muon efficiency study:** *Distribution of control muon p_T. Red histogram shows those events in which the test track is matched to a loose muon. Points with error bars show those events in which the test track is not matched to a loose muon. The histograms are normalised to the same number of events.*

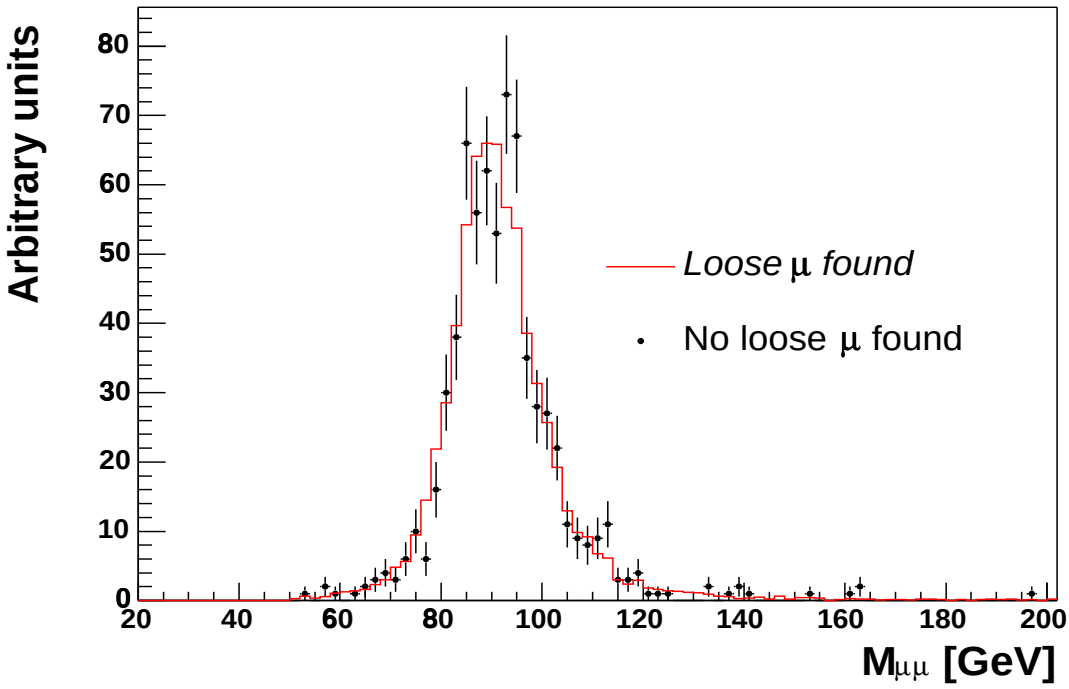

Figure 6.29: **Loose muon efficiency study:** *Distribution of $M_{\mu\mu}$. Red histogram shows those events in which the test track is matched to a loose muon. Points with error bars show those events in which the test track is not matched to a loose muon. The histograms are normalised to the same number of events.*

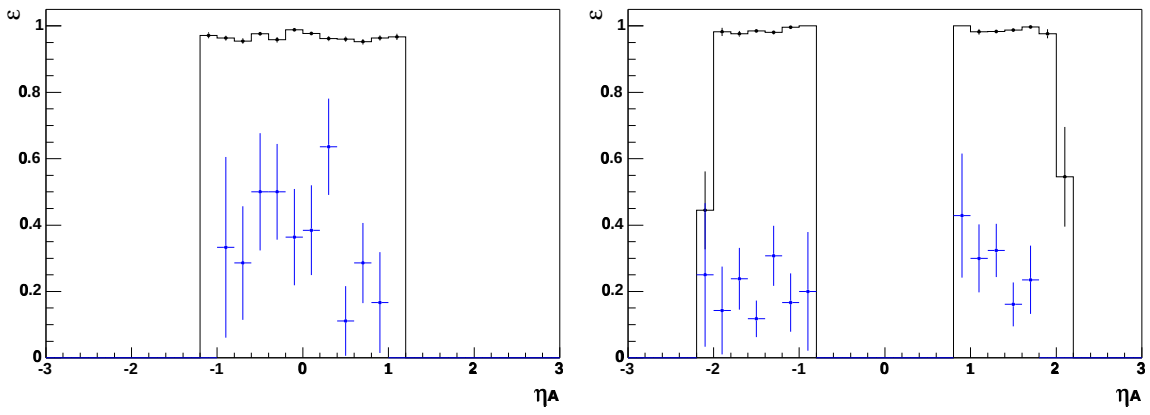

(a) (b)

Figure 6.30: *The efficiency for a muon to be reconstructed as loose as a function of η_A in (a) the central region and (b) the forward region. The black histograms show muons that are outside the boundary region and the blue points show muons that are inside the boundary region.*

6.5 Measurement of Trigger Efficiencies

There are a number of different triggers used to select candidate events, the details of which are given in Appendix C. The basic outcome is that it is only necessary to calculate the efficiency for one di-muon trigger (2MU_A_L2M0) and one single muon trigger (MUW_W_L2M3_TRK10).

2MU_A_L2M0 requires two Level 1 muon objects that have satisfied the tight scintillator condition. It also requires one medium muon at Level 2, with no p_T cut. MUW_W_L2M3_TRK10 requires one Level 1 muon object that satisfies both the tight scintillator and loose wire conditions in the region $|\eta_A| < 1.5$. At Level 2 it requires a medium muon that has $p_T > 3$ GeV. At Level 3 a track trigger object with $p_T > 10$ GeV is required. During period 1 the muon triggers required the Level 1 fast-z condition to be satisfied; after this time the condition was removed.

The efficiencies for candidate events to be selected by the 2MU_A_L2M0 and MUW_W_L2M3_TRK10 triggers are found by measuring each of the components of the triggers in turn. Those components relevant to the single muon trigger only are measured using the data in period 2 only. The trigger component efficiencies that need to be measured are:

1. Level 1 tight scintillator with respect to a loose offline muon, $\varepsilon_{\mathrm{L1scint}}$ [section 6.5.1].

2. Level 1 loose wire in the region $|\eta_A| < 1.5$ with respect to a loose offline muon that satisfies the Level 1 tight scintillator requirements, $\varepsilon_{\mathrm{L1wire}}$ [section 6.5.2].

3. Level 2 medium muon with respect to a loose offline muon that satisfies the Level 1 tight scintillator requirements, $\varepsilon_{\mathrm{L2M0}}$ [section 6.5.3].

4. Level 2 medium muon, $p_T > 3$ GeV with respect to a loose offline muon that (a) satisfies both the Level 1 tight scintillator and loose wire conditions, $\varepsilon_{\mathrm{L2M3}}$ and (b) that does not satisfy the Level 1 tight scintillator and loose wire conditions, $\varepsilon^{*}_{\mathrm{L2M3}}$ [section 6.5.3].

5. Level 3 track trigger, $p_T > 10$ GeV with respect to an offline central track with $p_T > 15$ GeV, $\varepsilon_{\mathrm{L3track}}$ [section 6.5.4].

6. Level 1 fast-z condition, $\varepsilon_{\mathrm{fz}}$ [section 6.5.5].

All of the muon detector trigger components (1-4) are measured using candidate events that have passed all selection criteria other than the trigger requirement. One of the muons in the event acts as a control muon and is required to have fired one of the single muon triggers that the control muon fires in section 6.4. It is then asked if the other muon, the test muon, is associated with the trigger component in question. This procedure is repeated with the second muon acting as the control muon and the first acting as the test muon.

6.5.1 Level 1 Tight Scintillator Efficiency

The efficiency for a muon to satisfy the Level 1 tight scintillator condition is given as a function of η_A and ϕ_A of the test muon in Figures 6.31(a) and 6.31(b) respectively.[9] Due to the wealth of structure in both coordinates, $\varepsilon_{\mathrm{L1scint}}$ is introduced into PMCS as two separate one-dimensional projections in η_A and ϕ_A, for the central and forward muon systems separately. So that the efficiency is not double counted, the ϕ_A distribution is normalised to unity.

An approximation to the average value of the efficiency is found by dividing the number of events in the efficient sample by the total number of events. A value of

$$\varepsilon_{\mathrm{L1scint}} = 0.858 \pm 0.002 \tag{6.17}$$

is obtained.

Figure 6.32 shows the distribution of $\mathrm{M}_{\mu\mu}$ for the events in which a tight scintillator object was found and for events in which no object was found. The histograms have been normalised to the same number of events. The distribution for inefficient events appears to have slightly more events in the low mass region. This may be due to any residual background in the candidate events being concentrated in this inefficient sample. In order to take this possibility into account the efficiency is also calculated by introducing a mass cut at 70 GeV. This leads to a 0.5% difference in the acceptance which is added as a systematic uncertainty.

[9] The apparent increase in the efficiency in the region $4.25 < \phi_A < 5.15$ is due to the fact that the exclusion of the bottom hole forces muons with this ϕ_A value to be at high $|\eta_A|$ where the efficiency is high.

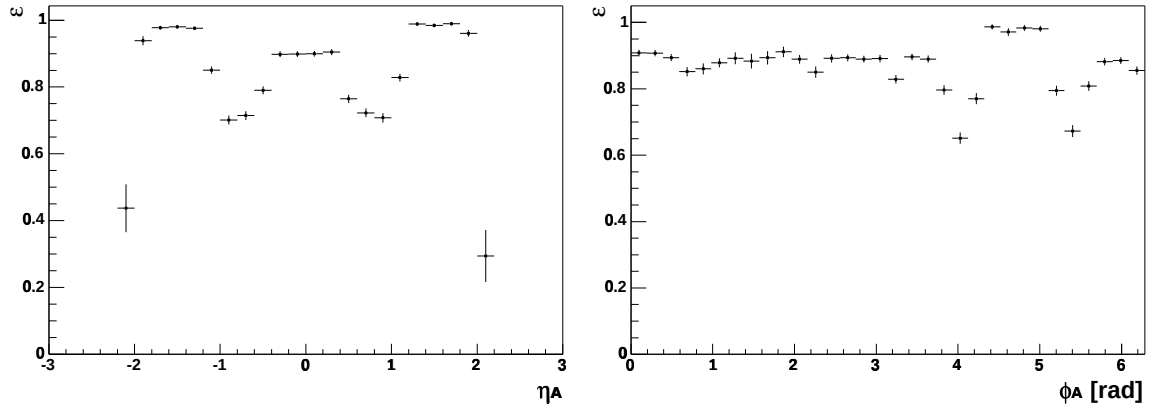

(a) (b)

Figure 6.31: *Level 1 tight scintillator efficiency with respect to a loose offline muon as a function of (a) η_A and (b) ϕ_A.*

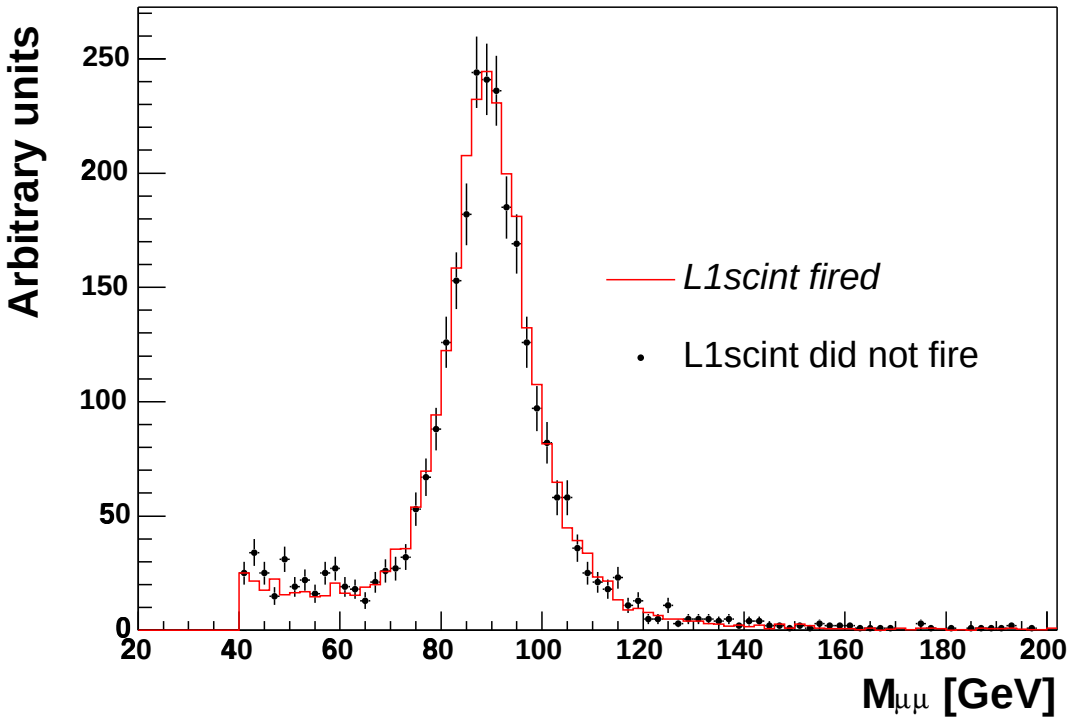

Figure 6.32: *$M_{\mu\mu}$ for the Level 1 scintillator study. Red histogram shows those events where the tight scintillator condition was satisfied. Points with error bars shows those events where the tight scintillator condition was not satisfied.*

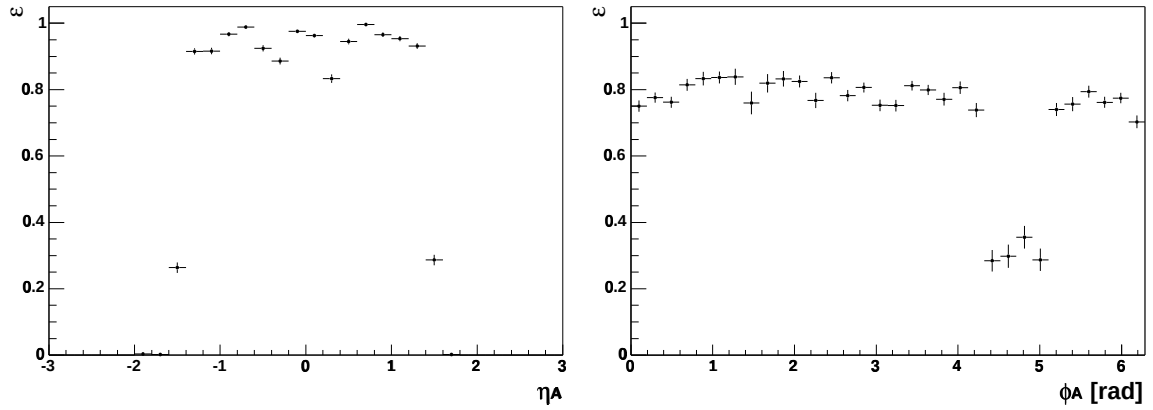

(a) (b)

Figure 6.33: *The efficiency for a muon to fire the Level 1 loose wire trigger in the region* $|\eta_A| < 1.5$ *with respect to a loose offline muon that has satisfied the Level 1 scintillator condition in period 2, as a function of (a)* η_A *and (b)* ϕ_A.

6.5.2 Level 1 Loose Wire Efficiency

The next step is to measure the efficiency of the Level 1 loose wire condition for muons that are reconstructed as loose offline and that satisfy the Level 1 tight scintillator requirements. $\varepsilon_{\mathrm{L1wire}}$ is given as a function of η_A and ϕ_A of the test muon in Figures 6.33(a) and 6.33(b) respectively. An approximation to the average value of the Level 1 wire trigger is found by dividing the number of events in the efficient sample by the total number of events. A value of

$$\varepsilon_{\mathrm{L1wire}} = 0.749 \pm 0.003 \tag{6.18}$$

is obtained.

6.5.3 Level 2 Trigger Efficiency

The next step is to measure the Level 2 trigger efficiencies $\varepsilon_{\mathrm{L2M0}}$, $\varepsilon_{\mathrm{L2M3}}$ and $\varepsilon^{*}_{\mathrm{L2M3}}$. A substantial increase in the Level 2 efficiency due to changes in the Level 2 look-up tables makes it necessary to determine the efficiency for period 1 and period 2 separately.[10] Table 6.1 shows the average Level 2 efficiencies for the two periods.

[10]For the purposes of calculating the cross section, all of the efficiencies are measured separately for the two periods.

	$\varepsilon_{\mathrm{L2M0}}$	$\varepsilon_{\mathrm{L2M3}}$	$\varepsilon^{*}_{\mathrm{L2M3}}$
Period 1	0.85 ± 0.01	not used	not used
Period 2	0.931 ± 0.002	0.971 ± 0.001	0.63 ± 0.01

Table 6.1: *The average Level 2 efficiencies in period 1 and period 2.*

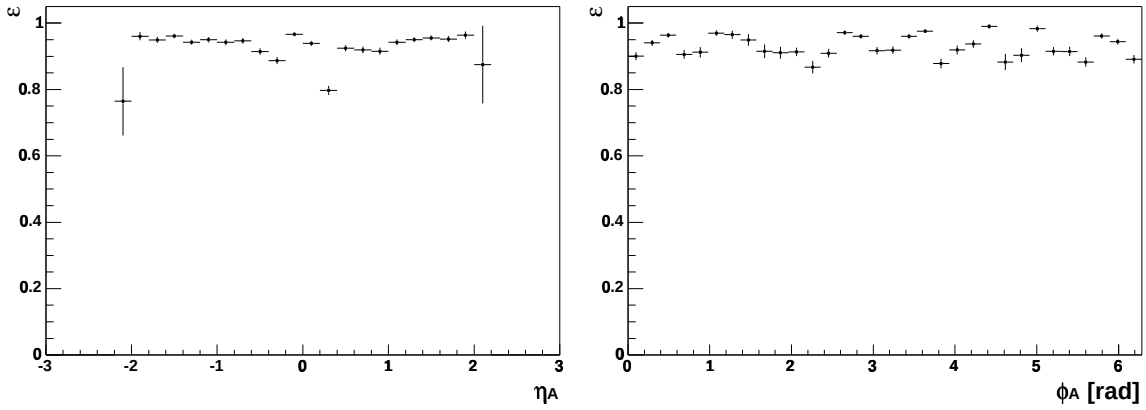

(a) (b)

Figure 6.34: *The Level 2 medium muon trigger efficiency with respect to a loose offline muon that has satisfied the Level 1 tight scintillator condition in period 2, as a function of (a) η_A and (b) ϕ_A.*

$\varepsilon_{\mathrm{L2M0}}$ is shown for period 2 as a function of η_A and ϕ_A in Figures 6.34(a) and 6.34(b) respectively. $\varepsilon_{\mathrm{L2M3}}$ is shown as a function of η_A and ϕ_A for period 2 in Figures 6.35(a) and 6.35(b) respectively.

6.5.4 Level 3 Track Trigger Efficiency

The efficiency of the Level 3 Track Trigger is measured using candidate events that were accepted by one of the di-muon triggers: 2MU_A_L2M0, 2MU_A_L2ETAPHI or 2MU_A_L2M0_L3L(6,15). For each track in the event it is simply asked if a Level 3 track object is matched to it. The matching is done in ϕ only since some Level 3 tracks only have axial hits. The efficiency is plotted as a function of η_{CFT} and ϕ [11] in Figures 6.36(a) and 6.36(b) respectively.

[11] The apparent dip in the efficiency for $4.25 < \phi < 5.15$ is due to the fact that the exclusion of the bottom hole forces muons with this ϕ value to be at high $|\eta|$ where the efficiency is low.

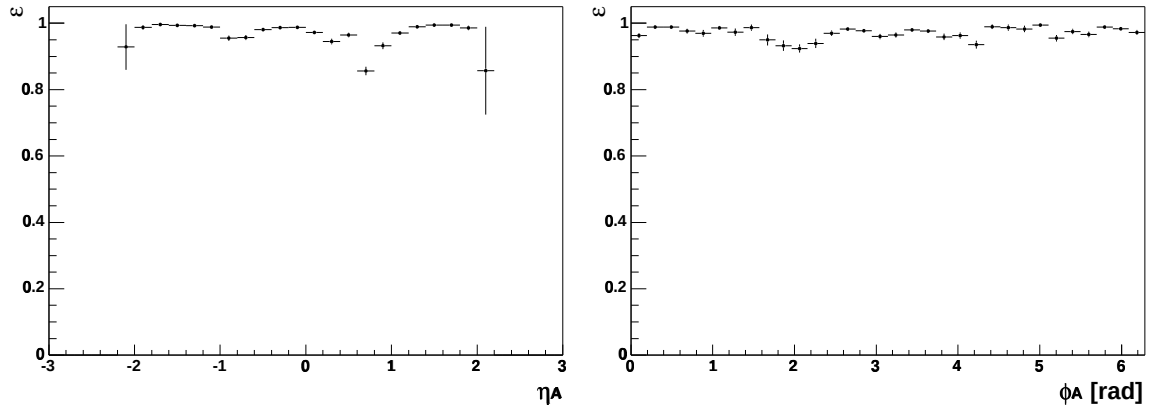

(a) (b)

Figure 6.35: *The Level 2 medium muon, $p_T > 3$ GeV, trigger efficiency with respect to a loose offline muon that has satisfied the Level 1 tight scintillator and loose wire conditions in period 2, as a function of (a) η_A and (b) ϕ_A.*

From the numbers of muons in the efficient and inefficient subsamples an average value for the Level 3 tracking efficiency of

$$\varepsilon_{\mathrm{L3track}} = 0.789 \pm 0.003 \tag{6.19}$$

is found.

6.5.5 Level 1 Fast-z Efficiency

The efficiency of $\varepsilon_{\mathrm{fz}}$ for period 1 is measured using $\mathrm{Z}/\gamma^* \to e^+e^-$ events [25], collected in that period, since the electromagnetic triggers have no fast-z requirement. The efficiency is given by the fraction of candidate $\mathrm{Z}/\gamma^* \to e^+e^-$ events for which the fast-z requirement was satisfied. The result

$$\varepsilon_{\mathrm{fz}} = 0.943 \pm 0.004 \tag{6.20}$$

is obtained. In order to check that the efficiency of $\varepsilon_{\mathrm{fz}}$ is the same in $\mathrm{Z}/\gamma^* \to \mu^+\mu^-$ events as it is in $\mathrm{Z}/\gamma^* \to e^+e^-$ events, despite differences in the kinematic distributions of the selected events, its value is calculated using both $\mathrm{Z}/\gamma^* \to \mu^+\mu^-$ and $\mathrm{Z}/\gamma^* \to e^+e^-$ events in period 2, when the muon triggers had no fast-z requirement. The numbers are found to be in good agreement. A systematic uncertainty of 0.3%

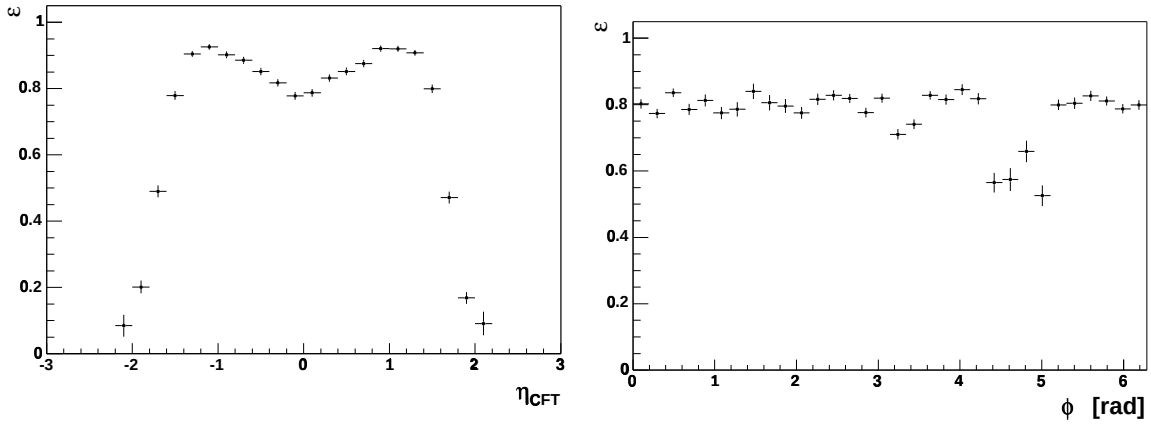

(a) (b)

Figure 6.36: *Efficiency of a Level 3 track object with $p_T > 10$ GeV with respect to an offline track with $p_T > 15$ GeV, measured in period 2, as a function of (a) η_{CFT} and (b) ϕ.*

due to the statistical limitation of this check is added to $\varepsilon_{\rm fz}$. In period 2 this requirement was not made and for the purposes of calculating the acceptance $\varepsilon_{\rm fz}$ is set trivially to unity.

6.6 Evaluation of Total Efficiency

6.6.1 Splitting of Dataset

Periods 1 and 2 have been treated separately by measuring the efficiencies independently. There are a few runs in period 2, with a total integrated luminosity of 1.5 pb^{-1}, where the single muon trigger is prescaled and so cannot be used. For the purposes of evaluating the cross section these runs are treated separately. The subdivision of the latter data taking period where the single muon trigger is prescaled is denoted period 2a and that where it is not prescaled is denoted period 2b.

6.6.2 Total Efficiency Using PMCS

All of the work described in this and consequent sections involving PMCS was done by Paul Telford. Work described involving the data or DMCS was done by the author.

The total efficiency for selecting $Z/\gamma^* \to \mu^+\mu^-$ events with $M_{\mu\mu} > 40$ GeV, $\varepsilon_{Z\gamma*}$, is evaluated according to the following formula:

$$\varepsilon_{Z\gamma*} = \varepsilon_{MC}^{eff} \times \varepsilon_{fz} \times \varepsilon_{opposite\_q} \times \varepsilon_{isol} \times \varepsilon_{cosmic}. \quad (6.21)$$

$\varepsilon_{opposite\_q}$, ε_{isol} and ε_{cosmic} were described in section 6.2 and ε_{fz} in section 6.5.5. ε_{MC}^{eff} includes the geometrical acceptance of the muon detector, the efficiency of the kinematic cuts on p_T and $M_{\mu\mu}$ and the trigger, tracking and loose muon identification efficiencies. It is determined using PMCS with the CTEQ6M [26] PDF set and tunes of PYTHIA parameters taken from [27, 28].

To evaluate ε_{MC}^{eff}, a sample of $Z/\gamma^* \to \mu^+\mu^-$ is produced with a generator level mass cut of 30 GeV. This lower mass cut is to account for those events with a physical invariant mass less than 40 GeV, but which are measured to have a mass greater than 40 GeV and so are included in the acceptance. ε_{MC}^{eff} is defined to be the ratio between the number of events accepted to the number of events generated with a mass greater than 40 GeV. An event is accepted if:

- both muons are inside the geometrical acceptance of the muon chambers,
- both muons pass the kinematic cuts on p_T and $M_{\mu\mu}$,
- both muons are reconstructed in the central detectors,
- both muons are reconstructed as loose in the muon chambers and
- the components of the di-muon trigger are satisfied (periods 1 and 2a); the components of either the di-muon or single muon trigger are satisfied (period 2b).

The dependence on the detector geometry of the efficiencies for the central tracking, loose muon identification and trigger efficiencies are introduced into PMCS; a muon is accepted with a probability equal to the efficiency at its detector coordinates. The exact coordinates used to measure efficiencies are chosen so that the measurements are unbiased. Table 6.2 summarises these choices. The introduction of the efficiencies into PMCS is described in detail in [29]. Table 6.3 lists the values of ε_{MC}^{eff} obtained for the three periods.

6.6.3 Assessment of Uncertainties on ε_{MC}^{eff}

This section describes the assessment of uncertainties on ε_{MC}^{eff}. The uncertainty due to Monte Carlo statistics is negligible as 5 million events were used.

EFFICIENCY	COORDINATES
$\varepsilon_{\text{track}}$	η_{CFT}, z
$\varepsilon_{\text{L3track}}$	η_{CFT}
$\varepsilon_{\text{loose}}$	η_A, in/out of octant boundaries
$\varepsilon_{\text{L1scint}}$	η_A and ϕ_A projections
$\varepsilon_{\text{L1wire}}$ (central region)	η_A and ϕ_A projections
$\varepsilon_{\text{L1wire}}$ (forward region)	η_A: in/out of octant boundaries
ε_{L2} (central region)	η_A and ϕ_A projections
ε_{L2} (forward region)	η_A: in/out of octant boundaries

Table 6.2: *Coordinates used to input efficiencies into PMCS. All muon efficiencies are input separately for the central and forward muon systems.* ε_{L2} *denotes all Level 2 efficiencies.*

Period	$\int \mathcal{L}dt$ [pb^{-1}]	$\varepsilon_{\text{MC}}^{\text{eff}}$
1	36.8	0.239
2a	1.5	0.268
2b	109.4	0.322

Table 6.3: *Variation of* $\varepsilon_{\text{MC}}^{\text{eff}}$ *in the three data-taking periods.*

Statistical Uncertainties of Input Efficiencies

There is an uncertainty on $\varepsilon_{\rm MC}^{\rm eff}$ due to the statistical uncertainties of the efficiencies measured in data. The value of each efficiency in each bin is varied independently when introduced into PMCS with a Gaussian distribution with sigma equal to the size of the uncertainty on that bin. This is done 100 times and the uncertainty is given by the standard deviation of the $\varepsilon_{\rm MC}^{\rm eff}$ values obtained. The uncertainties are 2.5%, 0.9% and 0.6% for periods 1, 2a and 2b respectively.

Muon Detector Boundary Variation

The loose muon identification, Level 1 wire and Level 2 trigger efficiencies are all evaluated in two different regions: close to the octant boundary and away from the octant boundary. However, there is some ambiguity in the choice of the boundary position. A systematic uncertainty is evaluated by varying the size of the boundary by 50% which results in a 1.0% variation in the acceptance.

$\varepsilon_{\rm L1scint}$ as a Two-Dimensional Map

The Level 1 tight scintillator efficiency is input as separate functions of η_A and ϕ_A, due to the wealth of structure in both coordinates. In order to cross check this procedure the η_A and ϕ_A dependences were included as a two-dimensional map. The χ^2 of the comparison of the η_A distribution between data and PMCS is higher when this method is used, probably due to the limited statistics at high $|\eta_A|$. The 0.2% difference in the total acceptance is quoted as a systematic uncertainty.

Variation of Efficiencies With Time

All measured efficiencies are averaged separately over period 1 and period 2. They are, however, not perfectly constant within these two periods. The procedure used to determine the uncertainty due to this variation is to evaluate the tracking efficiency, loose muon identification efficiency and cross section in blocks of runs, each containing ~ 5 pb^{-1}, as shown in Figures 6.37(a), 6.37(b) and 6.37(c) respectively. The large gap coincides with the splitting of the periods. The cross section is evaluated in each bin (with only the number of events, luminosity, tracking efficiency and loose muon identification efficiency varying) and added together, weighted by the luminosity in

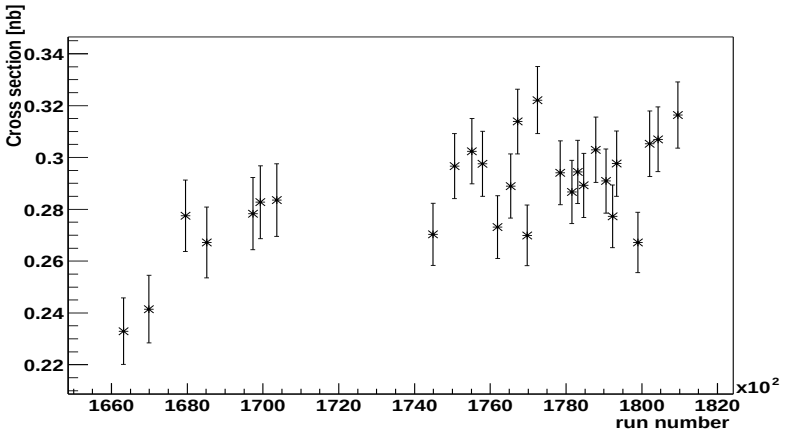

(a)

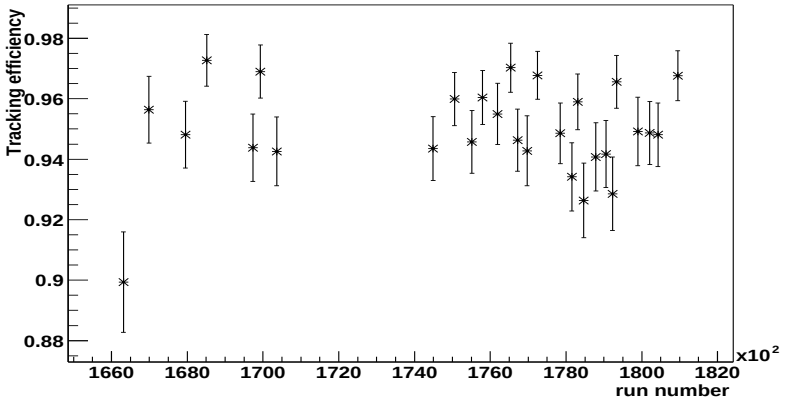

(b)

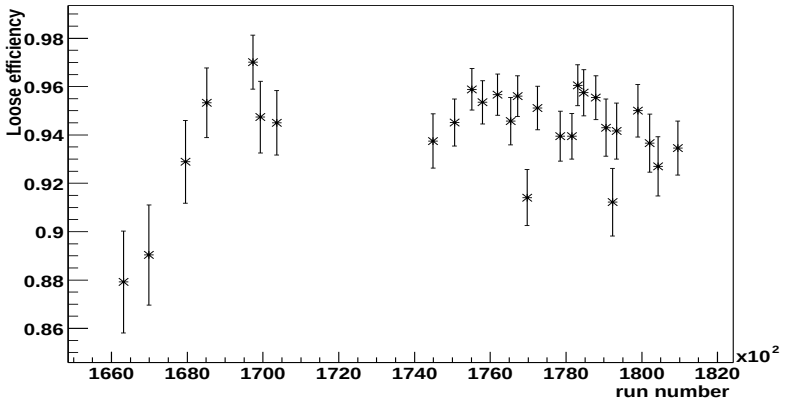

(c)

Figure 6.37: *Stability of the cross section as a function of time. (a) Cross section in blocks of* $\sim 5\ pb^{-1}$. *(b) Tracking efficiency in blocks of* $\sim 5\ pb^{-1}$. *(c) Loose muon efficiency in blocks of* $\sim 5\ pb^{-1}$.

each bin. Using the re-weighted cross section gives a 0.05% alteration in the total cross section which is treated as negligible.

z Distribution of Beamspot

The distribution of the beamspot in the z direction is not precisely known. For the purpose of this analysis the modelling of the distribution is based on a Gaussian distribution. This is tuned [30] using $W \to \mu\nu$ events to have a width of 26.7 cm. However, it was found impossible to obtain good agreement at high $|z|$ between the data and PMCS using a single Gaussian alone in both $W \to \mu\nu$ and $Z/\gamma^* \to \mu^+\mu^-$ events. Plotting the ratio of data and PMCS as a function of z a clear linear increase is observed. In the region $|z| > 40$ cm the ratio of data to PMCS is fitted with a first order polynomial. PMCS is then re-weighted by this linearly increasing factor.

To assess a systematic uncertainty the acceptance is calculated using the tune performed using $W \to e\nu$ and $Z/\gamma^* \to e^+e^-$ events [31]: a 28 cm Gaussian with no linear factor. This gave an acceptance which was 0.6% lower. This difference is quoted as a systematic uncertainty. Figure 6.38 shows the distribution of the z position of the muon tracks for the candidate events. The data are shown as points with error bars compared with the PMCS prediction using the 26.7 cm Gaussian with the linear factor for the beamspot distribution (black histogram) and that using the 28 cm Gaussian input for the beamspot distribution (blue histogram).

p_T Resolution and Scale

The parameterisation of the momentum resolution of the DØ central tracking system was given in section 3.4. The uncertainty of this parameterisation is given in [8]. The uncertainty on the acceptance due to the uncertainty on the p_T smearing factor is negligible. The uncertainty in the acceptance due to knowledge of the p_T scale is found to be 0.1%.

PDFs

The effect on $\varepsilon_{\mathrm{MC}}^{\mathrm{eff}}$ of varying the choice of PDF was investigated using the CTEQ6 [26] error sets. A description of the determination of the uncertainty on the PDFs is given in [29]. The uncertainty in $\varepsilon_{\mathrm{MC}}^{\mathrm{eff}}$ due to the choice of PDF is found to be 1.7%.

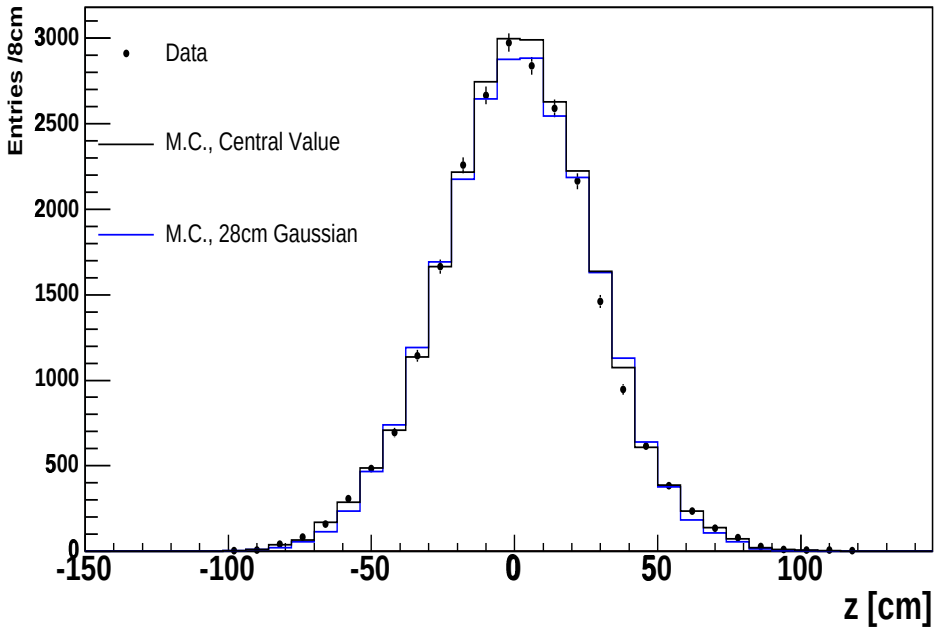

Figure 6.38: *Distribution of the z position of the muon tracks for the candidate events. The data are shown as points with error bars compared with the PMCS prediction using a 26.7 cm Gaussian with a linear factor as input for the beamspot position (black histogram) and that using a 28 cm Gaussian as input for the beamspot position (blue histogram).*

$\varepsilon_{\mathrm{MC}}^{\mathrm{eff}}$ Using DMCS

The value of $\varepsilon_{\mathrm{MC}}^{\mathrm{eff}}$ measured using PMCS can be broken down into four parts:

1. Geometric acceptance of the muon detectors and kinematic cuts.
2. Offline central track identification.
3. Offline loose muon identification.
4. Trigger efficiency.

The first three can be cross checked using a $\mathrm{Z}/\gamma^* \to \mu^+\mu^-$ DMCS sample. Monte Carlo samples with a mass range of $60 < \mathrm{M}_{\mu\mu} < 130$ GeV and the CTEQ4L [32] PDF set are used for both PMCS and DMCS for the purpose of this comparison. The efficiency for a muon to be reconstructed both in the central and in the muon detectors is greater in DMCS than it is in the data due to inaccurate detector simulation. If the average efficiencies predicted by DMCS are scaled so that they agree with those measured in the data, it is possible to cross check the efficiency to reconstruct offline $\mathrm{Z}/\gamma^* \to \mu^+\mu^-$ events.

Table 6.4 shows the breakdown of $\varepsilon_{\mathrm{MC}}^{\mathrm{eff}}$ measured with PMCS and DMCS. The geometrical acceptance and kinematic cut efficiencies are equivalent within their statistical uncertainties. There is a difference of 0.9% between the efficiencies for reconstructing two central tracks. There is a difference of 0.6% between the efficiencies for reconstructing two loose muons. These may be due to the poor description of the angular dependence of DMCS, which is not corrected to the data. They may also be due to some correlation that is not treated properly in PMCS. The overall discrepancy of 1.1% is taken as a systematic uncertainty.

All uncertainties on $\varepsilon_{\mathrm{MC}}^{\mathrm{eff}}$ mentioned in this and any earlier sections that are considered to be constant throughout the three periods (which excludes the uncertainties due to statistical uncertainties on the input efficiencies) are summarised in Table 6.5.

6.6.4 Data - PMCS Comparison Plots

In order to demonstrate that the Monte Carlo simulation provides a realistic description of the data, comparison plots between the data and PMCS are shown. In each

	DMCS	PMCS
Geometrical Acceptance and kinematic cuts	0.471 ± 0.001	0.472 ± 0.001
2 central tracks	0.883 ± 0.001	0.891 ± 0.001
2 loose muons	0.872 ± 0.001	0.877 ± 0.001

Table 6.4: *Breakdown of the acceptance measured using DMCS and PMCS. The numbers are consecutive so that the kinematic efficiency is for those events that passed the geometrical acceptance cuts, etc.*

Uncertainty source	Fractional uncertainty
PDF uncertainty	0.017
Boundary variation	0.010
$\varepsilon_{\mathrm{L1scint}}$ averaging	0.002
$\varepsilon_{\mathrm{L1scint}}$ background	0.005
Muon id background	0.004
z of beamspot	0.006
p_T scale	0.001
PMCS/DMCS discrepancy	0.011
total (exc. PDFs)	0.017

Table 6.5: *Summary of the systematic uncertainties on* $\varepsilon_{\mathrm{MC}}^{\mathrm{eff}}$ *that remain constant through the three periods.*

of the plots the data are shown as points with error bars, PMCS is shown as a blue histogram and the uncertainty on PMCS, due to the statistical uncertainties on the input efficiencies only, is shown as yellow bands.

Figure 6.39 shows the $M_{\mu\mu}$ distribution. The background is shown as a red histogram. Figures 6.40(a) and 6.40(b) show the distribution of η_A for the candidate muons for periods 1 and 2 respectively. Period 2b contains a mixture of events that have been written to tape because they fire:

(1) The single muon trigger only.

(2) The di-muon trigger only.

(3) Both the di-muon trigger and the single muon trigger.

In order to demonstrate that the way the triggers are 'or-ed' together in PMCS describes the actual effect in data, Figures 6.41(a), 6.41(b) and 6.41(c) show the η_A distributions of muons in events that fall into the above categories (1), (2) and (3) respectively (for period 2b only). Figures 6.42(a) and 6.42(b) show the distribution of ϕ_A for the candidate muons in periods 1 and 2 respectively. Figures 6.43(a) and 6.43(b) show the distribution of p_T for the muon with the highest p_T out of the pair and for the muon with the lowest p_T out of the pair respectively for candidate events over the whole data taking period. PMCS describes the data well in the region near the 15 GeV cut on the muon p_T. This helps to justify the assumption in section 6.3 that the inefficiency for muons with a measured $p_T < 15$ GeV is properly taken into account by PMCS. Figure 6.44 shows the p_T distribution of the Z/γ^* for the candidate events in the whole data taking period. Figure 6.45 shows the rapidity distribution of the Z/γ^* for the candidate events in the whole data taking period.

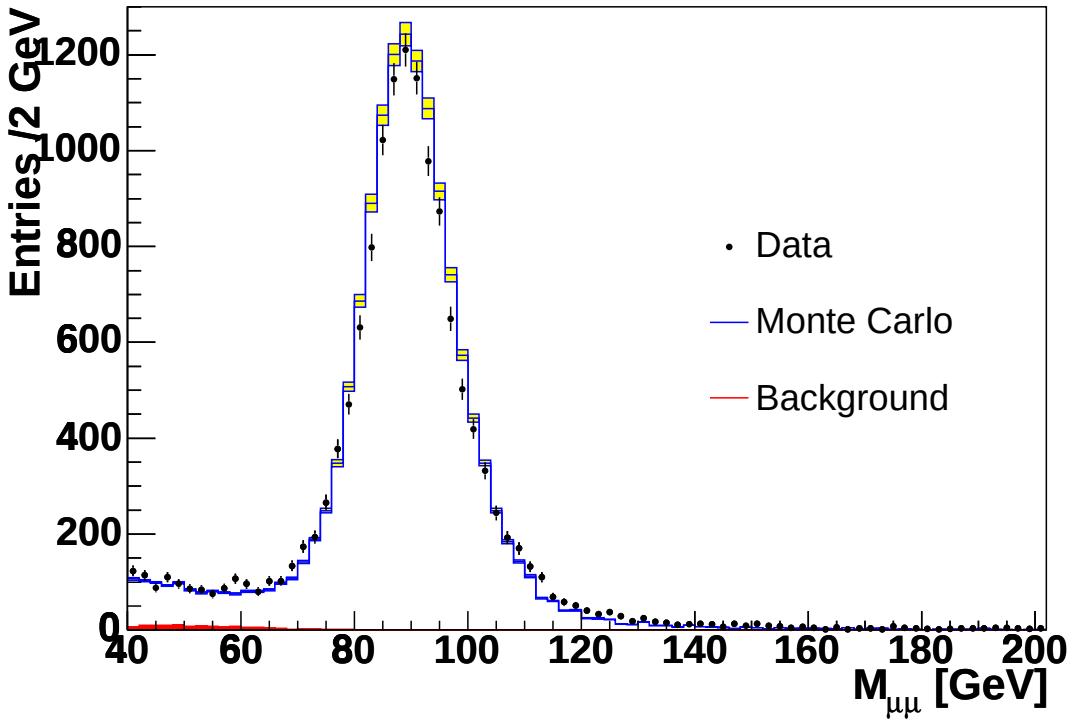

Figure 6.39: *$M_{\mu\mu}$ distribution. The data are shown as points with error bars. The PMCS prediction is shown as a blue histogram with yellow bands for the uncertainty. The contribution from the background is shown as the red filled histogram.*

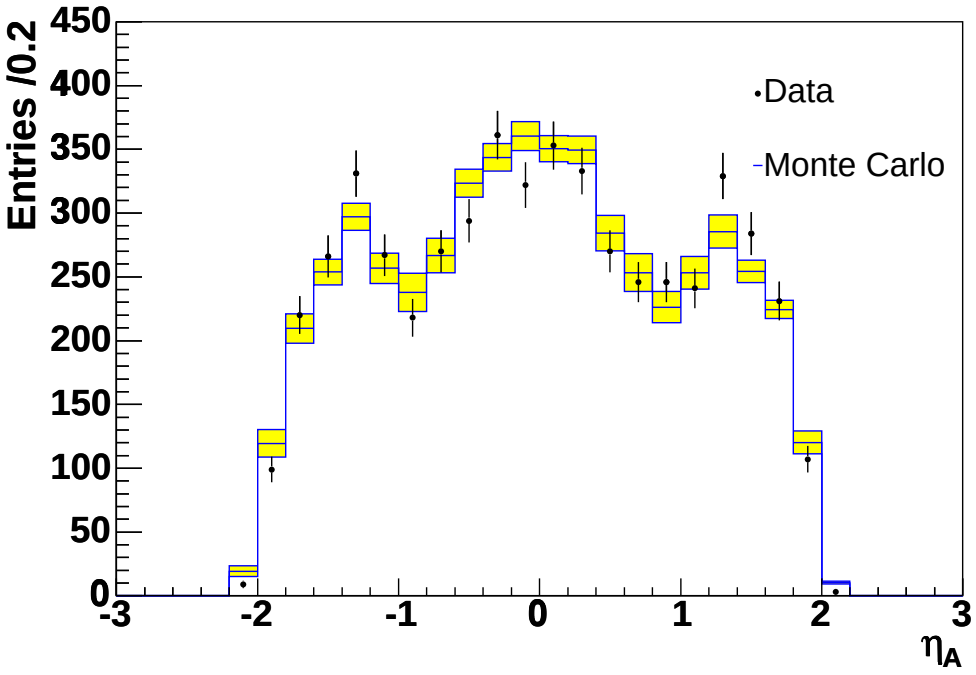

(a)

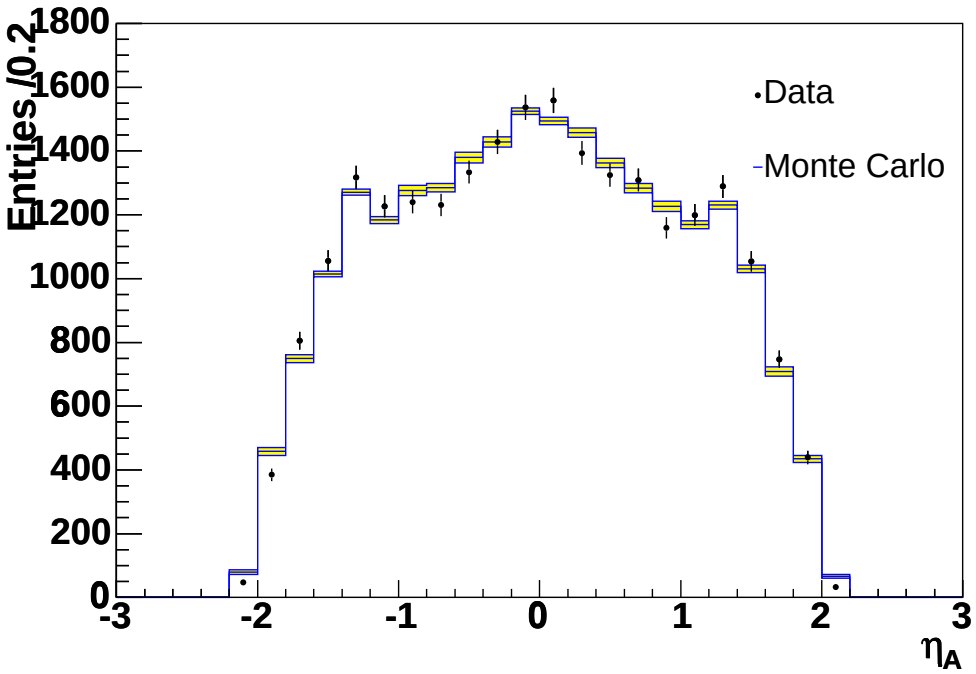

(b)

Figure 6.40: *Muon η_A distribution. The data are shown as points with error bars. The PMCS prediction is shown as a blue histogram with yellow bands for the uncertainty. (a) Period 1. (b) Period 2.*

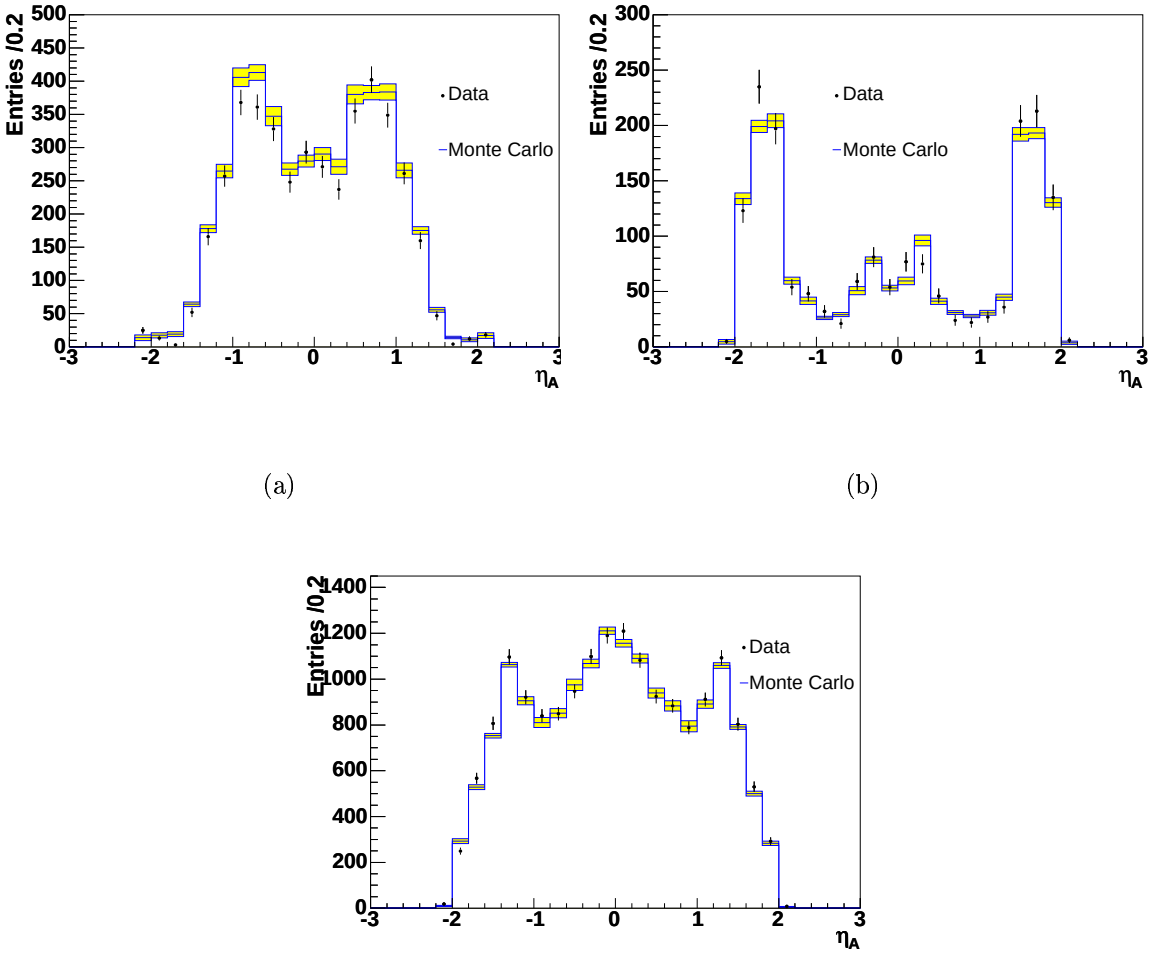

Figure 6.41: *Muon η_A distribution. The data are shown as points with error bars. The PMCS prediction is shown as a blue histogram with yellow bands for the uncertainty. (a) Events that fire only the single muon trigger. (b) Events that fire only the di-muon trigger. (c) Events that fire both the single and di-muon triggers.*

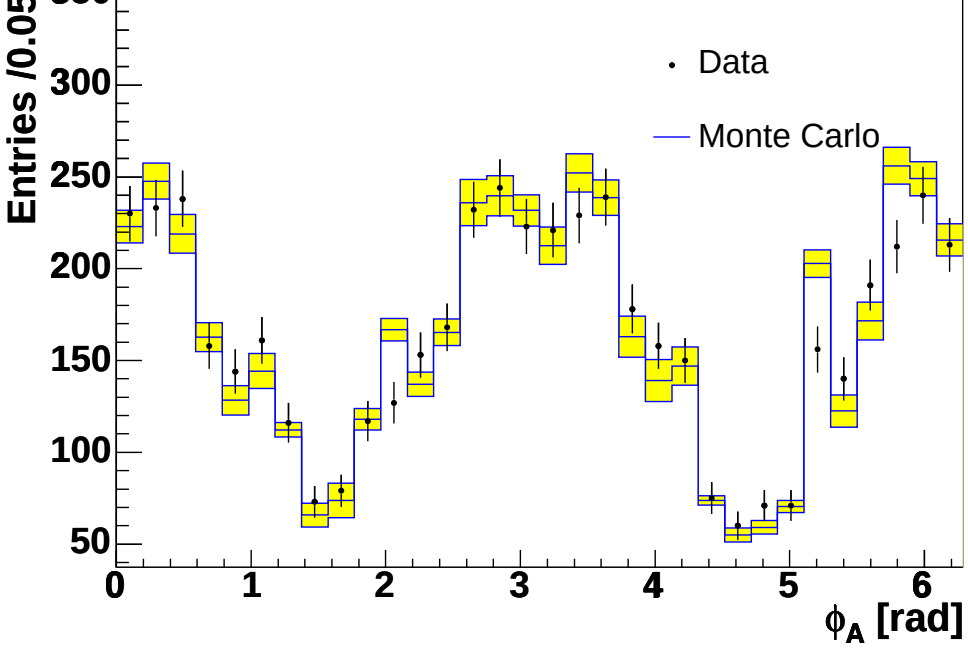

(a)

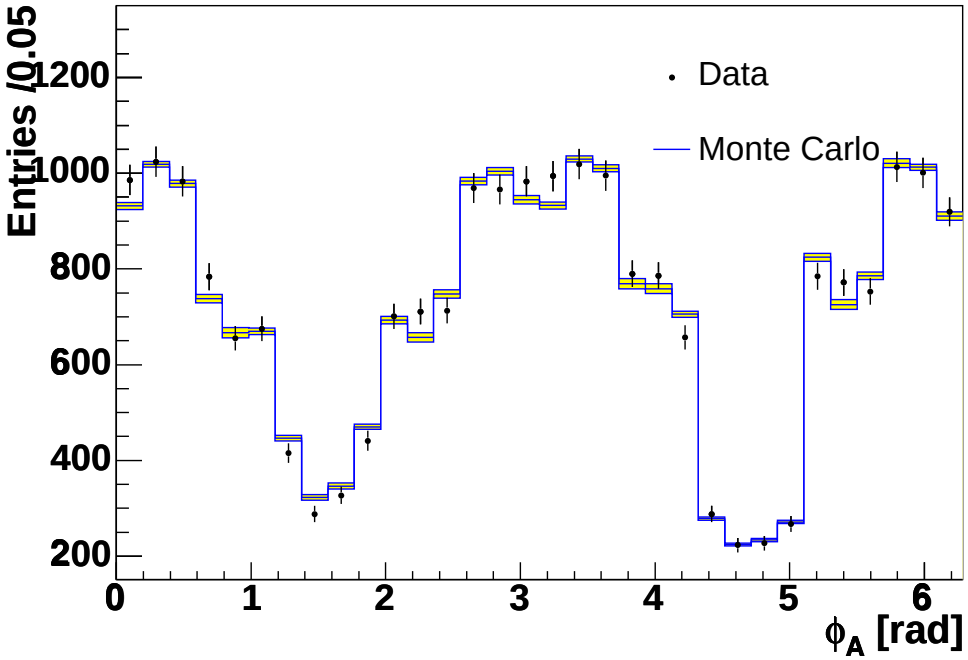

(b)

Figure 6.42: *Muon ϕ_A distribution. The data are shown as points with error bars. The PMCS prediction is shown as a blue histogram with yellow bands for the uncertainty. (a) Period 1. (b) Period 2.*

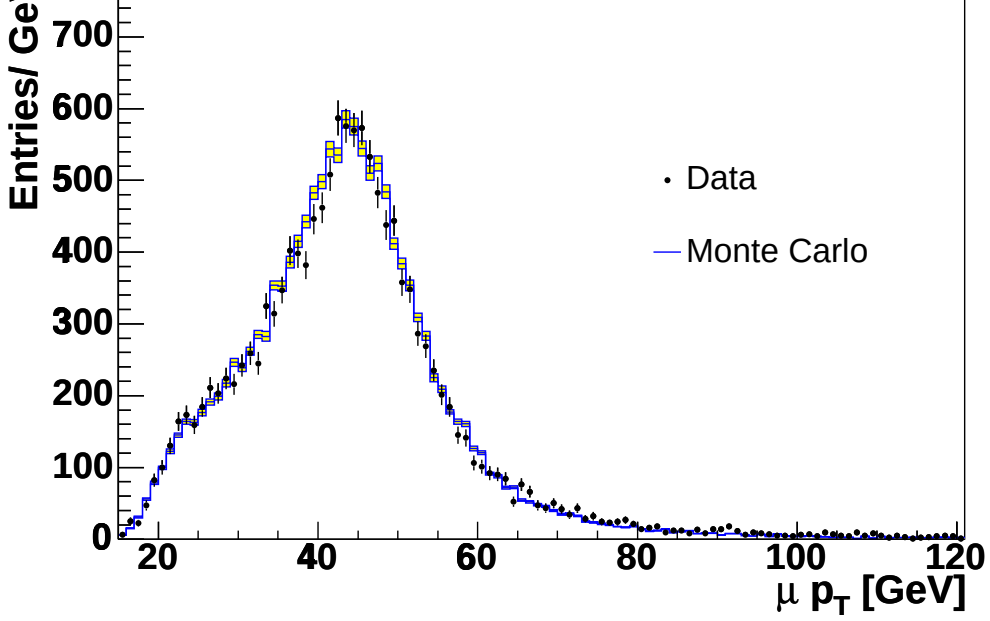

(a)

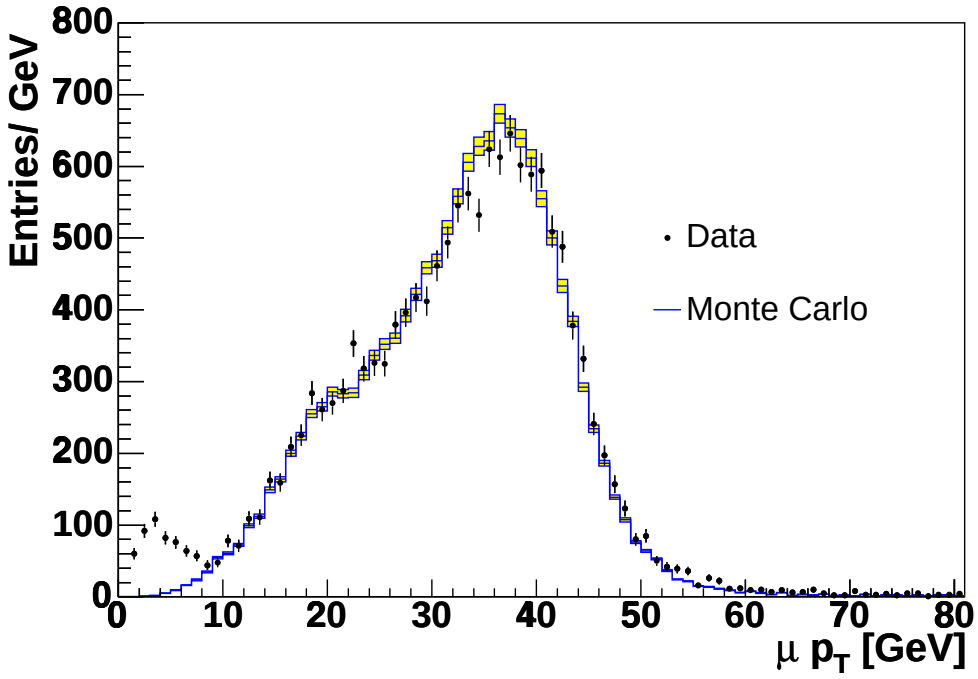

(b)

Figure 6.43: *Muon p_T distribution. The data are shown as points with error bars. The PMCS prediction is shown as a blue histogram with yellow bands for the uncertainty. (a) Higher p_T of the muon pair. (b) Lower p_T of the muon pair when all other cuts other than the cut on this quantity have been applied.*

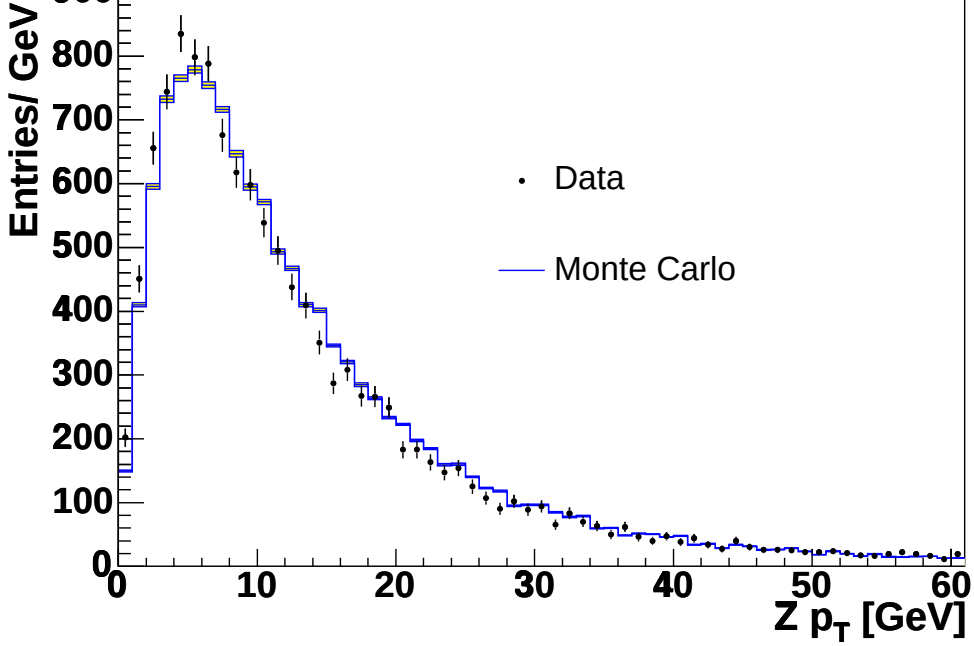

(a)

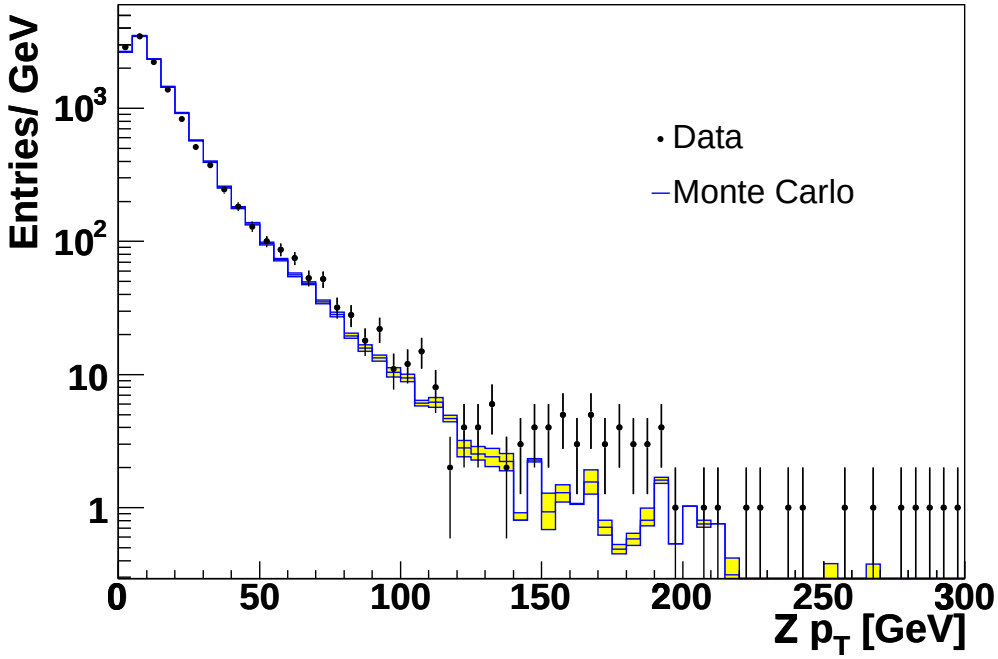

(b)

Figure 6.44: Z/γ^* p_T *distribution. The data are shown as points with error bars. The PMCS prediction is shown as a blue histogram with yellow bands for the uncertainty. (a) Low* p_T *region. (b) Entire region (log scale).*

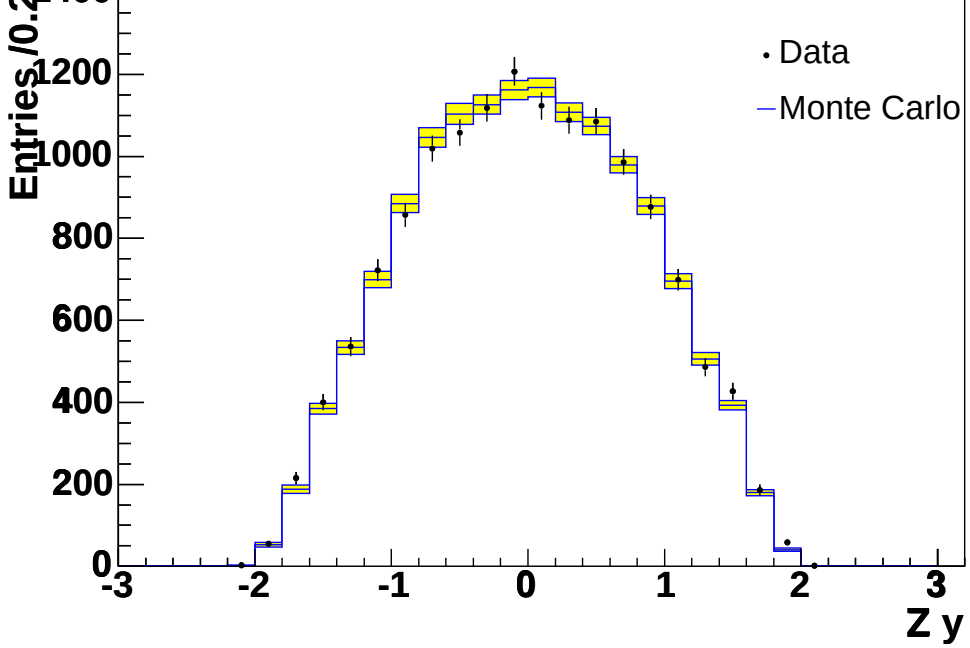

(a)

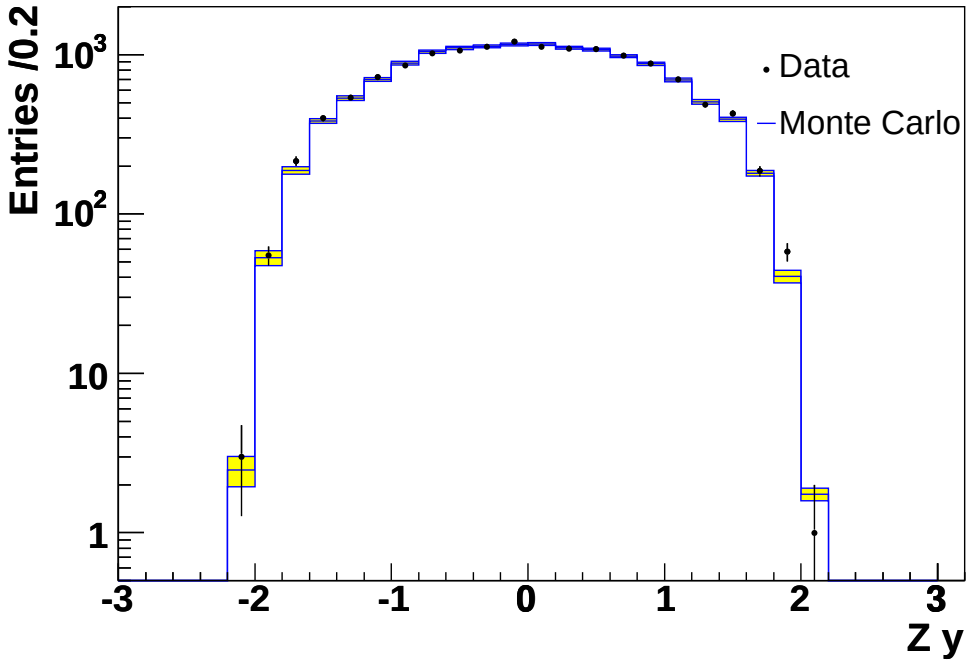

(b)

Figure 6.45: Z/γ^* *rapidity distribution. The data are shown as points with error bars. The PMCS prediction is shown as a blue histogram with yellow bands for the uncertainty. (a) Standard scale. (b) Log scale.*

$\sigma\,(\mathrm{Z}/\gamma^*)$ is found by rewriting Equation 6.1 as:

$$\sigma\,(\mathrm{Z}/\gamma^*) = \frac{\mathrm{N_{cand}}(1 - f_{\mathrm{bb}} - f_{cos})(1 - f_{\tau\tau})(1 - f_{\mathrm{W}})}{\varepsilon^{\mathrm{eff}}_{\mathrm{MC}}\ \varepsilon_{\mathrm{fz}}\ \varepsilon_{\mathrm{opposite\_q}}\ \varepsilon_{\mathrm{isol}}\ \varepsilon_{\mathrm{cosmic}}\ \int \mathcal{L}dt}. \tag{6.22}$$

$\sigma\,(\mathrm{Z})$ is obtained by applying a correcting factor to the above cross section:

$$\sigma\,(\mathrm{Z}) = \sigma\,(\mathrm{Z}/\gamma^*) \times R_\sigma, \tag{6.23}$$

where R_σ is the ratio between the theoretical predictions of $\sigma\,(\mathrm{Z})$ and $\sigma\,(\mathrm{Z}/\gamma^*)$. These cross sections are evaluated using MC@NLO [16].

The value of R_σ has a systematic uncertainty due to the choice of PDF. This uncertainty has some correlation with the PDF uncertainty on $\varepsilon^{\mathrm{eff}}_{\mathrm{MC}}$. To account for this correlation the PDF uncertainty in $\sigma\,(\mathrm{Z})$ is evaluated on the ratio of these quantities. The method used to obtain this uncertainty is given in [29], a value of 1.7% is found.

Table 6.6 summarises the various contributions to the cross section and its uncertainty that remain constant throughout the entire dataset. In this table the PDF uncertainty on both $\varepsilon^{\mathrm{eff}}_{\mathrm{MC}}$ and R_σ is associated with R_σ. Tables 6.7–6.9 summarise

Quantity	Value	fractional uncertainty
$\varepsilon_{\mathrm{isol}}$	0.999 ± 0.001	0.001
$\varepsilon_{\mathrm{opposite\_q}}$	0.998 ± 0.001	0.001
$\varepsilon_{\mathrm{cosmic}}$	0.988 ± 0.006	0.006
f_{bb}	0.005 ± 0.003	0.003
$f_{\tau\tau}$	0.005 ± 0.001	0.001
f_{cos}	0.002 ± 0.002	0.002
f_{W}	0.002 ± 0.001	0.001
R_σ	0.885 ± 0.015	0.017

Table 6.6: *Summary of the components to the calculation of the cross section that remain constant throughout the three data taking periods.*

the contributions to the cross section and its uncertainty that vary between periods, for the three data taking periods: 1, 2a and 2b. The final result for the process

$p\bar{p} \to Z/\gamma^* + X \to \mu^+\mu^- + X$ is measured to be:

$$\sigma\,(Z/\gamma^*) = 327.8 \pm 3.4(\text{stat.}) \pm 8.4(\text{syst.}) \pm 21.3(\text{lumi.}) \;\; \text{pb.} \tag{6.24}$$

The statistical uncertainty includes all uncertainties that are uncorrelated between the three periods. Correcting the observed number of isolated di-muon events by a factor of 0.885 ± 0.015 for the contribution from γ^* exchange and Z/γ^* interference, the cross section for $p\bar{p} \to Z + X \to \mu^+\mu^- + X$ is measured to be:

$$\sigma\,(Z) = 290.1 \pm 3.0(\text{stat.}) \pm 7.4(\text{syst.}) \pm 18.9(\text{lumi.}) \;\; \text{pb.} \tag{6.25}$$

Figure 6.46 shows this number along with the DØ preliminary measurement in the electron channel [31] and the CDF published measurements in the electron and muon channels combined [33], compared to a SM prediction of the $p\bar{p} \to Z + X \to \ell^+\ell^- + X$ cross section. The theoretical prediction [34] uses the NNLO code [11] augmented with the CTEQ6M PDFs and their associated error functions [26].

The result obtained for $\sigma\,(Z)$ is 2.2 standard deviations from the $Z \to e^+e^-$ result measured at DØ, excluding the common luminosity uncertainty and assuming the common PDF uncertainties to be 100% correlated. It is 1.8 standard deviations from the CDF measurement, assuming the common PDF uncertainties to be 100% correlated and leaving out the common uncertainty on the total inelastic $p\bar{p}$ cross section, $\sigma_{p\bar{p}}$. It is 2.4 standard deviations from the theoretical prediction.

Quantity	Value	Fractional Uncertainty:	
		uncorrelated	correlated
$\int \mathcal{L}dt$ [pb^{-1}]	36.8 $\pm$ 2.4	—	0.065
N_{cand}	2650 $\pm$ 51	0.019	—
ε_{MC}^{eff}	0.239 $\pm$0.007	0.025	0.017
ε_{fz}	0.943 $\pm$ 0.005	0.004	—
σ [pb]	283.0 $\pm$ 9.1	0.032	0.067

Table 6.7: *Summary of the components to the calculation of the cross section for period 1.*

Quantity	Value	Fractional Uncertainty:	
		uncorrelated	correlated
$\int \mathcal{L}dt$ [pb^{-1}]	1.5 $\pm$ 0.1	—	0.065
N_{cand}	146 $\pm$ 12	0.083	—
ε_{MC}^{eff}	0.268 $\pm$ 0.005	0.009	0.017
ε_{fz}	1 $\pm$ 0	—	—
σ [pb]	317.5 $\pm$ 26.4	0.083	0.067

Table 6.8: *Summary of the components to the calculation of the cross section for period 2a.*

Quantity	Value	Fractional Uncertainty:	
		uncorrelated	correlated
$\int \mathcal{L}dt$ [pb^{-1}]	109.4 $\pm$ 7.1	—	0.065
N_{cand}	11556 $\pm$ 107	0.009	—
ε_{MC}^{eff}	0.322 $\pm$ 0.006	0.006	0.017
ε_{fz}	1 $\pm$ 0	—	—
σ [pb]	290.6 $\pm$ 3.2	0.011	0.067

Table 6.9: *Summary of the components to the calculation of the cross section for period 2b.*

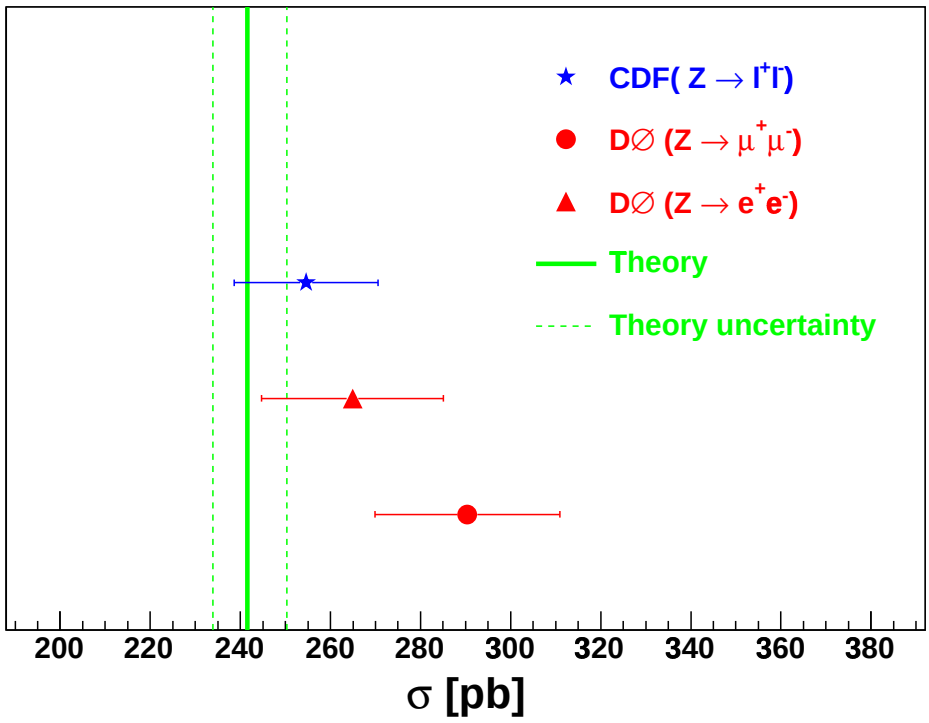

Figure 6.46: *The Standard Model prediction of the cross section for* $p\bar{p} \rightarrow Z + X \rightarrow \ell^+\ell^- + X$. *The experimental measurements in both the muon and electron channels for DØ and the muon and electron channels combined for CDF are shown as points with error bars.*

	HERWIG	PYTHIA
Cuts in x_A and y_A	0.568 ± 0.002	0.567 ± 0.002
Exclude bottom hole	0.801 ± 0.002	0.797 ± 0.002
Kinematic cuts	0.899 ± 0.002	0.896 ± 0.002

Table 6.10: *Breakdown of the acceptance measured using HERWIG and PYTHIA. The numbers are consecutive so that the bottom hole efficiency is for those events that passed the cuts in x_A and y_A, etc.*

6.8 Cross Checks

6.8.1 Acceptance Using HERWIG

The quoted acceptance of $Z/\gamma^* \rightarrow \mu^+\mu^-$ events in the DØ detector is evaluated using the PYTHIA event generator. As a cross check the kinematic and geometric efficiencies are evaluated using the HERWIG event generator. Table 6.10 shows the breakdown of the acceptance numbers measured with both PYTHIA and HERWIG. Both generators use the CTEQ4L PDF set for the purpose of this comparison. Since HERWIG does not model lepton bremsstrahlung, it is also switched off in PYTHIA to allow a direct comparison. The kinematic cuts are made using generator level information. The acceptance found with HERWIG and PYTHIA are in good agreement with one another.

6.8.2 Method to Measure Efficiencies

The reconstruction and trigger efficiencies used in this analysis are measured using $Z/\gamma^* \rightarrow \mu^+\mu^-$ events as described in sections 6.3–6.5. It is possible that this method introduces some bias to the measurement. For example, the control muon is more likely to be identified where the efficiency to reconstruct it is high. Since the test muon is correlated in position with the control muon it may be biased towards particularly (in)efficient parts of the detector. The introduction of the efficiencies into PMCS as a function of position coordinates should take out any biases of this nature.

$Z/\gamma^* \rightarrow \mu^+\mu^-$ DMCS can be used to check for any left over biases. Although the over-all efficiency for muon reconstruction in the muon chambers and central detectors is not properly simulated in DMCS, the basic structure of the detectors

and the correlations between the two muons are assumed to be well modelled. The code used to measure the efficiencies in the $Z/\gamma^* \rightarrow \mu^+\mu^-$ data can be run over a $Z/\gamma^* \rightarrow \mu^+\mu^-$ DMCS sample and the resulting efficiencies can be compared in each bin to those obtained from using the generator level information available in the Monte Carlo. The latter are found by dividing the number of reconstructed loose muons or central tracks by the total number of generated muons coming directly from the $Z/\gamma^* \rightarrow \mu^+\mu^-$ process.

Figure 6.47 shows the tracking efficiency as a function of η_{CFT} in bins of z of the interaction point. Figures 6.48(a) and 6.48(b) show the loose muon identification efficiency as a function of η_A in the regions outside and inside the crack boundaries respectively. Both figures show the efficiencies found using the generator level information and those measured using the control muon - test muon method. The two sets of distributions agree within the statistical uncertainties.

6.8.3 Trigger Efficiencies Using an Independent Trigger Sample

As described in section 6.5, the efficiency to trigger on candidate events is found by breaking down the trigger requirements and measuring each component using $Z/\gamma^* \rightarrow \mu^+\mu^-$ events. As a cross check the over-all trigger efficiency can be measured using candidate events that have been written to tape because they have fired a completely independent trigger. For runs where the trigger to be tested is unprescaled the trigger efficiency is found by:

$$\varepsilon_{\text{trig}}^{\text{indpt}} = \frac{N_{\text{trig+indpt}}}{N_{\text{indpt}}} \tag{6.26}$$

where $N_{\text{trig+indpt}}$ is the number of events firing the trigger in question and an independent trigger and N_{indpt} is the number of events firing an independent trigger.

The independent triggers used in this measurement are a series of electromagnetic and jet triggers which usually means that the $Z/\gamma^* \rightarrow \mu^+\mu^-$ event contains a jet from initial state gluon radiation or a photon from bremsstrahlung radiation. The numbers are therefore compared to the trigger efficiencies found from $Z/\gamma^* \rightarrow \mu^+\mu^-$ PMCS for events with either a 30 GeV jet or a 15 GeV photon, $\varepsilon_{\text{trig}}^{\text{PMCS}}$. Table 6.11 shows the efficiencies measured for the single and di-muon triggers compared to those predicted by PMCS, within the different periods. The numbers are consistent with each other

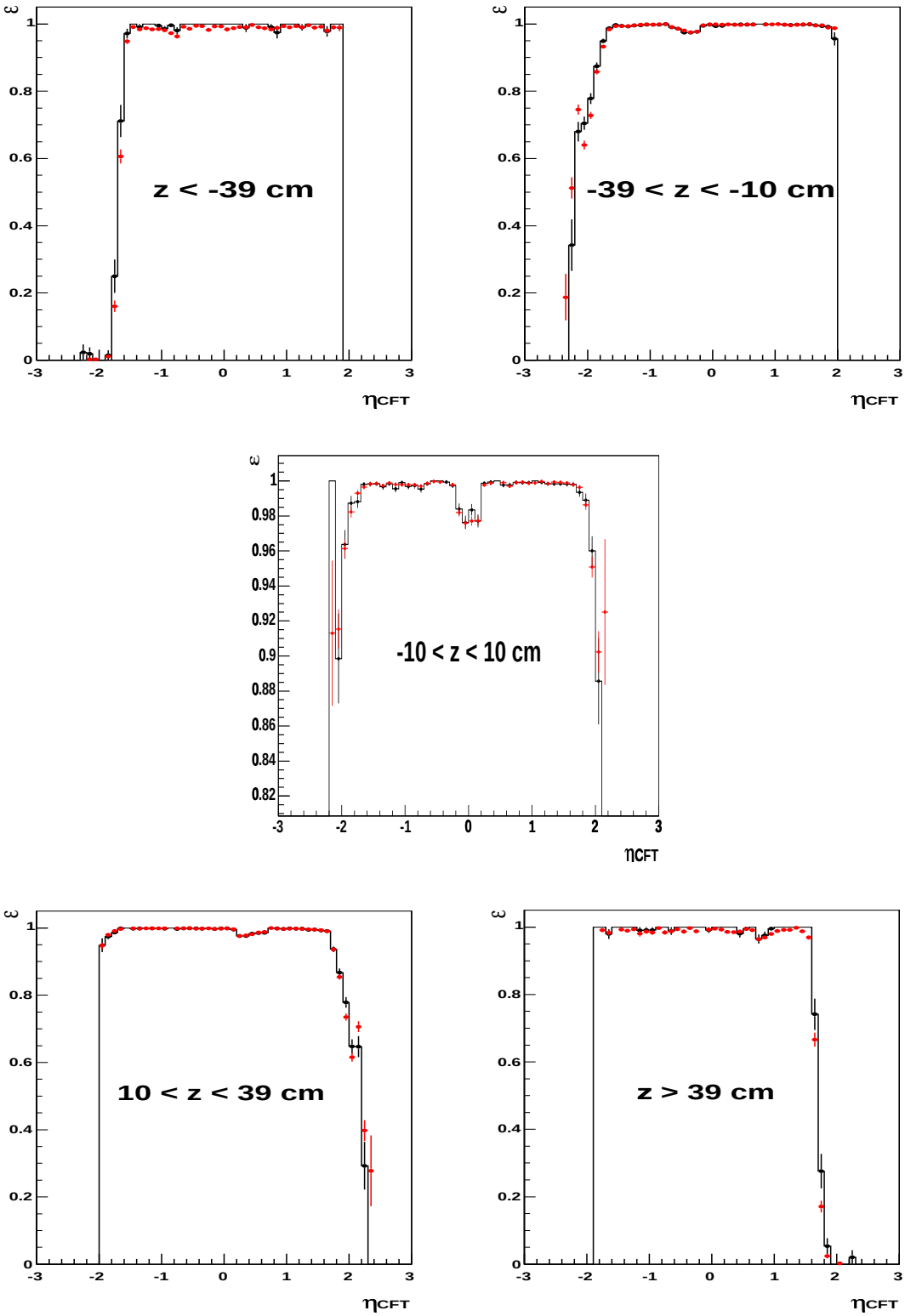

Figure 6.47: *The central tracking efficiency as a function of η_{CFT} in bins of z of the interaction point. Red shows the efficiencies measured using the generator level information and black shows the efficiencies measured using the control muon - test muon method.*

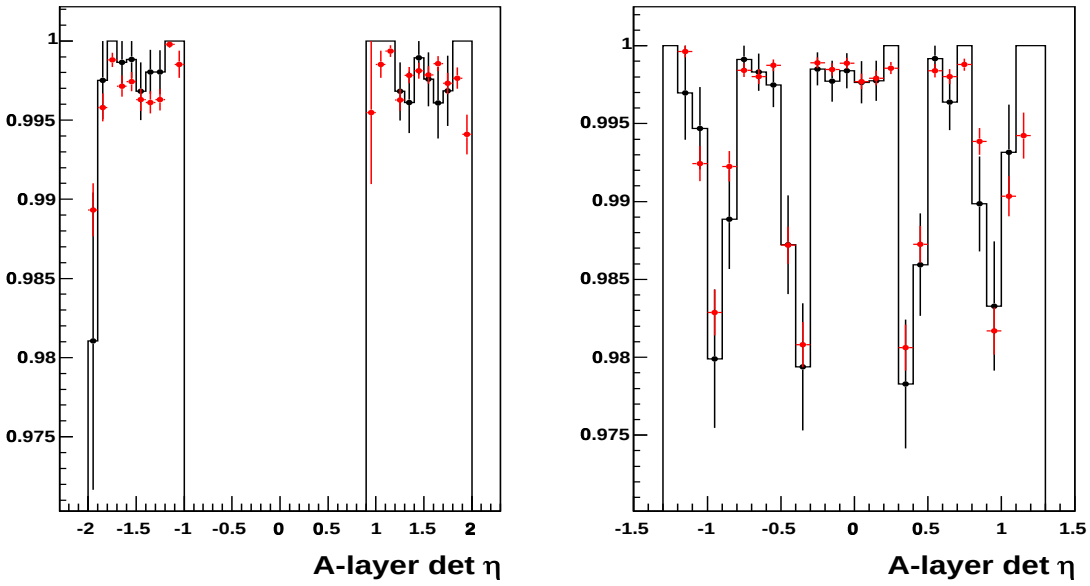

(a)

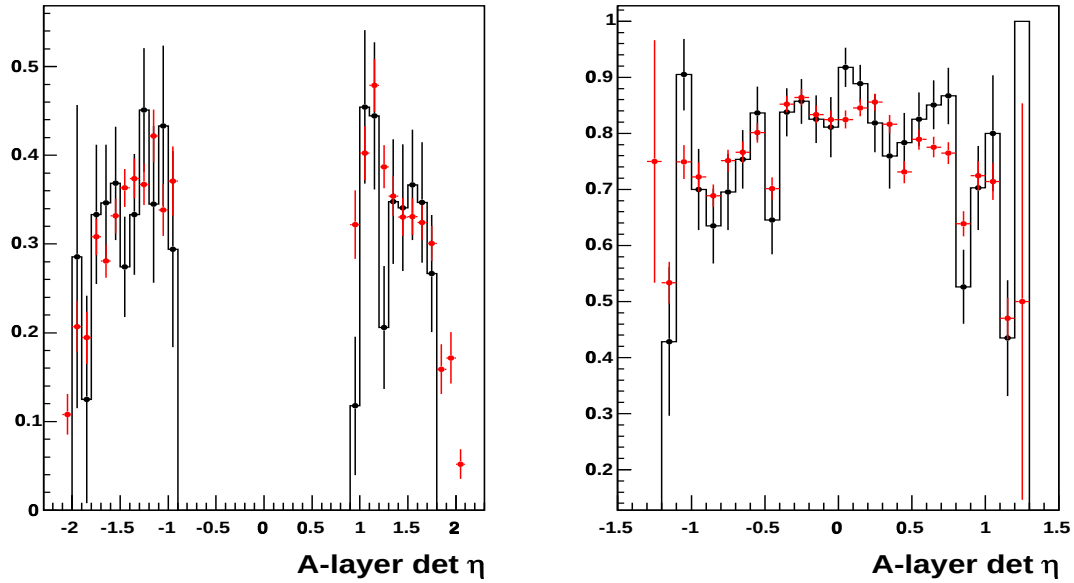

(b)

Figure 6.48: *The loose muon identification efficiency as a function of η_A in (a) the region outside the muon detector boundaries and (b) the region inside the muon detector boundaries. The left hand plots show the central region and the right hand plots show the forward region. Red shows the efficiencies measured using the generator level information and black shows the efficiencies measured using the control muon - test muon method.*

Trigger	Period	$\varepsilon_{\rm trig}^{\rm indpt}$	$\varepsilon_{\rm trig}^{\rm PMCS}$
2MU_L2M0	1	0.67 ± 0.03	0.67
2MU_L2M0	2	0.75 ± 0.02	0.73
MUW_L2M3_TRK10	2	0.86 ± 0.01	0.846

Table 6.11: *Trigger efficiencies measured using the independent trigger method and PMCS.*

within the statistical uncertainties.

6.8.4 Varying the Mass Cut

The value of $\sigma\,(\mathrm{Z})$ can be cross checked by changing the cut on $\mathrm{M}_{\mu\mu}$ from 40 GeV to 60 GeV. This involves re-evaluating $\mathrm{N}_{\rm cand}$, $\varepsilon_{\rm MC}^{\rm eff}$, R_σ and $f_{\rm bckgrd}$. The cross section for the second period changes by 0.4%. The statistical uncertainty on the change of number of candidate events is 0.3%, and since there will be some other uncorrelated uncertainties this is judged to be consistent.

6.8.5 Cross Section in Different Regions

The value for $\sigma\,(\mathrm{Z})$ can be evaluated separately for events where both the muons lie in the central muon system, both the muons lie in the forward system and one muon lies in the forward and one in the central muon system. This is done by re-evaluating $\mathrm{N}_{\rm cand}$ and $\varepsilon_{\rm MC}^{\rm eff}$, with the cross sections determined to be 287.9 ± 4.3 pb^{-1}, 286.3 ± 7.5 pb^{-1} and 292.7 ± 4.1 pb^{-1} respectively. The numbers are consistent within their uncertainties, which are solely due to the statistical uncertainty in the number of candidate events.

Chapter 7

Comparisons of HERWIG and MC@NLO to DØ Data

This chapter presents the comparison of p_T distributions for the W and Z bosons measured at DØ to HERWIG and MC@NLO simulations. Relevant parameters within HERWIG are varied to obtain the closest possible fit to the data. It is important that Monte Carlo generators accurately describe such processes, both as a test of QCD and to minimise the systematic uncertainty on measurements such as m_{W}. The differential cross section as a function of V p_T for the processes
$\mathrm{p\bar{p}} \rightarrow \mathrm{W} + \mathrm{X} \rightarrow \mathrm{e}\nu + \mathrm{X}$ and $\mathrm{p\bar{p}} \rightarrow \mathrm{Z} + \mathrm{X} \rightarrow e^+e^- + \mathrm{X}$ are denoted as p_T^W and p_T^Z respectively.

The data [35, 36] used were collected by DØ between 1994 and 1996, during Run I at the Tevatron. They have been fully corrected for detector acceptance, selection criteria and resolution effects so that a direct comparison can be made to generator level predictions.

7.1 Comparisons of HERWIG to Data

For each of the following Monte Carlo samples, 400000 $\mathrm{p\bar{p}} \rightarrow \mathrm{W} + \mathrm{X} \rightarrow \mathrm{e}\nu + \mathrm{X}$ or $\mathrm{p\bar{p}} \rightarrow \mathrm{Z} + \mathrm{X} \rightarrow e^+e^- + \mathrm{X}$ events were generated using version 6.301 of HERWIG. Figures 7.1 and 7.2 show p_T^W and p_T^Z for the data compared to the HERWIG simulation. The normalisation of the cross section in HERWIG is calculated to LO, and is therefore not expected to be accurate; the shape of the distribution is expected to be more reliable. Consequently, the graphs are normalised so that the total integral under

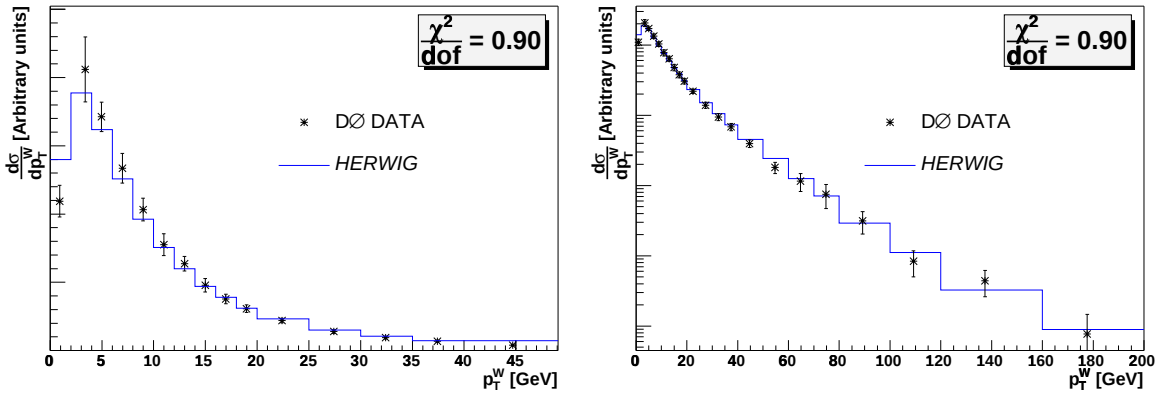

(a) (b)

Figure 7.1: p_T^W *for the data and HERWIG in (a) the low* p_T *range and (b) the entire* p_T *range. Parameters are set to their default values. The given* $\frac{\chi^2}{dof}$ *values correspond to the entire* p_T *range.*

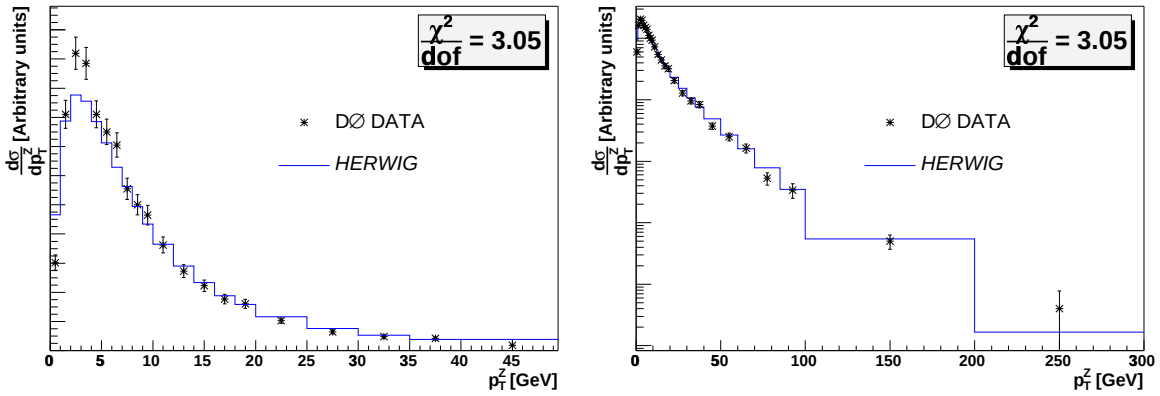

(a) (b)

Figure 7.2: p_T^Z *for the data and HERWIG in (a) the low* p_T *range and (b) the entire* p_T *range. Parameters are set to their default values. The given* $\frac{\chi^2}{dof}$ *values correspond to the entire* p_T *range.*

both of them is equal. The error bars on the data points correspond to both the systematic and statistical uncertainties but do not include an overall normalisation uncertainty in the integrated luminosity. It is likely that there will be some correlation between the systematic uncertainties from point to point[1]. The uncertainties on p_T^W are dominated by systematics, since the neutrino from the W decay cannot be detected and its momentum has to be measured from the total hadronic recoil in the event. The uncertainties on p_T^Z are dominated by statistics.

The χ^2 per degree of freedom of the fit for the entire p_T range is 0.90 for the W, which clearly indicates a very good fit to the data. On closer inspection it is easy to see that the theoretical prediction agrees well with the data points in most of the p_T range but there is a discrepancy in the very low p_T region. There is an excess of events in the lowest p_T bin and a deficit in the next few bins. Since a prediction is only being made for the shape of the distribution, the correlations between the systematic uncertainties are leading to an underestimation of the χ^2.

The χ^2 per degree of freedom of the fit for the Z is 3.05, indicating a less good fit to the data. The excess of points in the first bin and deficit in the next few is present and more apparent. This more realistic value for χ^2 can be attributed to the fact that the uncertainties are dominated by statistics which have no correlations from point to point.

In conclusion, there is a good agreement between the HERWIG predictions and the data for most of the p_T range, with discrepancies in the low p_T region. The next step is to consider the input parameters in HERWIG that will have an effect on the distribution in this region.

7.1.1 HERWIG Parameters

The default HERWIG parameters are taken from tunes to data at the LEP experiments.

[1]The paper [35] that describes the extraction of p_T^W does not include the full error matrix, so that it is not possible to decouple the systematic uncertainties that are correlated from point to point from those that are uncorrelated.

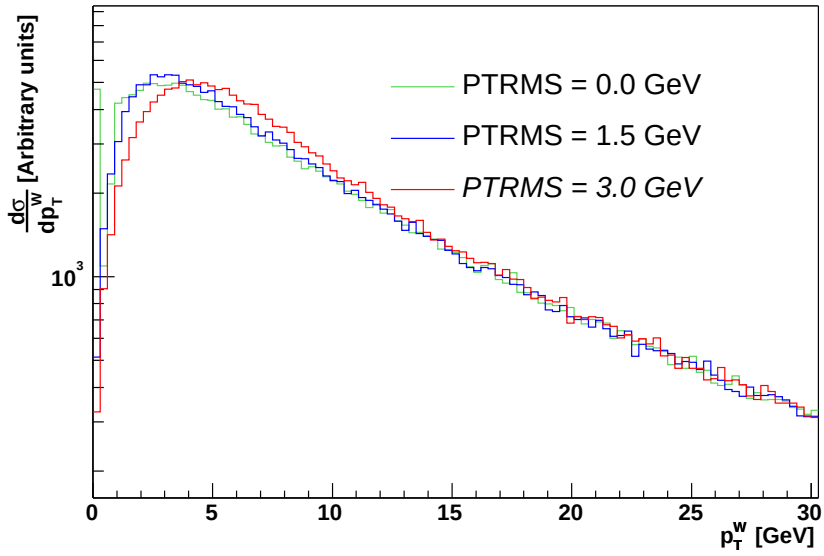

Figure 7.3: p_T^W *with varying values of PTRMS. All other parameters are kept at their default values.*

Intrinsic Transverse Momentum

So far it has been assumed that the p_T acquired by the incoming quarks is exclusively due to recoil from gluon emission. In reality there will also be some intrinsic p_T due to the uncertainty on the position of the quark within the proton. The relevant parameter in HERWIG is known as PTRMS, which is defined as the width of the Gaussian distribution of intrinsic p_T of valence partons in incoming hadrons. Since the parameters in HERWIG were tuned to the e^+e^- data at LEP, where this parameter is irrelevant, it has an unphysical default value of 0.0 GeV. Increasing PTRMS to $\sim$ 1 GeV would have the effect of smearing the distribution in the lowest p_T bins. Figure 7.3 demonstrates qualitatively the effect on p_T^W due to variations in PTRMS. It is evident that increasing PTRMS from 0.0 GeV $\rightarrow$ 1.5 GeV $\rightarrow$ 3.0 GeV has the desired effect of smearing events from the lowest bins, which gets rid of the unphysical spike at 0 GeV. The effect is similar for p_T^Z.

Strong Coupling Constant

The running of $\alpha_s(\mu)$, where μ is the renormalisation scale, is well understood and is governed by the series expansion

$$\mu^2 \frac{d\alpha_s}{d\mu^2} = -\alpha_s^2(\beta_0 + \beta_1\alpha_s + \beta_2\alpha_s^2 + ...) \tag{7.1}$$

where β_n are constants. Experimental input is required to fix the position of the curve by measuring the value of α_s at an arbitrary scale. If equation 7.1 were to be truncated after the first term on the right hand side it could be solved analytically. The value of μ at which α_s in this truncated part of the equation blows up to infinity is the HERWIG parameter related to α_s, known as QCDLAM. It has a default value of 0.18 GeV.

The parton shower is only accurate to the LLA and therefore the renormalisation scheme is not fixed.[2] This means that QCDLAM is allowed to differ from the fundamental parameter $\Lambda^{(5)}_{\overline{\rm MS}}$, which relates to the experimentally measured value of $\alpha_s\,(m_{\rm Z})$ through the modified minimal subtraction scheme, assuming five active quark flavours. The world average value of $\Lambda^{(5)}_{\overline{\rm MS}}$ is 0.202^{+65}_{-53} GeV [37]. If the discrepancy between QCDLAM and $\Lambda^{(5)}_{\overline{\rm MS}}$ were very large it would be an indication that it is necessary to take higher order corrections properly into account. Decreasing QCDLAM decreases α_s at a fixed energy scale. A decrease in α_s leads to smaller probabilities of gluon emission and hence to a lower mean p_T value. This will have the effect of pulling events in the high p_T region into the peak, which is demonstrated in Figure 7.4, where p_T^W is shown for QCDLAM = 0.10, 0.15 and 0.20 GeV. Again, the effect is similar in p_T^Z.

Infrared Cut Off

At low energy scales the parton showers in HERWIG are terminated as α_s becomes too large for perturbative QCD to be reliable. In these regions processes are described by non-perturbative, phenomenological models. The cutoff point between perturbative and non-perturbative physics is known as the infrared cutoff, Q_i, and is given by

$$Q_i = RMASS(i) + Q_0, \tag{7.2}$$

[2]The LO and LL terms are renormalisation scheme independent. In order to fix the scheme it is necessary to include NLO or NLL terms.

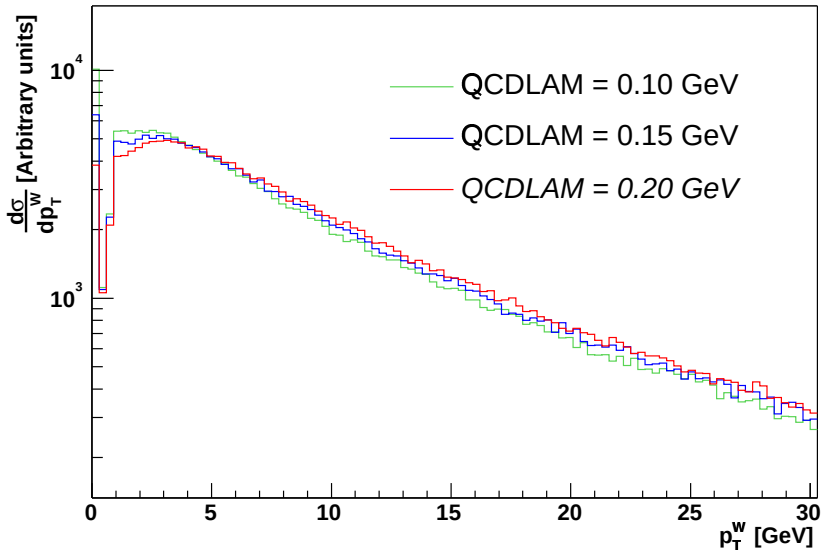

Figure 7.4: p_T^W *with varying values of QCDLAM. All other parameters are kept at their default values.*

where $RMASS(i)$ for $i = 1$ ... 6, 13 is the effective parton mass for d, u, s, c, b, t, g, and Q_0 is set by the quark and gluon cutoff parameters, VQCUT and VGCUT.

At each stage in the branching, the renormalisation scale is set to the component of the momentum of the emitted parton transverse to the direction of the emitter. The showers are terminated when this scale is less than Q_i. [3]

In an ideal world the value of the cutoff would not affect the physical results as the two regions of physics should match. However, the predictions are only reliable in the perturbative region. The value of the cutoff has to be a compromise between understanding the process better and a reasonable cutoff from the perturbative region.

In the case of final state partons the p_T at scales below the cutoff is provided by the energy release when a cluster decays isotropically to hadrons and is of the order of a few GeV. For initial state partons the only source of p_T below the cutoff is from the intrinsic p_T of the quarks within the incoming hadron. With PTRMS set at its default of 0.0 GeV, any events with no emitted gluons due to the cutoff have zero p_T. This is the reason for the unphysical spike in the lowest p_T bin.

The parameter chosen to investigate the behaviour of the cutoff is VQCUT, which

[3] This statement is only exact in the massless limit. The kinematics are modified due to the effective masses of the partons, although the statement is still approximately true.

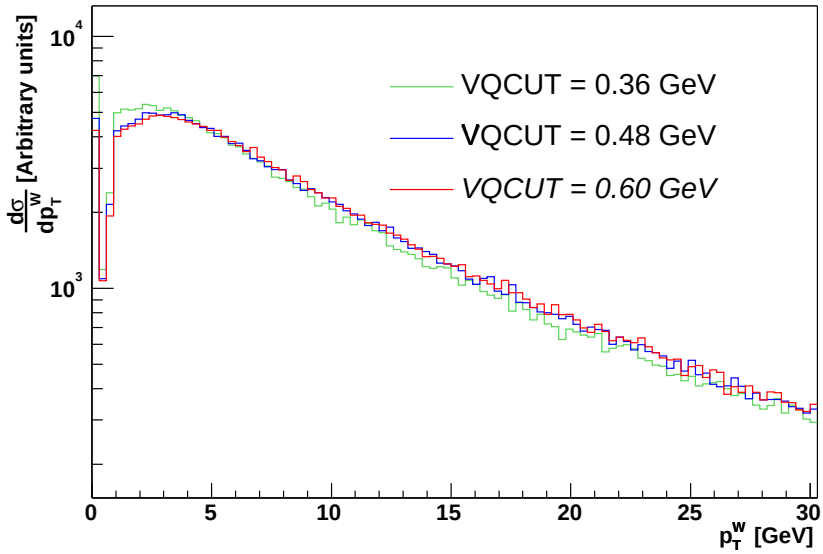

Figure 7.5: p_T^W *with varying values of VQCUT. All other parameters are kept at their default values.*

has a default value of 0.48 GeV. VGCUT would also affect the p_T distributions and including this parameter when fitting the data is a possible avenue for future work. Figure 7.5 shows the variation in p_T^W due to changes in VQCUT. Again, the effect on p_T^Z is similar. As VQCUT is decreased partons with lower p_T are included in the simulation and events in the spike at 0.0 GeV should be pulled into the low p_T bins. However, the number of events in the spike increase as VQCUT deceases; this is not understood [38]. There is a saturation of this effect above about 0.5 GeV with no further variation in the number of events in the spike; there is also very little variation in the full p_T distribution from $\sim$ 0.5 GeV to $\sim$ 1.0 GeV, which is also not understood. There is a noticeable change in the distributions in the range $10 < p_T < 30$ GeV, despite the fact that the changes made are at energy scales of $\sim$ 0.5 GeV. In this region a large contribution to the cross section is from events where most of the momentum acquired is due to the emission of a single hard gluon. The observed decrease in the cross section with a decrease in the value of the cutoff may possibly be attributable to the fact that an increase in the number of soft gluons emitted at large angles leads to a decrease in the amount of energy left available for the emission of a hard gluon at smaller angles.

7.1.2 Tuning the Parameters

A parameter is tuned by varying it and performing χ^2 fits to the data in the entire p_T range. A quadratic polynomial[4] is fitted to the distribution of χ^2 as a function of the parameter. The best fit value is found by minimising the polynomial and the uncertainty is found by allowing the absolute χ^2 to vary from $\chi^2_{min} \rightarrow \chi^2_{min} + 1$.

Each of the three parameters will be considered in turn and tuned separately to p_T^W and p_T^Z. When the best fit value for a parameter is obtained it will be held at that value whilst the other parameters are tuned. The tuning process will then be repeated with variations of the first parameter investigated whilst all other parameters are held at their new best fit values. Since there is no reason for the parameters to have different values when tuned to p_T^W and p_T^Z, the respective best fit values will be combined to give an overall best fit value for each parameter.

Figures 7.6(a) and 7.6(b) show a plot of χ^2 against PTRMS for p_T^W and p_T^Z, which give best fit values for PTRMS of 1.6 $\pm$ 0.2 GeV and 1.2 $\pm$ 0.1 GeV respectively. Plots of the differential cross section in the low p_T region (any difference in the high p_T region is negligible) with the new tuned input values for PTRMS are shown in Figures 7.7(a) and 7.7(b) for p_T^W and p_T^Z. The improved χ^2 per degree of freedom values are 0.43 and 1.24. As expected, some events from the lowest bin have been redistributed in the next few bins and the distribution has broadened.

The next parameter to be tuned is QCDLAM. The tuning is done with PTRMS kept at its respective new best fit values. Figures 7.8(a) and 7.8(b) show a plot of χ^2 against QCDLAM for p_T^W and p_T^Z, which give best fit values for QCDLAM of 0.16 $\pm$ 0.02 GeV and 0.15 $\pm$ 0.01 GeV respectively. Plots of the differential cross section in the low p_T region (any difference in the high p_T region is negligible) with the new tuned input values for PTRMS and QCDLAM are shown in Figures 7.9(a) and 7.9(b) for p_T^W and p_T^Z respectively. The new χ^2 per degree of freedom values are 0.46 and 0.92.

Figures 7.10(a) and 7.10(b) show χ^2 against VQCUT for p_T^W and p_T^Z. The distributions do not appear quadratic in the region above $\sim$ 0.5 GeV since varying VQCUT

[4]It should be noted that the χ^2 distributions are not perfect quadratic polynomials. This comes, in part, from fluctuations in χ^2 values due to the limited statistics of the Monte Carlo samples. The best fit values and their uncertainties should therefore be considered to be an approximation that gives a rough idea of the acceptable range.

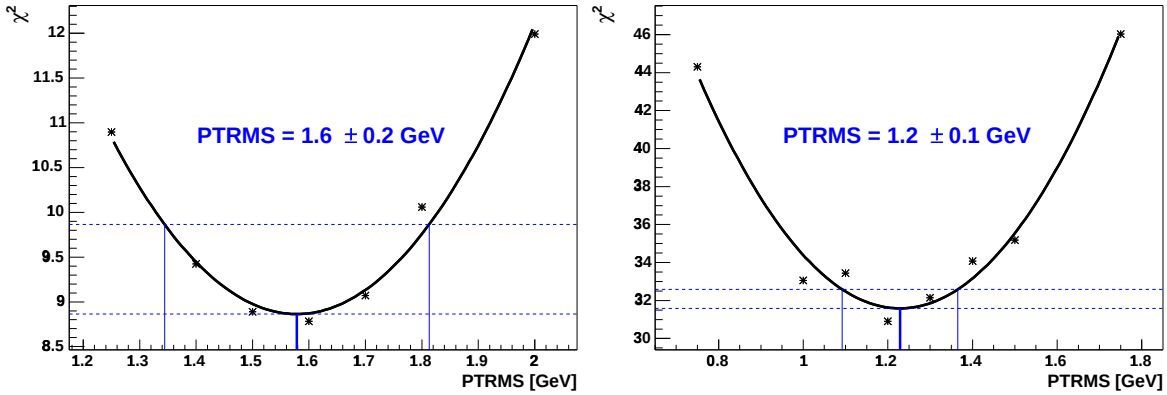

(a) (b)

Figure 7.6: *Absolute χ^2 of HERWIG fit to data for (a) p_T^W and (b) p_T^Z as a function of PTRMS.*

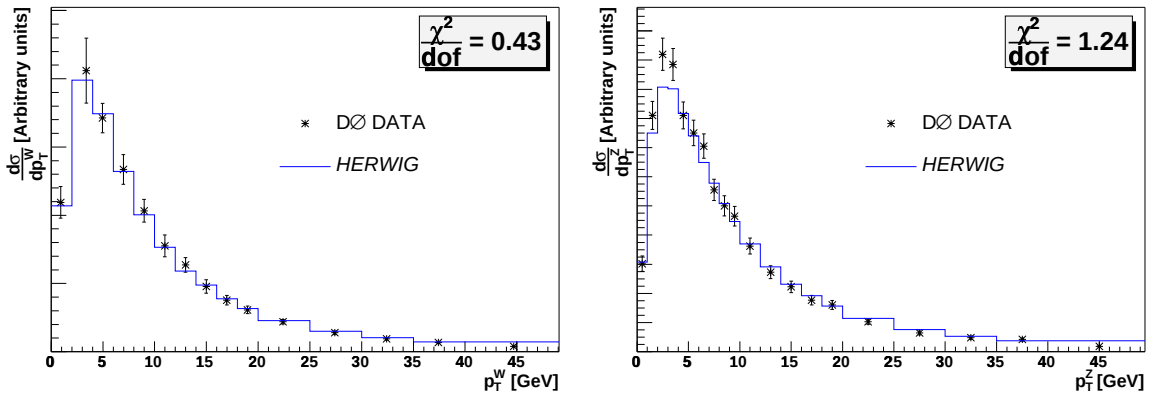

(a) (b)

Figure 7.7: *(a) p_T^W for the data and HERWIG. Parameters are set to PTRMS=1.6 GeV, QCDLAM=0.18 GeV, VQCUT=0.48 GeV. (b) p_T^Z for the data and HERWIG. Parameters are set to PTRMS=1.2 GeV, QCDLAM=0.18 GeV, VQCUT=0.48 GeV. The given $\frac{\chi^2}{dof}$ values correspond to the entire p_T range.*

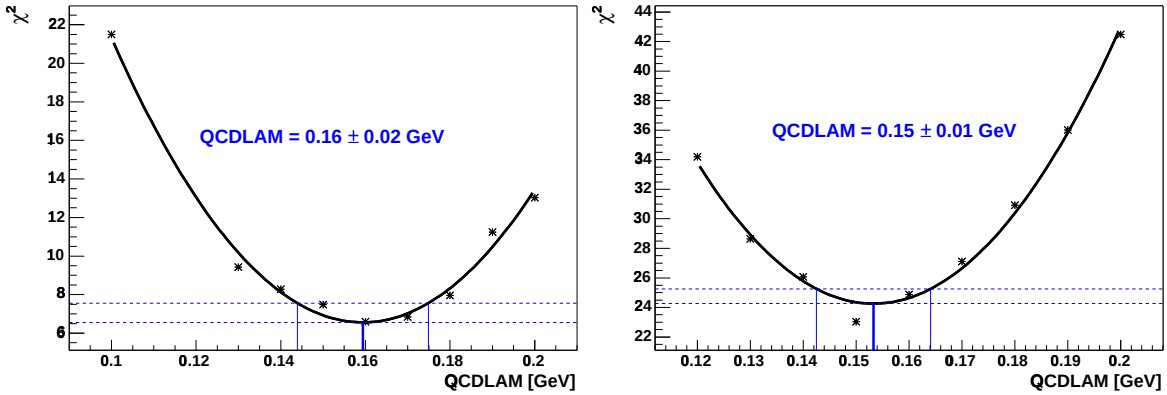

(a) (b)

Figure 7.8: *Absolute χ^2 of HERWIG fit to data for (a) p_T^W and (b) p_T^Z as a function of QCDLAM.*

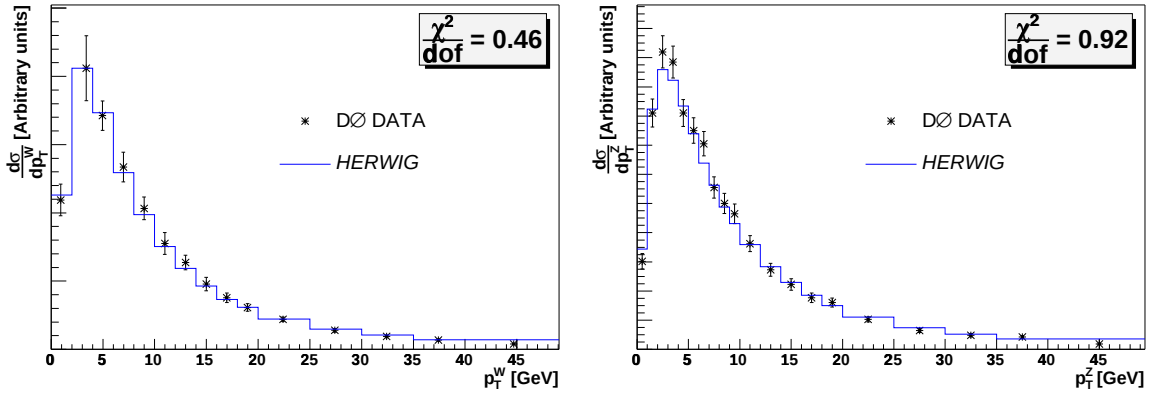

(a) (b)

Figure 7.9: *(a) p_T^W for the data and HERWIG. Parameters are set to PTRMS=1.6 GeV, QCDLAM=0.16 GeV, VQCUT=0.48 GeV. (b) p_T^Z for the data and HERWIG. Parameters are set to PTRMS=1.2 GeV, QCDLAM=0.15 GeV, VQCUT=0.48 GeV. The given $\frac{\chi^2}{dof}$ values correspond to the entire p_T range.*

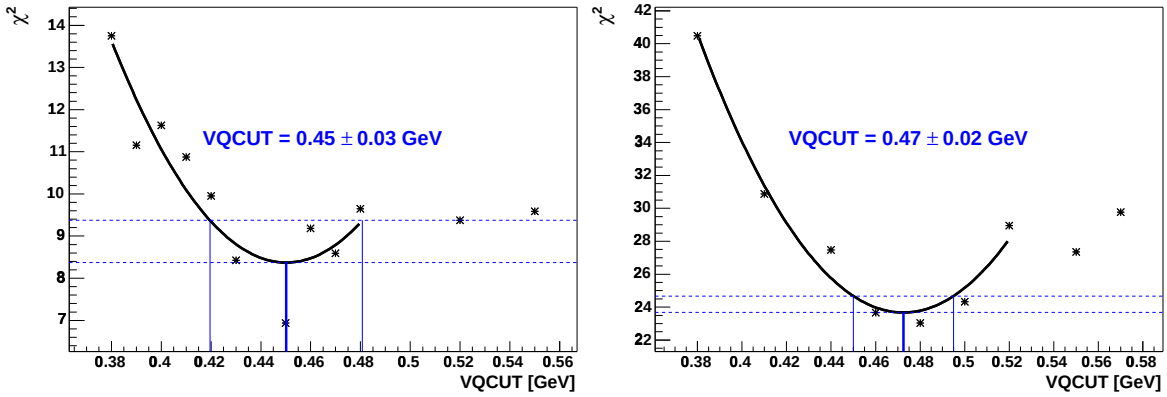

(a) (b)

Figure 7.10: *Absolute χ^2 of HERWIG fit to data for (a) p_T^W and (b) p_T^Z as a function of VQCUT.*

from $\sim$ 0.5 GeV to $\sim$ 1.0 GeV has little affect on the p_T distributions. The best fit value for VQCUT is 0.45 $\pm$ 0.03 GeV for p_T^W and 0.47 $\pm$ 0.02 GeV for p_T^Z. The upper bound on the uncertainties are probably under-estimations, due to the non-quadratic behaviour of the χ^2 distribution in this region. Plots of the differential cross section in the low p_T region (any difference in the high p_T region is negligible) with the new tuned input values for PTRMS, QCDLAM and VQCUT are shown in Figures 7.11(a) and 7.11(b) for p_T^W and p_T^Z respectively. This time the distributions do not appear to be noticeably different. The respective new values for the χ^2 per degree of freedom are 0.38 and 0.95.

The three parameters considered are by no means independent of each other in the way that they affect the p_T distributions. The tuning process is therefore repeated for each parameter in turn, with the other parameters held at their new values. This is done a total of three times. The results of the best fit values for each step in the tuning process are shown in Table 7.1. Figures 7.12 and 7.13 show p_T^W and p_T^Z with their best fit parameters. The χ^2 per degree of freedom values are now 0.35 for p_T^W and 0.69 for p_T^Z.

The best fit values of the parameters tuned to p_T^W and p_T^Z agree within their uncertainties, assuming that they are uncorrelated. Since the uncertainties on p_T^W are dominated by systematics and those on p_T^Z are dominated by statistics, this is a

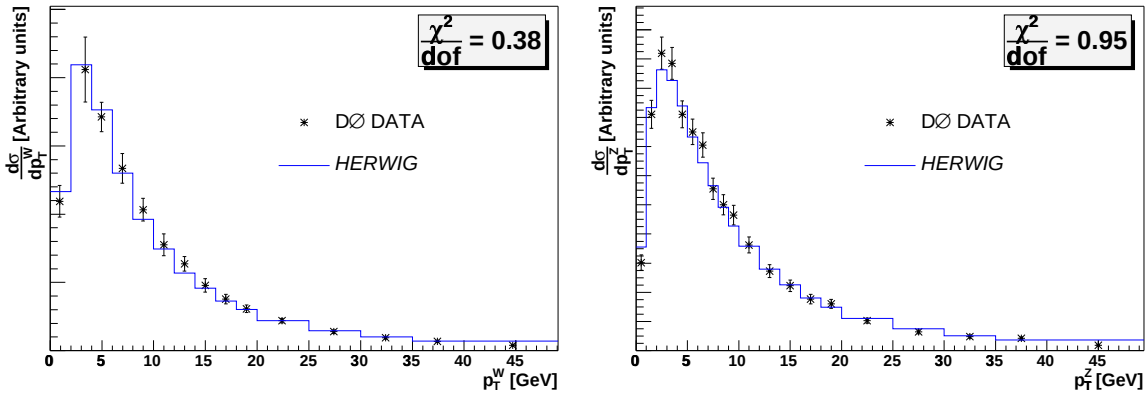

(a) (b)

Figure 7.11: *(a) p_T^W for the data and HERWIG. Parameters are set to PTRMS=1.6 GeV, QCDLAM=0.16 GeV, VQCUT=0.45 GeV. (b) p_T^Z for the data and HERWIG. Parameters are set to PTRMS=1.2 GeV, QCDLAM=0.15 GeV, VQCUT=0.47 GeV. The given $\frac{\chi^2}{dof}$ values correspond to the entire p_T range.*

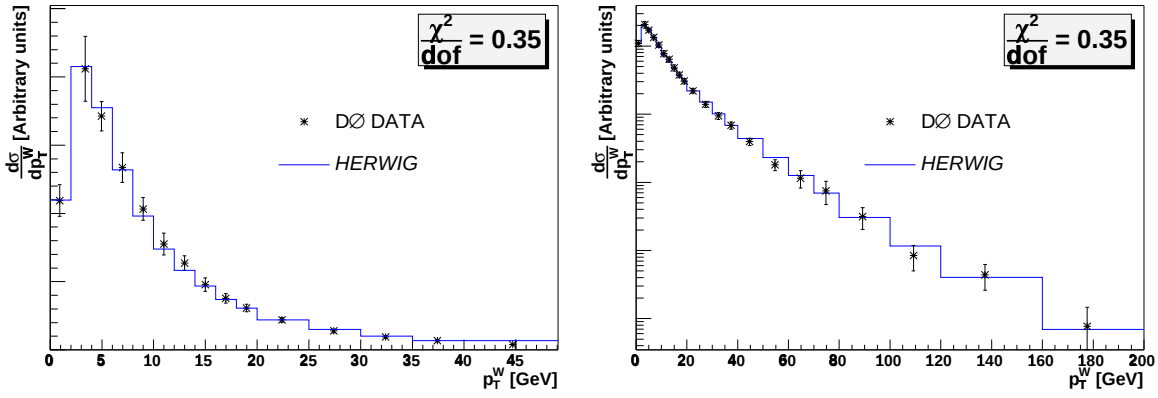

(a) (b)

Figure 7.12: *p_T^W for the data and HERWIG in (a) the low p_T range and (b) the entire p_T range. Parameters are set to PTRMS=1.7 GeV, QCDLAM=0.16 GeV, VQCUT=0.46 GeV. The given $\frac{\chi^2}{dof}$ values correspond to the entire p_T range.*

		W	Z
PTRMS [GeV]	default	0	0
	1st tune	1.58 ± 0.23	1.23 ± 0.14
	2nd tune	1.68 ± 0.28	1.49 ± 0.12
	3rd tune	1.71 ± 0.29	1.58 ± 0.11
QCDLAM [GeV]	default	0.18	0.18
	1st tune	0.159 ± 0.015	0.153 ± 0.011
	2nd tune	0.160 ± 0.021	0.139 ± 0.011
	3rd tune	0.160 ± 0.021	0.140 ± 0.012
VQCUT [GeV]	default	0.48	0.48
	1st tune	0.450 ± 0.031	0.472 ± 0.022
	2nd tune	0.463 ± 0.050	0.460 ± 0.029
	3rd tune	0.463 ± 0.050	0.451 ± 0.031

Table 7.1: *Best fit values with uncertainties for PTRMS, QCDLAM and VQCUT using p_T^W and p_T^Z, for each step in the tuning process.*

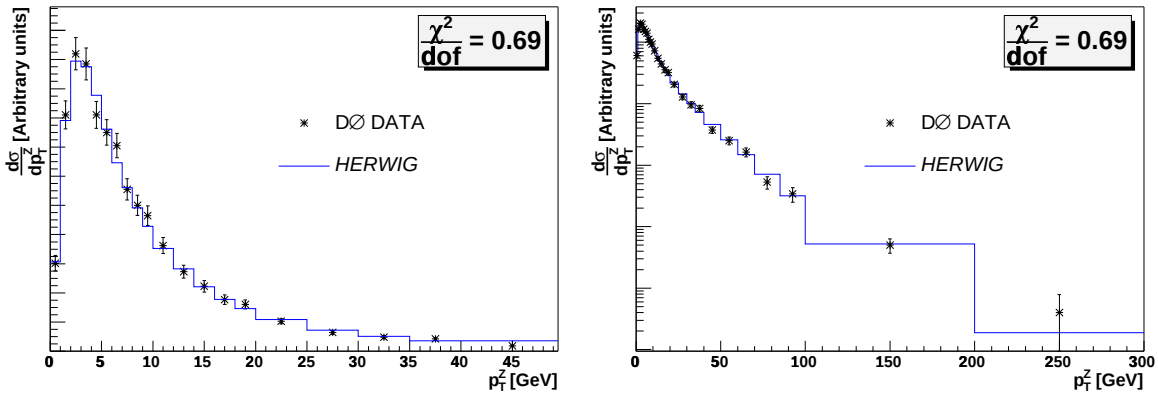

(a) (b)

Figure 7.13: *p_T^Z for the data and HERWIG in (a) the low p_T range and (b) the entire p_T range. Parameters are set to PTRMS=1.6 GeV, QCDLAM=0.14 GeV, VQCUT=0.45 GeV. The given $\frac{\chi^2}{dof}$ values correspond to the entire p_T range.*

reasonable approximation. The parameters can therefore be combined to give:

$$\text{PTRMS} = 1.6 \pm 0.1 \text{ GeV}, \tag{7.3}$$

$$\text{QCDLAM} = 0.14 \pm 0.01 \text{ GeV}, \tag{7.4}$$

$$\text{VQCUT} = 0.45 \pm 0.03 \text{ GeV}. \tag{7.5}$$

Using these average parameters the χ^2 per degree of freedom values are 0.43 and 0.74 for p_T^W and p_T^Z respectively, which are still excellent fits.

It is possible that the best fit values for the three parameters depend on which parameter is tuned first. In order to investigate this, the tuning procedure is repeated starting with each of the three parameters in turn to see if different best fit values are found. QCDLAM and VQCUT are found to be completely correlated, with the best fit value obtained for QCDLAM depending on the starting value of VQCUT and vice versa. The tuning process converges to give pairs of best fit values with approximately constant values of χ^2. By fitting a straight line through a plot of the best fit value of VQCUT against that for QCDLAM, VQCUT can be expressed in terms of QCDLAM with the following functional form:

$$\text{VQCUT} \approx -2.3 \times \text{QCDLAM} + 0.85 \text{ GeV}. \tag{7.6}$$

PTRMS is independent of the order of tuning and always converges to the same value.

7.1.3 Input PDFs

PDFs of the incoming beam hadrons are required in the HERWIG simulation. There are some internal PDF sets that can be used. Alternatively, it is possible to use an interface to the parton distribution library, PDFLIB [39]. PDFLIB contains different sets of PDFs that have been fitted to data by different groups, such as MRST and CTEQ. The default PDF used is an internal set which is an average of two published MRST sets [40].

It is possible that the choice of PDF set may affect the vector boson p_T distributions. In order to investigate this possibility, the input PDF set is varied, with all parameters kept at their default values. Figures 7.14(a) and 7.14(b) show the data plotted against HERWIG distributions using seven different PDF sets from the MRST [41] and CTEQ [32, 42] groups as input for p_T^Z in the low and entire p_T ranges respectively. The PDF sets do not differ significantly from one another in the way they affect p_T^Z, with any differences negligible compared to the experimental uncer-

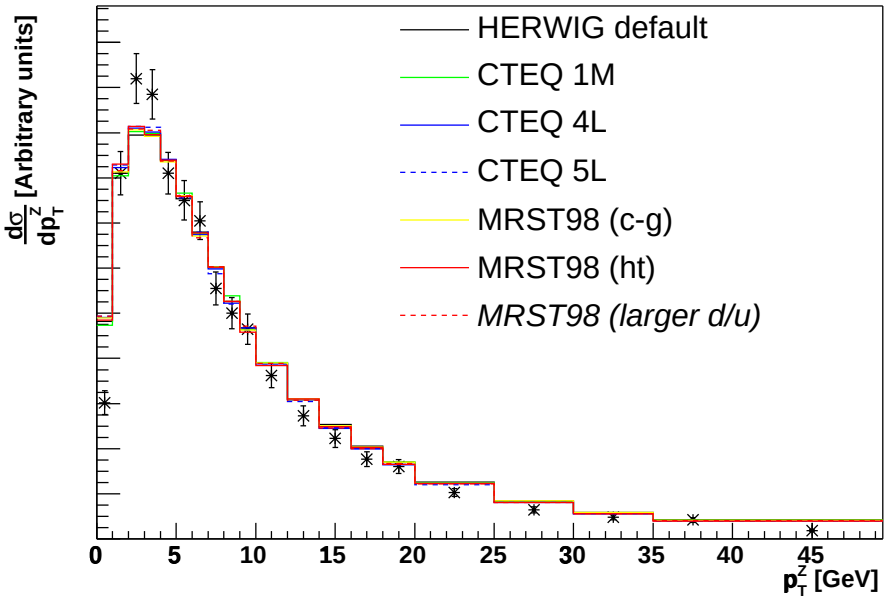

(a)

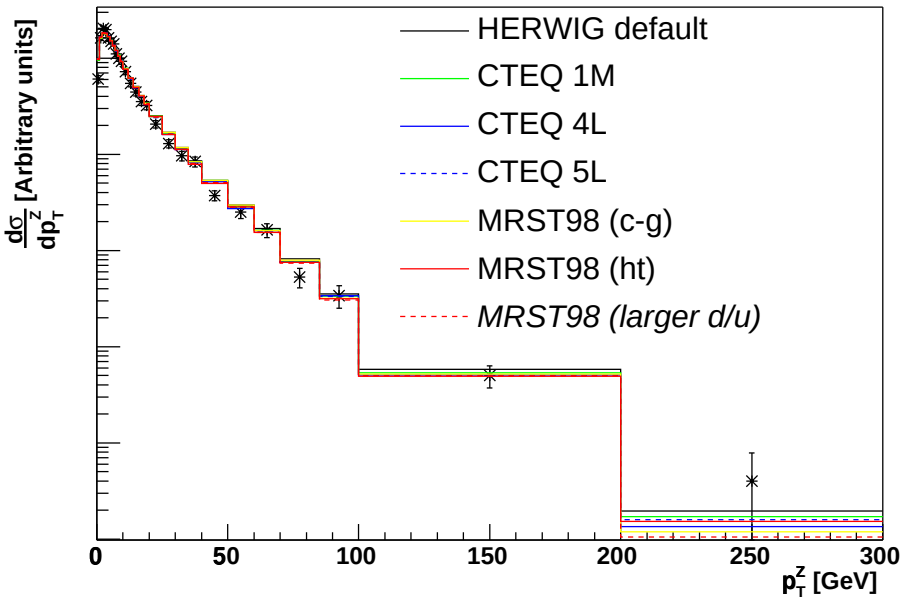

(b)

Figure 7.14: p_T^Z *in (a) the low* p_T *range and (b) the entire* p_T *range. Points with error bars show the data, histograms show HERWIG prediction with various input PDF sets. Parameters are set to their default values.*

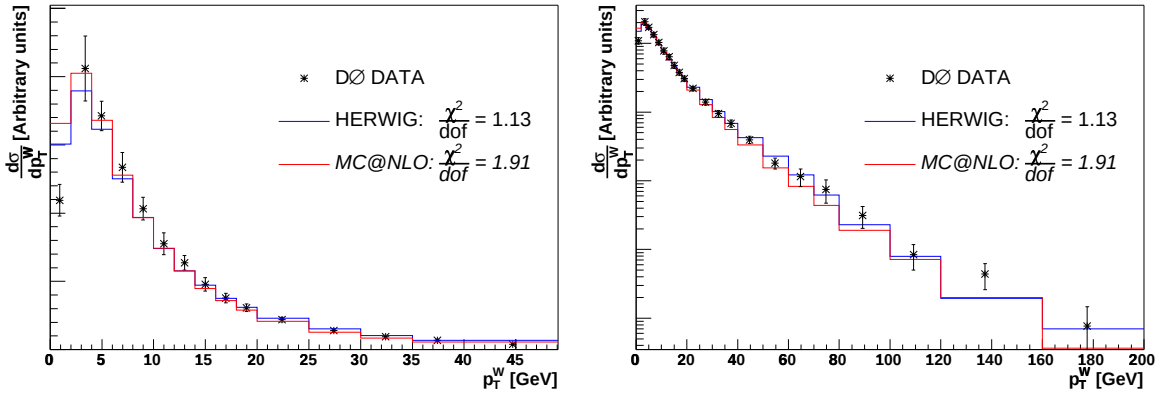

(a) (b)

Figure 7.15: p_T^W *for the data, HERWIG and MC@NLO in (a) the low* p_T *range and (b) the entire* p_T *range. Parameters are set to their default values. The given* $\frac{\chi^2}{dof}$ *values correspond to the entire* p_T *range.*

tainties. It is therefore concluded that the choice of PDF set is not relevant for this study.

7.2 Comparisons of MC@NLO to HERWIG and Data

HERWIG version 6.505 was used for the following study as any versions prior to 6.5 cannot be interfaced with MC@NLO. Since the HERWIG p_T distributions in this section are made using version 6.505 there are slight differences to those made using version 6.301 in section 7.1. The differences can be attributed to a bug fix in the forced backward evolution to a valence quark, which was resulting in the rejection of some events [43]. Again, each of the Monte Carlo samples contains 400000 $p\bar{p} \rightarrow W + X \rightarrow e\nu + X$ or $p\bar{p} \rightarrow Z + X \rightarrow e^+e^- + X$ events.

For the case of W and Z production at the Tevatron, which are purely electroweak processes at LO, MC@NLO takes into consideration any diagrams with an additional external gluon or gluon loop. Comparisons of p_T^W and p_T^Z for data, standard HERWIG and MC@NLO predictions are shown in Figures 7.15 and 7.16 respectively. All parameters are set at their default values. Since HERWIG matches the parton shower to an exact $\mathcal{O}(\alpha_S)$ matrix element for hard radiation, which corresponds to

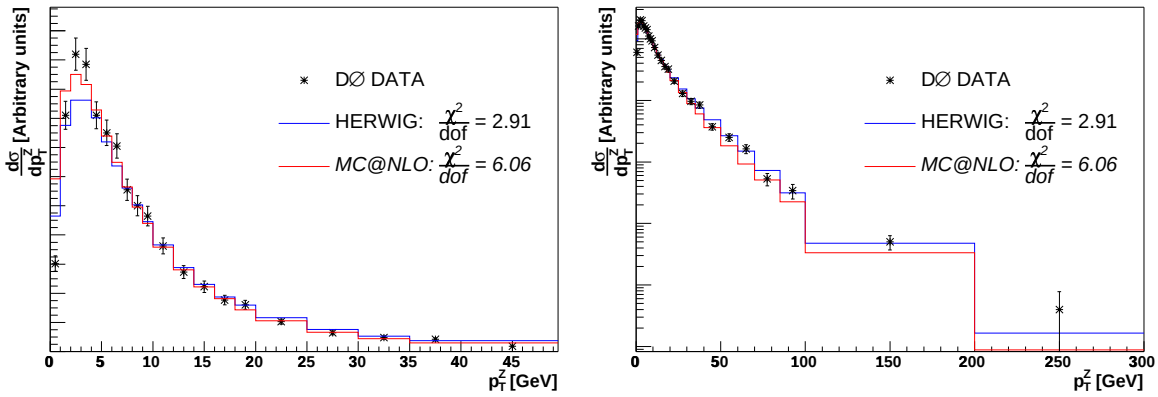

(a) (b)

Figure 7.16: *p_T^Z for the data, HERWIG and MC@NLO in (a) the low p_T range and (b) the entire p_T range. Parameters are set to their default values. The given $\frac{\chi^2}{dof}$ values correspond to the entire p_T range.*

the emission of one hard gluon, it should agree with MC@NLO in this region of phase space. MC@NLO is above HERWIG in the low p_T region and below it in the high p_T region. The distributions are normalised to the same area, so the increase in the cross section in the low p_T region for MC@NLO is causing an apparent decrease in the high p_T region, where they should be equivalent.

The fit to the data is worse for MC@NLO using the default parameters, with χ^2 per degree of freedom values of 1.91 and 6.06 for p_T^W and p_T^Z respectively. This may, in part, be due to the fact that the default parameters are taken from HERWIG tunes to LEP data.

7.2.1 Tuning the Parameters

The tuning process for the three parameters introduced in section 7.1.1 is repeated using MC@NLO. Table 7.2 summarises the best fit values for the parameters during the tuning process. The uncertainty on the value of VQCUT obtained using p_T^W is large compared to that obtained from p_T^Z. It is also large compared with the values obtained from the HERWIG tunes. This is due to the fact that varying VQCUT from $\sim$ 0.5 GeV to $\sim$ 1.0 GeV has a very small effect on the p_T distributions. Since the best fit value obtained using p_T^W is 0.57 this leads to a relatively large uncertainty. Figures 7.17 and 7.18 show p_T^W and p_T^Z for data, HERWIG and MC@NLO, with the

		W	Z
PTRMS [GeV]	default	0	0
	1st tune	1.80 ± 0.25	1.48 ± 0.13
	2nd tune	1.46 ± 0.32	1.35 ± 0.14
	3rd tune	1.35 ± 0.33	1.36 ± 0.13
QCDLAM [GeV]	default	0.18	0.18
	1st tune	0.202 ± 0.014	0.189 ± 0.011
	2nd tune	0.210 ± 0.017	0.189 ± 0.011
	3rd tune	0.212 ± 0.017	0.191 ± 0.011
VQCUT [GeV]	default	0.48	0.48
	1st tune	0.533 ± 0.047	0.503 ± 0.025
	2nd tune	0.57 ± 0.22	0.511 ± 0.027
	3rd tune	0.57 ± 0.22	0.511 ± 0.027

Table 7.2: *MC@NLO best fit values with uncertainties for PTRMS, QCDLAM and VQCUT using p_T^W and p_T^Z, for each step in the tuning process.*

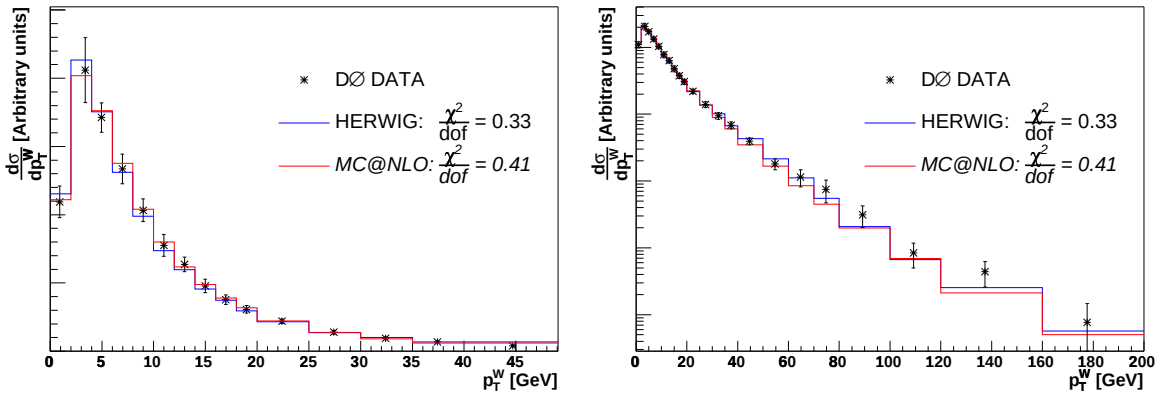

(a) (b)

Figure 7.17: *p_T^W for the data, HERWIG and MC@NLO in (a) the low and (b) the entire p_T range. For HERWIG(MC@NLO) parameters are set to PTRMS=1.7(1.4) GeV, QCDLAM=0.16(0.21) GeV, VQCUT=0.46(0.57) GeV. The given $\frac{\chi^2}{dof}$ values correspond to the entire p_T range.*

parameters in HERWIG and MC@NLO set to their respective best fit values.

The values of the parameters obtained using the MC@NLO tunes to p_T^W and p_T^Z

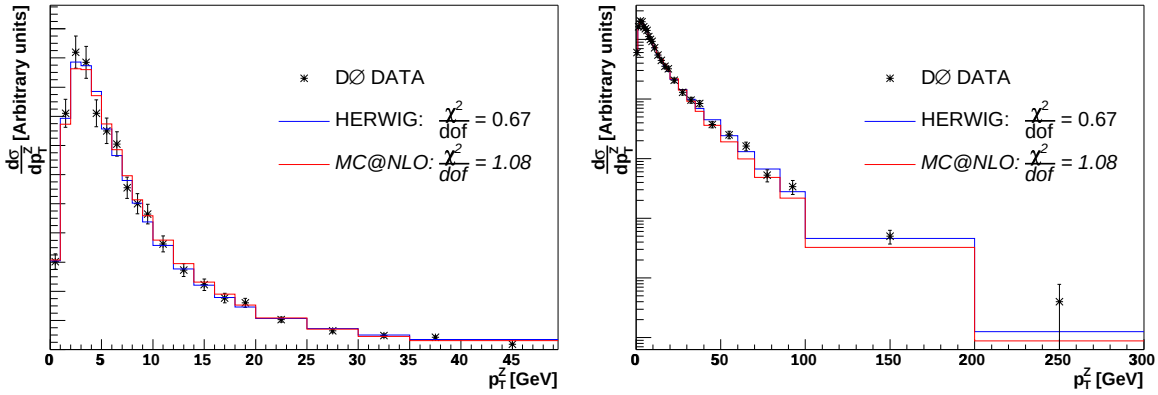

(a) (b)

Figure 7.18: *p_T^Z for the data, HERWIG and MC@NLO in (a) the low and (b) the entire p_T range. For HERWIG(MC@NLO) parameters are set to PTRMS=1.6(1.4) GeV, QCDLAM=0.14(0.19) GeV, VQCUT=0.45(0.51) GeV. The given $\frac{\chi^2}{dof}$ values correspond to the entire p_T range.*

agree within their uncertainties, and are therefore combined to give:

$$\text{PTRMS} = 1.4 \pm 0.1 \text{ GeV}, \tag{7.7}$$

$$\text{QCDLAM} = 0.197 \pm 0.009 \text{ GeV}, \tag{7.8}$$

$$\text{VQCUT} = 0.51 \pm 0.03 \text{ GeV}. \tag{7.9}$$

Using these average parameters the χ^2 per degree of freedom values are 0.61 and 0.69 for p_T^W and p_T^Z respectively, which indicate excellent fits.

7.2.2 HERWIG Compared to MC@NLO

Table 7.3 summarises the best fit parameters found by combining the values obtained from fits to p_T^W and p_T^Z for HERWIG and MC@NLO. The uncertainties are highly correlated as the same data is used in the tuning process. Tuning with MC@NLO results in a slightly lower value for PTRMS with respect to HERWIG. This is more realistic as the inverse size of a proton is $\sim$ 200 MeV. The larger value of PTRMS highlights the fact that it accounts for all non-perturbative QCD effects, not just the intrinsic p_T of the proton. MC@NLO gives a higher value for QCDLAM, which is closer to the central value of $\Lambda_{\overline{MS}}$. MC@NLO also gives a higher VQCUT value,

	HERWIG	MC@NLO
PTRMS [GeV]	1.6 ± 0.1	1.4 ± 0.1
QCDLAM [GeV]	0.14 ± 0.01	0.197 ± 0.009
VQCUT [GeV]	0.45 ± 0.03	0.51 ± 0.03

Table 7.3: *Best fit values with uncertainties for PTRMS, QCDLAM and VQCUT using combinations from fits to p_T^W and p_T^Z, for HERWIG and MC@NLO.*

despite the fact that it was observed to be inversely proportional to QCDLAM in the HERWIG distributions.

After tuning MC@NLO, the fits to the data are still slightly worse than those for HERWIG. However, the χ^2 values all indicate good descriptions of the data. MC@NLO appears to be slightly under-estimating the cross section in the high p_T region with respect to the low p_T region, although this effect is small.

7.3 Conclusions

Both standard HERWIG and MC@NLO provide extremely good descriptions of p_T^W and p_T^Z measured at DØ during Run I at the Tevatron when relevant input parameters are tuned. This is encouraging as it suggests that the calculations and models used in the Monte Carlo programs are reliable. VQCUT and QCDLAM were found to be completely correlated with one another in the way they affect the p_T distributions. It will be necessary to use other distributions to try and differentiate between the parameters. One possibility is $\frac{\sigma(\mathrm{W}+(n+1)J)}{\sigma(\mathrm{W}+nJ)}$, the ratio of the cross section for $\mathrm{p\bar{p}} \rightarrow$ W+ (n+1) jets to that for $\mathrm{p\bar{p}} \rightarrow$ W+ n jets, which will depend on the input value of QCDLAM. Varying PDF sets did not affect the p_T distributions at a significant level compared to the experimental uncertainties. Another possible parameter to be included in future fits to the data is VGCUT. Since the $\frac{\chi^2}{dof}$ values are already low without including this parameter, it is concluded that it is reasonable to wait for experimental data with reduced uncertainties before including it in the fit.

The large increase in luminosity from Run II at the Tevatron will help to further constrain the parameters and test the models and assumptions used in HERWIG and MC@NLO.

Chapter 8

Summary

The work presented in this thesis was carried out at DØ, one of the general purpose detectors on the Tevatron proton antiproton collider, at Fermilab in the USA. The study of leptonically decaying W and Z events at the Tevatron is interesting for a number of reasons. A detailed understanding of both W and Z events is required to minimise the uncertainties on electroweak precision measurements, including one of the most important measurements to come from Run II at the Tevatron, the W boson mass. The clean signatures of leptonically decaying W and Z events make them ideal for understanding and calibrating the detector and trigger systems and for testing the QCD aspects of their production mechanisms.

Chapter 6 described the measurement of the inclusive $Z/\gamma^* \to \mu^+\mu^-$ cross section, for $M_{\mu\mu} > 40$ GeV, using 147.7 pb^{-1} of integrated luminosity. The final result:

$$\sigma\,(Z/\gamma^*) = 327.8 \pm 3.4(\text{stat.}) \pm 8.4(\text{syst.}) \pm 21.3(\text{lumi.}) \;\; \text{pb} \tag{8.1}$$

was obtained. The inclusive $Z \to \mu^+\mu^-$ cross section was extracted from this result and found to be:

$$\sigma\,(Z) = 290.1 \pm 3.0(\text{stat.}) \pm 7.4(\text{syst.}) \pm 18.9(\text{lumi.}) \;\; \text{pb.} \tag{8.2}$$

The extraction of these numbers required detailed knowledge of muon reconstruction and trigger efficiencies, which were measured using the $Z/\gamma^* \to \mu^+\mu^-$ data. These efficiencies are used in other analyses within DØ of processes containing high p_T muons. The extracted inclusive $Z \to \mu^+\mu^-$ cross section will be combined with the inclusive $W \to \mu\nu$ cross section to obtain an indirect measurement of the W width, which places constraints on exotic W decays.

Monte Carlo event generators, such as HERWIG and PYTHIA, are invaluable to the interpretation of results at hadron colliders. Comparing their predicted distributions to data is essential in testing that they accurately describe the processes occurring in nature. Chapter 7 presented comparisons made between DØ data, collected during Run I at the Tevatron, and HERWIG and MC@NLO predictions. The W and Z boson p_T distributions were studied, with relevant Monte Carlo parameters tuned to obtain the closest possible fit to data. An excellent agreement is found for both HERWIG and MC@NLO. In order to further constrain the models used in Monte Carlos it will be necessary to use the increased statistics and reduced systematics that are becoming available from Run II data.

Increasing our understanding of electroweak processes at hadron colliders is not only crucial for the Run II physics programme at the Tevatron. The Large Hadron Collider (LHC) is due to start colliding protons with protons at CERN in 2007. The LHC will supersede the Tevatron as the highest energy accelerator in the world and, with a centre of mass energy of 14 TeV, it will play a pivotal role in particle physics research for the next 15 years or so. The most popular BSM theories are expected to be verified or ruled out at the LHC and if the long sought-after Higgs boson is not discovered there, its existence within current theories will be severely doubted. Understanding the hadronic environment at the Tevatron is an important prerequisite to understanding the similar, but more complicated, environment at the LHC and the study of electroweak physics is essential in achieving this.

Appendix A

Loose and Medium Muon Definitions

The quality of a muon is defined by the type and number of hits it has in the muon detectors:

A muon with both A- and BC-layer segments is:

- *medium* if it has:
  - at least two A-layer wire hits,
  - at least one A-layer scintillator hit,
  - at least two BC-layer wire hits and
  - at least one BC-layer scintillator hit (except for central muons with less than four BC-layer wire hits);
- *loose* if passes two of the above requirements, with the A-layer wire and scintillator hits treated as one requirement and always requiring at least one scintillator hit.

A muon with only BC-layer segments is:

- *medium* if it:
  - has at least one BC-layer scintillator hit,
  - has at least two BC-layer wire hits and
  - is located in the bottom two octants of the detector with $|\eta_A| < 1.6$;

- *loose* if it satisfies the first two of the above three requirements.

A muon with only A-layer segments is:

- *medium* if it:
  - has at least one A-layer scintillator hit,
  - has at least two A-layer wire hits and
  - is located in the bottom two octants of the detector with $|\eta_A| < 1.6$;
- *loose* if it satisfies the first two of the above three requirements.

Appendix B

Refitting CFT-Only Central Tracks

The resolution of $\frac{q}{p_T}$ for central tracks with hits in the CFT but not the SMT can be improved by constraining them to have a dca of zero. If the measured values are denoted $\frac{q}{p_T}$ and dca, and the known values are denoted $\left(\frac{q}{p_T}\right)'$and dca', then the χ^2 of the two variables is:

$$\chi^2 = \left(\; dca - dca', \quad \frac{q}{p_T} - \left(\frac{q}{p_T}\right)' \; \right) V^{-1}_{dca,\frac{q}{p_T}} \left(\begin{array}{c} dca - dca' \\ \frac{q}{p_T} - \left(\frac{q}{p_T}\right)' \end{array} \right), \tag{B.1}$$

where $V^{-1}_{dca,\frac{q}{p_T}}$ is the inverse of the two dimensional track fit error matrix:

$$V_{dca,\frac{q}{p_T}} = \left(\begin{array}{cc} \sigma_{dca,dca} & \sigma_{dca,\frac{q}{p_T}} \\ \\ \sigma_{\frac{q}{p_T},dca} & \sigma_{\frac{q}{p_T},\frac{q}{p_T}} \end{array} \right) \tag{B.2}$$

so that

$$V^{-1}_{dca,\frac{q}{p_T}} = \frac{1}{\sigma_{\frac{q}{p_T},\frac{q}{p_T}}\sigma_{dca,dca} - \sigma^2_{dca,\frac{q}{p_T}}} \left(\begin{array}{cc} \sigma_{\frac{q}{p_T},\frac{q}{p_T}} & -\sigma_{dca,\frac{q}{p_T}} \\ -\sigma_{\frac{q}{p_T},dca} & \sigma_{dca,dca} \end{array} \right). \tag{B.3}$$

The value of $\left(\frac{q}{p_T}\right)'$ is found by substituting equation B.3 into equation B.1 and minimising the χ^2:

$$\frac{d\chi^2}{d\left(\frac{q}{p_T}\right)'} = 2\sigma_{dca,\frac{q}{p_T}}\left(dca - dca'\right) - 2\sigma_{dca,dca}\left(\; \frac{q}{p_T} - \left(\frac{q}{p_T}\right)' \; \right) = 0 \tag{B.4}$$

and since dca' is constrained to be zero:

$$\left(\frac{q}{p_T}\right)' = \frac{q}{p_T} - \left(\frac{\sigma_{dca,\frac{q}{p_T}}}{\sigma_{dca,dca}}\, dca\right). \tag{B.5}$$

Appendix C

Triggers

Table C.1 summarises the different combinations of triggers used to select candidate $Z/\gamma^* \rightarrow \mu^+\mu^-$ events, with the relative amount of integrated luminosity. The trigger names are composed of abbreviations of the different components that make up the trigger. Table C.2 summarises the abbreviated names and what they represent. During period 1 and period 2a (defined in section 6.6.1) candidate events are required to have been selected by one of the di-muon trigger combinations given in the first two rows in Table C.1 (the name of a di-muon trigger always begins with a 2). During period 2b candidate events are required to have been selected by one of the single

Trigger combination	$\int \mathcal{L}dt$ [pb^{-1}]
2MU_A_L2M0	37.4
2MU_A_L2ETAPHI or 2MU_A_L2M0_L3L15 or 2MU_A_L2M0_TRK10	0.9
MUW_W_L2M3_TRK10 or 2MU_A_L2M0	89.2
MUW_W_L2M3_TRK10 or 2MU_A_L2ETAPHI or 2MU_A_L2M0_L3L15 or 2MU_A_L2M0_TRK10	8.8
MUW_W_L2M3_TRK10 or 2MU_A_L2ETAPHI or 2MU_A_L2M0_L3L6 or 2MU_A_L2M0_TRK5	6.2
MUW_W_L2M3_TRK10 or 2MU_A_L2M0_L3L6 or 2MU_A_L2M0_TRK5	5.1

Table C.1: *Breakdown of $\int \mathcal{L}dt$ by combination of triggers used. When two or more triggers are or-ed together an event is written to storage tapes if it is accepted by any of those triggers.*

Component Name	Description
2MU	two Level 1 tight scintillator muons
MU	one Level 1 tight scintillator muon
MUW	one Level 1 tight scintillator + loose wire muon
A	Level 1 muons can be anywhere
W	Level 1 muons have $\|\eta_A\| < 1.5$
L2M0	one Level 2 medium muon
L2M(3, 5)	one Level 2 medium muon, $p_T > (3, 5)$ GeV
L2ETAPHI	two well separated Level 2 medium muons
TRK(3, 5, 10)	one Level 3 central track, $p_T > (3, 5, 10)$ GeV
2TRK3	two Level 3 central tracks, $p_T > 3$ GeV
L3L(6, 15)	one Level 3 muon, $p_T > (6, 15)$ GeV

Table C.2: *Description of trigger components used to make up the muon trigger names.*

and di-muon trigger combinations given in the remaining rows in Table C.1.

The efficiency of the 'or' of the triggers 2MU_A_L2M0_TRK(5,10), 2MU_A_L2M0_L3L(6,15) and 2MU_A_L2ETAPHI is found by measuring the fraction of events firing the 2MU_A_L2M0 trigger that also fire one of the above triggers. It is found to be 100%. The efficiency of the 'or' of the triggers 2MU_A_L2M0_TRK(5,10) and 2MU_A_L2M0_L3L(6,15) is found in the same way. It is found to be 99.6%. Since this combination is only used in a 3.5% of the luminosity, the overall inefficiency of the 'or' of these triggers with respect to 2MU_A_L2M0 is 99.999% and is taken to be 100%. It is therefore only necessary to calculate the efficiency for 2MU_A_L2M0 and MUW_W_L2M3_TRK10.

Bibliography

[1] S. L. Glashow, Nucl. Phys. **22** (1961) 579.

[2] S. Weinberg, Phys. Rev. Lett. **19** (1967) 1264.

[3] A. Salam, *Elementary Particle Theory*, ed. N. Svartholm (Almquist and Wiksell, Stockholm, 1968) p. 376.

[4] W. A. Bardeen, A. J. Buras, D. W. Duke and T. Muta, Phys. Rev. D **18** (1978) 3998.

[5] P. W. Higgs, Phys. Rev. **145** (1966) 1156.

[6] t. L. E. Group, t. S. Electroweak and H. F. Groups [OPAL Collaboration], *A combination of preliminary electroweak measurements and constraints on the standard model*, arXiv:hep-ex/0412015.

[7] S. Abachi *et al* [The DØ Collaboration], *The DØ upgrade: The detector and its physics,* FERMILAB-PUB-96-357-E (1996).

[8] P. Telford, N. Hadley and L. Wang, *Re-tuning of pmcs_chprt to P13 and P14 data*, DØ Note 4297 (2003).

[9] S. Eidelman *et al.* [Particle Data Group Collaboration], Phys. Lett. B **592** (2004) 1.

[10] W.K. Sakumoto, *W/Z Cross Section Predictions for* $\sqrt{s} = 1.96$ *TeV,* **cdf6341** (2003).

[11] R. Hamberg, W. L. van Neerven and T. Matsuura, Nucl. Phys. B **359** (1991) 343.

[12] W. L. van Neerven and E. B. Zijlstra, Nucl. Phys. B **382** (1992) 11.

[13] G. Corcella, I.G. Knowles, G. Marchesini, S. Moretti, K. Odagiri, P. Richardson, M.H. Seymour and B.R. Webber, JHEP **0101** (2001) 010.

[14] T. Sjöstrand, P. Edén, C. Friberg, L. Lönnblad, G. Miu, S. Mrenna and E. Norbin, Computer Phys. Commun. **135** (2001) 238.

[15] G. Dissertori, I.G. Knowles and M. Schmelling, *Quantum Chromodynamics*, Oxford Science Publications (2003) p. 45.

[16] S. Frixione and B.R. Webber, **JHEP 0206** (2002) 029.

[17] Y. Fisyak and J. Womersley, *DØ GEANT Simulation of the Total Apparatus Response*, DØ Note 3191 (1997).

[18] GEANT 3, CERN Program Library Long Write-up, W5013 (1993).

[19] T. Edwards, S. Yacoob, T. Andeen, M. Begel, B. Casey, R. Partridge, H. Schellman, A. Sznajar, *Luminosity Constant for DØ Run II*, DØ Note 4496, (2004).

[20] F. Abe *et al.* [CDF Collaboration], Phys. Rev. D **50** (1994) 5550.

[21] C. Avila *et al.* [E811 Collaboration], Phys. Lett. B **445** (1999) 419.

[22] S. Klimenko, J. Konigsberg and T. M. Liss, *Averaging of the inelastic cross sections measured by the CDF and the E811 experiments*, FERMILAB-FN-0741 (2003).

[23] M. Verzocchi, private communication.

[24] J. Elmsheuser, *Search for the Higgs boson in* $H \to WW^{(*)} \to \mu^+\nu_\mu\mu^-\bar{\nu_\mu}$ *decays at DØ in Run II*, DØ Note 4386 (2004) p.16.

[25] H. Fox, private communication.

[26] J. Pumplin, D. R. Stump, J. Huston, H. L. Lai, P. Nadolsky and W. K. Tung, JHEP **0207** (2002) 012.

[27] U. Yang and Y. Kim, *ISR Studies on Drell-Yan*, Fermilab MC Workshop (2003), http://cepa.fnal.gov/patriot/mc4run2/MCTuning/031204/unki.pdf

[28] R. Field, *Pythia Tune Set A* (2002), http://www.phys.ufl.edu/∼rfield/cdf/tunes/py_tuneA.html

[29] E. Nurse and P. Telford, *Measurement of the Cross section for Inclusive Z Production in Di-muon Final States at* $\sqrt{s} = 1.96$ *TeV*, DØ Note 4689 (2005).

[30] B. Tuchming, private communication.

[31] The DØ collaboration, *Measurement of the Cross Section for W and Z Production to Electron Final States with the DØ Detector at sqrts* $= 1.96$ *TeV*, DØ Note 4403-CONF (2004).

[32] H. L. Lai *et al.*, Phys. Rev. D **55** (1997) 1280.

[33] D. Acosta *et al.* [CDF Collaboration], *First Measurements of Inclusive W and Z Cross Sections from Run II of the Tevatron Collider*, hep-ex/0406078.

[34] T. Nunnemann, *NNLO Cross-Sections for Drell-Yan, Z and W Production using Modern Parton Distribution Functions*, DØ Note 4476 (2004).

[35] B. Abbott *et al.* [DØ Collaboration], Phys. Lett. B **513** (2001) 292

[36] B. Abbott *et al.* [D0 Collaboration], Phys. Rev. D **61** (2000) 032004.

[37] R.K. Ellis, W.J. Stirling and B.R. Webber, *QCD and Collider Physics*, Cambridge University Press (1996) p. 424.

[38] M.H. Seymour and B.R. Webber, private communication.

[39] H. Plothow-Besch, Computer Phys. Commun. **75** (1993) 396.

[40] A. D. Martin, R. G. Roberts, W. J. Stirling and R. S. Thorne, Phys. Lett. B **443** (1998) 301.

[41] A. D. Martin, R. G. Roberts, W. J. Stirling and R. S. Thorne, Eur. Phys. J. C **4** (1998) 463.

[42] J. Botts, J. G. Morfin, J. F. Owens, J. w. Qiu, W. K. Tung and H. Weerts [CTEQ Collaboration], Phys. Lett. B **304** (1993) 159.

[43] G. Corcella, I.G. Knowles, G. Marchesini, S. Moretti, K. Odagiri, P. Richardson, M.H. Seymour and B.R. Webber, *HERWIG 6.5 Release Note*, arXiv:hep-ph/0210213 (2002).